

# The Formation Mechanisms of Galaxy Tails: A Statistical and Case Study

THE FORMATION MECHANISMS OF GALAXY TAILS:  
A STATISTICAL AND CASE STUDY

By Alex LU,

*A Thesis Submitted to the School of Graduate Studies in the Partial  
Fulfillment of the Requirements for the Degree Masters of Science*

McMaster University © Copyright by Alex LU September 12, 2022

McMaster University

Masters of Science (2022)

Hamilton, Ontario (Department of Physics and Astronomy)

TITLE: The Formation Mechanisms of Galaxy Tails: A Statistical and Case Study

AUTHOR: Alex LU (McMaster University)

SUPERVISORS: Dr. James WADSLEY and Dr. Laura PARKER

NUMBER OF PAGES: xiv, 129

# A Note on Terminology

In this work, unless otherwise specified, terms such as "ISM" and "disk" will be used to refer to material within a sphere of radius  $3r_e$ , and terms such as "CGM" and "annulus" will be used to refer to material between  $3r_e$  and  $R_{\text{vir}}$ . Group gas or IGM will refer to unbound material within 2 virial radii of the group near the halo. Refer to Chapter 2 for the definitions of  $r_e$  and  $R_{\text{vir}}$ .

# Abstract

Using a hydrodynamical smoothed particle hydrodynamics (SPH) zoom-in simulation of a galaxy group, we present a set of tail identification methods, and study the statistical properties of galaxy tails and their correlations with their expected formation mechanisms. We have a sample of 4548  $M > 10^8 M_\odot$  galaxies across 58 snapshots from  $z = 0.67$  to  $z = 0$ . For each galaxy, we apply a series of velocity and density cuts to identify the tail. We observed no significant correlations between galaxy tail mass and ram pressure, though we note some issues with our sampling. Tracking four visually identified jellyfish galaxies over time showed some evidence of increased ram pressure driving ISM mass loss, as well as spikes in tail mass preceding spikes in ram pressure with temporal offsets ranging from 500 Myr to 2 Gyr. No correlation was found between ISM mass and tail mass. We track the tail gas of a particularly well defined jellyfish galaxy 3.2 Gyrs back in time. We find that a lower bound of 30% of the tail gas was never in the ISM. Distinguishing between former ISM tail material and never ISM-accreted tail material, we see evidence of temperature mixing with the IGM in the former. Velocity and radial trajectory maps show a sharp impulse of  $\Delta v \approx 50 \text{ km s}^{-1}$  over 4 snapshots, affecting both the never ISM-accreted tail material and CGM material, with the former showing evidence of momentum mixing onto the former ISM material. Combined with observations of CGM stripping, we propose that a significant portion of galaxy tails consists of stripped CGM that got swept up into the stripped ISM.

## *Acknowledgements*

I would like to express my sincerest gratitude to my supervisors Dr. James Wadsley and Dr. Laura Parker for their guidance, patience and support throughout my MSc. I would also like to thank my fellow graduate students and friends for making my experience at McMaster an absolute joy.

I dedicate this thesis in memory of my grandmother, who has always dreamed of seeing my academic success. May she rest in peace, and I hope I have made her proud.

# Contents

<b>Abstract</b>	<b>iv</b>
<b>Acknowledgements</b>	<b>v</b>
<b>1 Introduction</b>	<b>1</b>
1.1 Galaxies . . . . .	1
1.2 The Galactic Environment . . . . .	5
1.2.1 The Intragroup Medium . . . . .	5
1.2.2 Starvation . . . . .	6
1.2.3 Ram Pressure Stripping . . . . .	7
1.3 Jellyfish Galaxies . . . . .	8
1.3.1 Entrainment . . . . .	10
1.4 Simulating The Universe . . . . .	11
1.4.1 Why Simulate? . . . . .	11
1.4.2 Hydrodynamics . . . . .	11
1.4.3 Octree Optimization . . . . .	13
1.5 Outline for Thesis . . . . .	15
<b>2 Dataset and Methods</b>	<b>17</b>
2.1 The Simulation Setup . . . . .	17

2.2	Halos . . . . .	19
2.2.1	Finding and Loading Halos . . . . .	19
2.2.2	Centering and Orienting . . . . .	21
2.3	Galaxy Properties . . . . .	25
2.3.1	The Effective Radius . . . . .	25
2.3.2	The Disk . . . . .	26
2.3.3	Star Formation Rate . . . . .	26
2.3.4	Ram Pressure and the Modified Stripping Criterion . . . . .	30
2.4	Group Characteristics . . . . .	32
2.5	The Galaxy Sample . . . . .	33
2.5.1	Merger Trees . . . . .	35
2.5.2	Ancestor Tracking and Branches . . . . .	37
2.5.3	Branch Length and Weighting . . . . .	40
2.5.4	Sample Characteristics . . . . .	42
2.6	Explored Unused Numerical Methods . . . . .	46
2.6.1	The 6-D Phase Space Convex Hull . . . . .	46
2.6.2	The Impulse Criterion . . . . .	47
<b>3</b>	<b>Tail Identification</b>	<b>48</b>
3.1	Motivation . . . . .	48
3.2	Observable Features of a Jellyfish Galaxy . . . . .	50
3.3	Tail Characteristics of a Jellyfish Galaxy in Phase Space . . . . .	54
3.3.1	The Background and Direction of Interest . . . . .	56
3.3.2	Density Space . . . . .	56
3.3.3	Temperature Space . . . . .	59

3.3.4	Velocity Space . . . . .	60
3.4	Putting It All Together . . . . .	66
3.4.1	The Tailfinding Algorithm . . . . .	66
3.4.2	Result . . . . .	68
3.4.3	The Necessity of Multiple Cuts . . . . .	69
3.5	Limitations . . . . .	74
<b>4</b>	<b>Results</b>	<b>77</b>
4.1	Statistical Galaxy Tail Correlations . . . . .	77
4.1.1	Galaxy Classifications . . . . .	77
4.1.2	Tail Orientation . . . . .	79
4.1.3	Tail Mass Correlations . . . . .	84
4.2	Time Evolution . . . . .	90
4.3	Entrainment . . . . .	97
4.3.1	Where did Tail Particles Originate? . . . . .	97
4.3.2	Particle Trajectories . . . . .	101
4.3.3	Mixing . . . . .	105
4.3.4	The Stripped CGM Hypothesis . . . . .	111
<b>5</b>	<b>Conclusion</b>	<b>119</b>
5.1	Summary Discussion . . . . .	119
5.2	Future Work . . . . .	121
<b>A</b>	<b>Finetuning the Tailfinding Algorithm</b>	<b>122</b>
	<b>Bibliography</b>	<b>125</b>

# List of Figures

1.1	SFR vs $M_*$ from Sánchez et al. 2019 . . . . .	4
1.2	RXJ1159+5531 Group Density Profile (adapted from Cavaliere et al. 2016) . . . . .	6
1.3	ESO 137-001 . . . . .	9
1.4	Quadtree Division. Fig 1 of Barnes & Hut 1986 . . . . .	14
2.1	Projection of simulation (Joshi et al. 2019) . . . . .	18
2.2	Schematic of halo . . . . .	27
2.3	Star formation calculation scheme comparisons . . . . .	29
2.4	Stellar mass function at $z = 0$ . . . . .	33
2.5	Stellar mass - halo mass relation at $z = 0$ . . . . .	34
2.6	Merger tree visualization . . . . .	36
2.7	Diagram of holes in evolutionary history of galaxies . . . . .	37
2.8	Merger tree length count . . . . .	39
2.9	Schematic justifying 0.1 weight floor . . . . .	41
2.10	Stellar mass - halo mass relation for high res galaxies from $z = 0.67$ to $z = 0$ . . . . .	43
2.11	Stellar mass function for high res galaxies from $z = 0.67$ to $z = 0$ . . . . .	44

2.12 Star forming main sequence for high res galaxies from $z = 0.67$ to $z = 0$ . . . . .	45
3.1 Optical RGB mock images for galaxy 648-1286 . . . . .	50
3.2 Gas surface density map for galaxy 648-1286, . . . . .	51
3.3 Temperature map for galaxy 648-1286 . . . . .	52
3.4 Velocity field overlayed on top of a gas surface density map for galaxy 648-1286 . . . . .	53
3.5 Density-velocity, temperature-velocity and temperature-density phase diagrams for all particles in the annulus between $3r_e$ and $R_{\text{vir}}$ for galaxy 648-1286 . . . . .	55
3.6 Visual representation of the background cut . . . . .	57
3.7 Distribution of particle densities for galaxy 648-1286 . . . . .	58
3.8 Distribution of gas particle temperatures for galaxy 648-1286 . . . . .	60
3.9 Distribution of gas particle temperatures for all sampled galaxies . . . . .	61
3.10 Distribution of projected velocities within the annulus for galaxy 648-1286 . . . . .	64
3.11 Same velocity distribution as Figure 3.10 with curve fits . . . . .	65
3.12 Figure 3.5 with cuts shown . . . . .	67
3.13 Gas density maps of galaxy 648-1286, with tail particle positions plotted on top . . . . .	68
3.14 Gas surface density map for galaxy 608-108 . . . . .	70
3.15 Gas density maps of galaxy 608-108 with dense particle positions plotted on top . . . . .	71
3.16 Figure 3.12 but for galaxy 608-108 . . . . .	72

3.17 Gas density maps of galaxy 608-108, with tail particle positions scattered on top . . . . .	73
3.18 The gas density map of galaxy 568-5023 on the left, with the particles identified by the tailfinding algorithm overlaid on the right. 568-5023 is an ancestor of infalling galaxy 648-1286, and is many virial radii away from the group at the time this gas density image is taken at. . . . .	76
4.1 Diagram showing three vectors of interest for a tailed galaxy . . . . .	79
4.2 Dot products between the position, tail centroid and velocity vectors	80
4.3 Tail orientation comparisons between our sample, LoTSS tails (Roberts et al. 2021a) and IllustrisTNG tails ( <b>sty3156</b> ) . . . . .	83
4.4 Stripping criterion vs tail mass and normalized tail mass scatter plots	85
4.5 Star mass vs stripping criterion and normalized tail mass scatter plots	86
4.6 Ram pressure vs tail mass and normalized tail mass scatter plots . .	87
4.7 Ram pressure vs ISM mass flux over a single snapshot . . . . .	89
4.8 Tail mass, star formation rate (total), star formation rate (tail), ram pressure, ISM mass ratio, and group-centric distance over time for four jellyfish galaxies . . . . .	91
4.9 The time evolution of galaxy 4347. As with Figure 4.8, the bad data points in ISM mass are removed. The yellow curve represents the radial trajectory of the galaxy . . . . .	93
4.10 The time evolution of galaxy 10641. As with Figure 4.8, the bad data points in ISM mass are removed. The yellow curve represents the radial trajectory of the galaxy . . . . .	94

4.11	The time evolution of galaxy 3626. As with Figure 4.8, the bad data points in ISM mass are removed. The yellow curve represents the radial trajectory of the galaxy . . . . .	95
4.12	Gas density maps for galaxy 648-1286 and galaxy 584-5100 . . . . .	98
4.13	The mass fraction of tail mass that ever entered the disk vs the total tail mass over time . . . . .	99
4.14	The same gas density maps as Figure 4.12, but with tail particles positions scattered on top . . . . .	100
4.15	Gas density maps of galaxy 648-1286 and 584-5100, but 3.2 Gyrs back in time . . . . .	101
4.16	Radial tail particle trajectories over time for galaxy 648-1286 and galaxy 584-5100 . . . . .	102
4.17	Projected relative velocity tail particle trajectories over time for galaxy 648-1286 and galaxy 584-5100 . . . . .	103
4.18	Averaged versions of Figures 4.16 and 4.17 with ram pressure shown	104
4.19	Histograms of tail particle temperatures for galaxy 10641 and galaxy 4347 . . . . .	106
4.20	Average temperature trajectories of the entrained and stripped particles for galaxy 10641 and galaxy 4347 . . . . .	107
4.21	Greyscale gas density maps of galaxy 648-1286 and 584-5100 with tail particles temperatures plotted on top . . . . .	108
4.22	Histograms of tail particle metallicities for galaxy 10641 and galaxy 4347 . . . . .	109
4.23	Average metallicity trajectories of the entrained and stripped particles for galaxy 10641 and galaxy 4347 . . . . .	110

4.24	The time evolution of the CGM for galaxy 10641 . . . . .	112
4.25	Projected relative velocity trajectories of the CGM gas from -3.2 Gyr	113
4.26	Projected radial trajectories of the CGM gas from -3.2 Gyr . . . . .	114
4.27	Projected relative velocity distributions of the CGM gas at three distinct times . . . . .	115
4.28	Temperature trajectory of the non-tail particles within $R_{\text{vir}}$ of galaxy 10641 over time . . . . .	116
4.29	Projected relative velocity trajectories of the CGM gas and en- trained tail gas from -3.2 Gyr . . . . .	117
4.30	A closer look at the tail mass spike in Figure 4.10 . . . . .	118
A1.1	Mass fraction over time and mass ever in disk over time for five jellyfish galaxies . . . . .	124

# List of Tables

3.1	Table of galaxies and the expected velocity/position shifts for their ISM due to ram pressure . . . . .	63
4.1	Our sample selection table. Here $R_{\text{vir}}$ refers to the virial radius of the group. . . . .	78
4.2	A table of weighted two sample KS test statistics between the position-tail centroid dot product distribution of a given class and a uniform random distribution of dot products, with the null hypothesis assuming both distributions are the same . . . . .	82
4.3	A table showing the stellar mass and status of each galaxy at $z = 0$	92

# Chapter 1

## Introduction

### 1.1 Galaxies

Galaxies are among the most common objects in the universe, tracing the largest scale structures. They consist of gravitationally bound stars, gas and dust, embedded in a larger dark matter halo. Galaxies are diverse objects with a range of observable properties such as colour and morphology. They have also been observed over an enormous range of distances, from our very own Milky Way and our close neighbour Andromeda, to what could potentially be the furthest galaxies we've ever seen in GLASS z-13 and z-11 at dozens of billions of light years away, approaching the edge of our observable universe (Naidu et al. 2022). They also vary drastically in mass: from Segue 2, a tiny spheroidal dwarf galaxy (Belokurov et al. 2009) with a mass of  $5.5 \times 10^5 M_{\odot}$ , to Triangulum, a nearby dwarf spiral galaxy with a mass of  $5 \times 10^{10} M_{\odot}$ , all the way up to IC 1101, one of the largest elliptical galaxies ever discovered (Dullo et al. 2017) with a whopping mass of  $2.5 \times 10^{15} M_{\odot}$ .

The physics of galaxies is highly nonlinear and occurs on all scales - from the formation of planets and planetesimals through hierarchical coagulation and streaming instabilities (Del Popolo et al. 2003, Youdin & Goodman 2005) on cm-km scales, to the collapse of giant 100 pc-scale molecular clouds (Wu et al. 2015, López et al. 2011) into AU-scale protoplanetary disks where stars are birthed (Pringle 1981), to the formation of kpc scale superbubbles - the collective remnants of many supernovae (Pidopryhora et al. 2007, Bialy et al. 2021), all the way to the hundreds of kpc scale outflows driven by active galactic nuclei in the most massive galaxies (Martín-Navarro et al. 2018, Harrison et al. 2018). Galaxies also tend to live in larger environments such as groups and clusters (see Section 1.2), where even larger scale physics such as merging, stripping, starvation and rejuvenation occur (Bautz & Morgan 1970, Hickson 1997). The physics of the smaller and larger scales can often be intertwined and overlap with each other. For instance, the supernovae driven superbubbles, which are large kpc-sized cavities filled with hot gas above  $10^6$  K, prevent the collapse of cold molecular gas clouds, a process essential to star formation. Additionally, AGN driven jet outflows can create large regions of hot gas that can drive environmental effects that impact the star formation of the whole galaxy (Scheuer 1974, Wu et al. 2017, Saxena et al. 2018). Galaxy physics at all scale exist in a tightly interconnected web - insights in any specific phenomenon or mechanism will cascade into further insights in other phenomena.

The study of galaxies has also given us bountiful insights on the workings of our Universe as a whole. In the early 20th century, observations of nearby galaxies showed them to be moving away from us, with recession velocities increasing with distance (Hubble 1937, Slipher 1913). Observations of Andromeda's rotation curve

showed significant deviations between observed and expected velocities given the observable mass (Rubin & Ford 1970, Babcock 1939), which fueled evidence for the existence of dark matter, the properties of which have been studied extensively since in gravitational lensing (Allen et al. 2011, Natarajan et al. 2017) and the Cosmic Microwave Background (CMB) (Hinshaw et al. 2009). Both theoretical models and observations of high redshift galaxies, supernovae and the CMB led to the discovery of dark energy ( $\Lambda$ ), causing an acceleration in the expansion rate of our Universe (Paal et al. 1992). This all eventually led to the widely accepted  $\Lambda$ -CDM model of our Universe.

Observationally, galaxies are characterized by their luminosities, colours, and spectra. Shifts in the spectrum reveal the rotation curve and redshift; total mass can be estimated from the luminosity using a mass-to-light ratio derived from the colour and empirical models (Huchra 2003) or spectral energy distribution (SED) fitting (Baes 2020); metallicities can be derived from the colour and spectra using calibrated models; molecular gas abundances can be traced by CO emission lines and dust abundances can be traced by far infrared emissions.

One of the most important properties of galaxies is their star formation rates (SFR). Comparing SFR to properties such as metallicity, colour and molecular gas abundances can provide key insights on the mechanisms that drive star formation and the effects star formation has on the galaxy. One method of deriving SFRs is by studying specific emission lines such as H- $\alpha$ , or overall emissions in UV and IR (Dijkstra & Westra 2010, Leroy et al. 2012). UV traces the direct emissions from bright young stars and IR traces absorption and re-emission from ISM dust, while H- $\alpha$  traces recombination events in the HII regions ionized by the UV radiation.

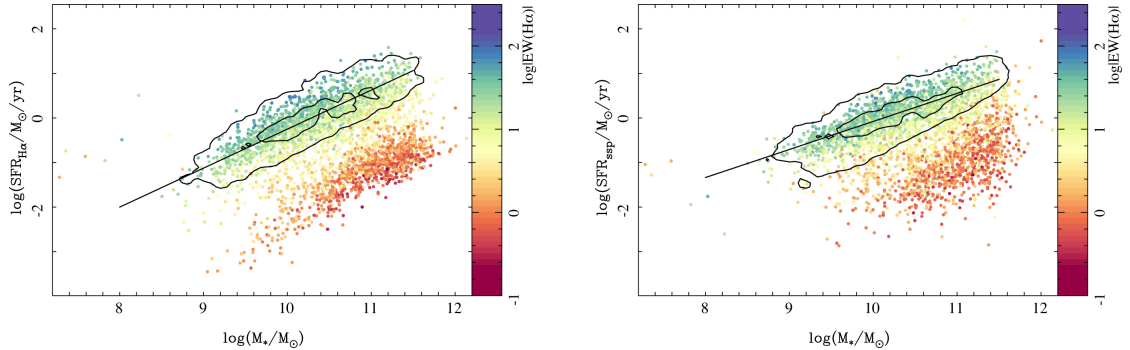


FIGURE 1.1: Figure 1 from Sánchez et al. 2019. Each panel plots star formation rate vs stellar mass, with star formation calculated using H- $\alpha$  abundances (left) and stellar mass accumulation in the last 100 Myr (right). The colour represents the equivalent width (EW) of H- $\alpha$  averaged across the field of view of each datacube. Contours encircle 95% (outer) and 25% (inner) of the galaxies.

Observed galaxies tend to lie along a star forming main sequence - an empirical relation between a galaxy's star formation rate and stellar mass. Most stellar mass-star formation plots of galaxies from surveys show not only the main sequence but a second distinct population below the main sequence, representing galaxies with significantly lower star formation rates. These two populations are colloquially known as "blue, star forming galaxies" and "red and dead galaxies" respectively. Their colour namesakes are based on both the physics of star formation and the observational data showing strong correlations between colour and stellar population. Light from blue galaxies is dominated by younger blue stars with shorter Myr-scale lifespans, indicating high star formation rates. Meanwhile, light from red galaxies is dominated by older red stars and red giants, indicating low, if not zero, star formation rate (Tortora et al. 2010, Strateva et al. 2001). In Figure 1.1 we see an example of a star forming main sequence plot, illustrating both the star forming population and the red and dead population. (Sánchez et al. 2019).

The process of star formation requires a supply of cold, molecular hydrogen. A galaxy will stop forming stars when its supply of gas runs out, where it migrates from the blue star forming region to the red and dead region of the star forming main sequence. This process is known as quenching and remains an active area of research (Schawinski et al. 2014, Suess et al. 2022, Brownson et al. 2022). Simulations have shown supernovae to be an important mechanism in quenching galaxies (Smith et al. 2018, Lucas et al. 2020), particularly in the form of superbubbles which prevent the collapse of gas necessary to form stars (Keller et al. 2016a). As mentioned above, for more massive galaxies, AGN driven outflows can significantly heat the galactic environment, preventing the accretion of extra-galactic cool gas, effectively "starving" the galaxy (Scheuer 1974, Wu et al. 2017, Saxena et al. 2018).

## 1.2 The Galactic Environment

At  $z = 0$ , up to 50% of all galaxies reside in either groups or clusters. A large proportion of galaxies are not only driven by internal mechanisms, but also external, environmental mechanisms.

### 1.2.1 The Intragroup Medium

Isolated galaxies are driven almost entirely by self-regulation, however the same cannot be said for galaxies residing in groups and clusters. The intragroup medium, and by extension the intracluster medium, consists of hot gas of around  $10^7$  K ( $10^8$  K for clusters), and dominated by X ray emissions. Typical IGM densities are orders of magnitude less than ISM densities and increase with decreasing group-centric distance following a power law, with an example shown in Figure 1.2. At the

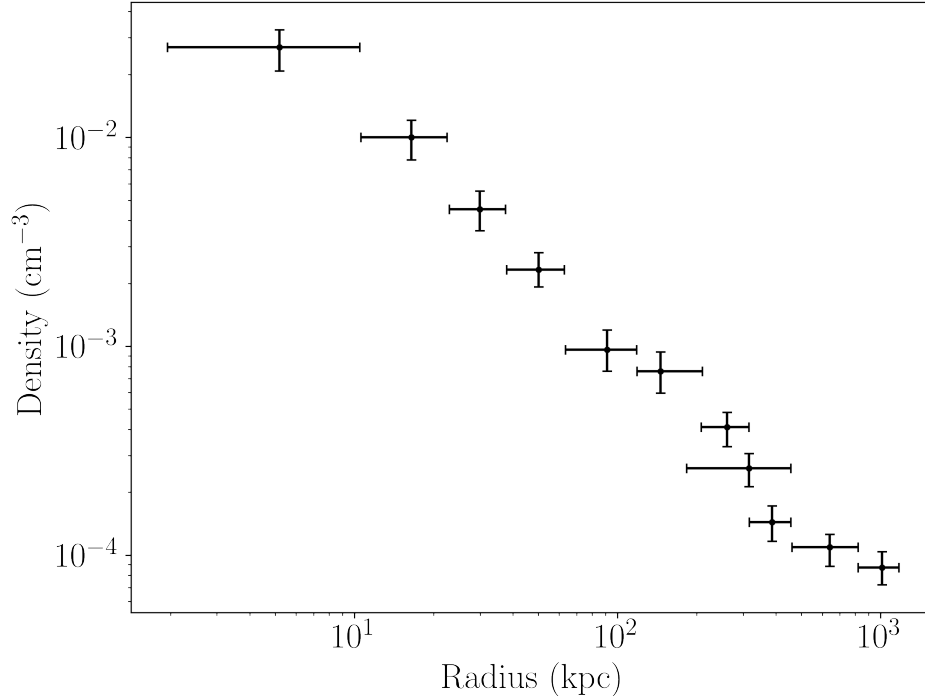


FIGURE 1.2: Adapted from Fig 1 from Cavaliere et al. 2016. This shows the 3D density profile of group RXJ1159+5531. The data is taken using a spectral deprojection tool.

centers of groups sits the brightest group galaxy (BGG), generally characterized as a massive red and dead galaxy that sees occasional star formation bursts as infalling satellites merge onto it (Cavaliere et al. 2016, Sun et al. 2009, Oppenheimer et al. 2021). The origins of the hot, dense group medium is generally speculated to be a combination of remnant gas from mergers, and AGN outflows from the BGG.

### 1.2.2 Starvation

The hot IGM can have several important effects on the galaxy. As mentioned earlier, the process of star formation involves the collapse of cold molecular gas. One environmental mechanism that quenches star formation is starvation, which occurs when there is no longer an inflow of cold gas into a galaxy. Starvation

occurs mostly in the denser regions of the ICM or IGM, where the entire medium is hot with a lack of cold molecular gas, which in turn prevents the inflow of cold gas. Evidence for this phenomenon is seen with observations of star formation rates of galaxies in clusters - galaxies near the center of clusters exhibit lower SFRs compared to galaxies further away (Haines et al. 2013, Kawinwanichakij et al. 2017, Peng et al. 2015).

### 1.2.3 Ram Pressure Stripping

Another important mechanism can occur when a galaxy is moving through the dense medium. The medium acts as a fluid flowing around the galaxy, applying ram pressure to the galaxy. The ram pressure can be expressed as

$$P = \rho v^2 \tag{1.1}$$

where  $\rho$  represents the density of the medium, and  $v$  represents the galaxy's velocity relative to the medium.

For a galaxy moving through the IGM, the ram pressure it experiences depends on the density of the medium  $\rho$  and the velocity of the galaxy through the medium  $v$ . When the ram pressure is large, particularly near the centers of groups (see Figure 1.2), this ram pressure can exceed the gravitational binding force of the galaxy's gas content, causing stripping of the ISM. As calculated in Gunn & Gott 1972, the gravitational pressure can be estimated as

$$P_g = 2\pi G \Sigma_s \Sigma_g \tag{1.2}$$

where  $\sigma_s$  and  $\sigma_g$  represent the local stellar and gaseous surface densities of the region in question. This process is known as ram pressure stripping. Ram pressure stripping represents another way to quench galaxies via stripping of its star forming gas reserves (Nichols & Bland-Hawthorn 2011, Brown et al. 2017), but there is also evidence that ram pressure can temporarily boost star formation (Roberts & Parker 2020), likely due to compression of the ISM (Choi et al. 2022). Ram pressure stripping can also have huge morphological effects on these galaxies where they leave behind long tails of stripped gas. Galaxies with vast, extensive tails are known as jellyfish galaxies.

### 1.3 Jellyfish Galaxies

Jellyfish galaxies are characterized by visually extensive tails and reside in dense environments such as galaxy groups and clusters (see Figure 1.3). These tails have been directly observed through HI and H- $\alpha$  emissions (Boselli et al. 2018, Luber et al. 2022, Poggianti et al. 2019, Gullieuszik et al. 2020), with more recent studies looking at radio emissions (Roberts et al. 2021a). The detection of molecular gas and UV/X-ray emissions in these tails (Poggianti et al. 2019, Schellenberger & Reiprich 2015), combined with simulations (Lee et al. 2022, Steinhauser et al. 2016), indicates the presence of star formation in the tail.

Characterizing large samples of jellyfish galaxies remains an open area of research, with a recent observational study (Roberts et al. 2021a) showing a preference for small cluster-centric distances and tail orientations away from the cluster center, and a recent simulation study ( Yun et al. 2019) showing a preference for

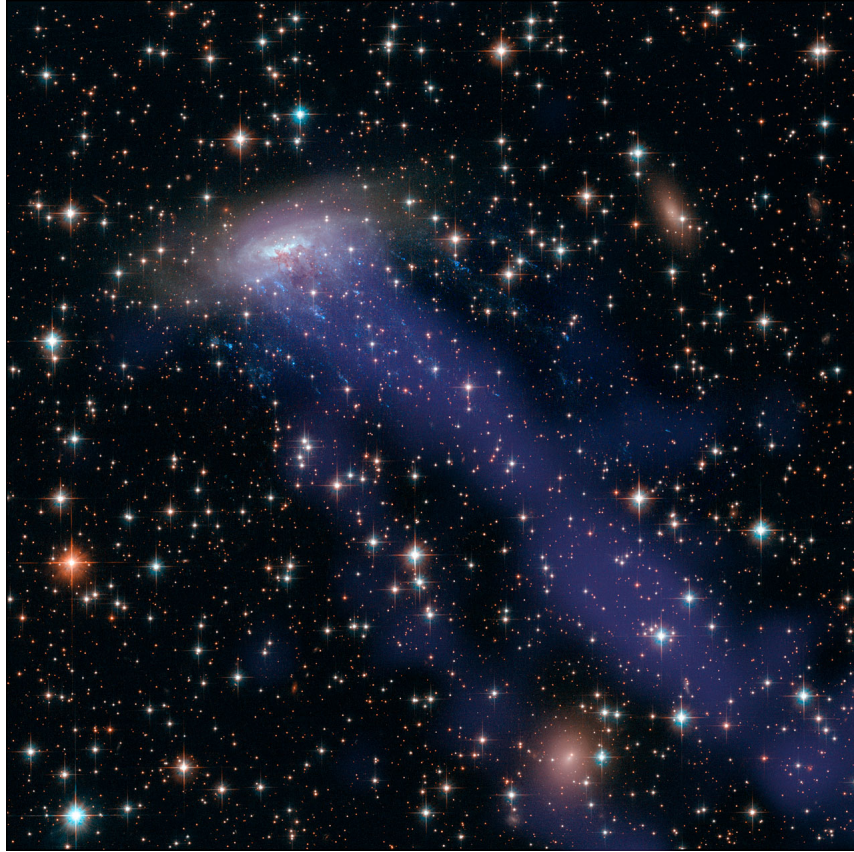


FIGURE 1.3: Jellyfish galaxy ESO 137-001. The X-ray emissions from the Chandra X-ray Observatory data is overlaid on top of the Hubble Space Telescope image. Credits to Hubble Space Telescope and Chandra X-ray Observatory.

intermediate and large cluster centric distances and no preference in its tail orientations. Jellyfish galaxies in lower mass galaxy groups have been studied less extensively. Comparisons between group and cluster jellyfish galaxies show weaker ram pressure and a lack of enhanced star formation in the former (Roberts et al. [2021b](#)).

Numerous studies have been done on jellyfish galaxies in clusters; JO201 and JO206 in the Abell 85 and IIZw108 clusters respectively, show significant HI deficiencies in the disk, exhibit long H- $\alpha$  tails, and enhanced star formation rate

efficiencies in their tails (Bellhouse et al. 2017, Ramatsoku et al. 2020); IC3418 in the Virgo clusters shows distinct, star forming UV clumps in its tail, with H- $\alpha$  clumps offset from these UV clumps (Kenney et al. 2014, Hota et al. 2021); JO204 of the Abell 957 cluster shows both a short ionized gas tail and a long neutral HI tail, along with signatures of molecular gas in both the disk and the tail (Deb et al. 2020).

Ram pressure stripping has been the widely agreed upon mechanism driving the formation of these tails, as evidenced by HI deficiencies in the disks of jellyfish galaxies (Deb et al. 2020, Haynes et al. 1984, Jaffé et al. 2013, Lubert et al. 2022). When the ram pressure  $\rho v^2$  exceeds the gravitational binding force of the disk gas (Gunn & Gott 1972), the gas is stripped out, creating long gaseous tails. This causes the aforementioned HI deficiencies in the disk, and enhanced UV/Xray/H- $\alpha$  emissions in the tail, as the cold gas in the tail collapses and forms stars far from the disk.

### **1.3.1 Entrainment**

While ram pressure remains the dominant mechanism behind tail formation, there is mounting evidence for the entrainment of intracluster gas onto the stripped interstellar medium. A recent study shows decreasing metallicity in jellyfish tails as a function of distance from the disk, an observation consistent with the cooling of metal poor ICM onto the tail (Franchetto et al. 2021). High resolution wind tunnel simulations confirm the presence of mixed ICM in tails, with up to 50% of molecular clumps in the parts of the tail far from the galactic center originating from the ICM (Lee et al. 2022). They also reveal momentum transfer mixing

processes, with the mixing ICM accelerating the tail as it moves further away from the disk, and ICM-compression driven star formation enhancement of the disk (Choi et al. 2022).

## **1.4 Simulating The Universe**

### **1.4.1 Why Simulate?**

Observational studies face a number of challenges. For instance, quantities such as mass and star formation rate must be inferred from the photometry and spectroscopy, while gas and dust abundances must be estimated from tracers such as 21 cm, H- $\alpha$ , C-O and IR emission. Line of sight radial positions must be estimated using redshifts and standard candles.

Simulations have the benefit of not only precise values for the above derived quantities and full 6D phase space information, but also access to various points in time. However simulations are constrained by the quality and accuracy of the physics implemented, and developing both accurate and efficient computational models for astrophysical processes with high spatial and temporal resolution remains an active area of research.

### **1.4.2 Hydrodynamics**

While galactic and cosmological physics occurs on all scales, the most important physics are gravity and hydrodynamics.

The standard gravitational equation of motion for some spherical mass  $i$  under the gravitational influence of  $n - 1$  other particles is:

$$\ddot{\vec{r}}_i = \sum_{n \neq i} \frac{Gm_n(\vec{r}_n - \vec{r}_i)}{|\vec{r}_n - \vec{r}_i|^3} \quad (1.3)$$

For dark matter which only interacts through gravity, solving the Newtonian equation of motion is sufficient. However, to properly simulate gas, one must account for fluid dynamics. Defining the above gravitational force as  $\vec{g}$ , the full Euler equations can be expressed as

$$\frac{\partial \rho}{\partial t} + \vec{v} \cdot \nabla \rho + \rho \nabla \cdot \vec{v} = 0 \quad (1.4)$$

$$\frac{\partial \vec{v}}{\partial t} + \vec{v} \cdot \nabla \vec{v} + \frac{\nabla p}{\nabla \rho} = \vec{g} \quad (1.5)$$

$$\frac{\partial u}{\partial t} + \vec{v} \cdot \nabla u + \frac{p}{\rho} \nabla \cdot \vec{v} = 0 \quad (1.6)$$

where  $u$ ,  $\rho$  and  $\vec{v}$  represent the fluid internal energy, density and velocity respectively.

Most modern codes follow one of two approaches - grid based codes such as RAMSES (Teyssier 2002) and ATHENA (Stone et al. 2008) or particle based codes such as GADGET-2 (Springel 2005) and Gasoline2 (Wadsley et al. 2017). Grid codes generally consist of a fixed grid of cells, allowing for a continuous flow of material between cells, while particle codes generally consist of large numbers of discrete particles, with each particle having some well defined quantities such as temperature and density, and can freely interact with other particles

across some smoothing length (known as smoothed particle hydrodynamics). Grid codes are generally better at accurately solving the Euler equations, while particle codes are generally better with obeying conservation laws and allow for particle-specific tracking over time. Codes such as Arepo (Weinberger et al. 2020) and MANGA (Chang & Etienne 2020) employ both methods by employing moving mesh codes, where meshes are generated dynamically based on particle locations at each timestep. Gravity is solved using the particles, while hydrodynamics is solved using the mesh.

In most codes, Equation 1.4 usually includes additional terms to include physics such as radiative cooling/heating and magnetic fields, but most codes solve some version of those equations. Each quantity is discretized across individual cells for grid based codes, and across individual particles for particle based codes.

### 1.4.3 Octree Optimization

Despite being a simple calculation, gravity is very expensive to calculate, especially for large numbers of objects. For  $N$  discrete elements,  $N - 1$  calculations are required per element, resulting in  $O(N^2)$  calculation time.

Most codes employ a scheme adapted from Barnes & Hut 1986, known as a Barnes-Hut algorithm. The underlying assumption is that gravitational forces exerted by far away particles can be approximated as a single force. For a group of particles far away, occupying some volume  $S$ :

$$\sum_{\vec{r}_i \in S} \vec{g}_i \approx \vec{g}_S \quad (1.7)$$

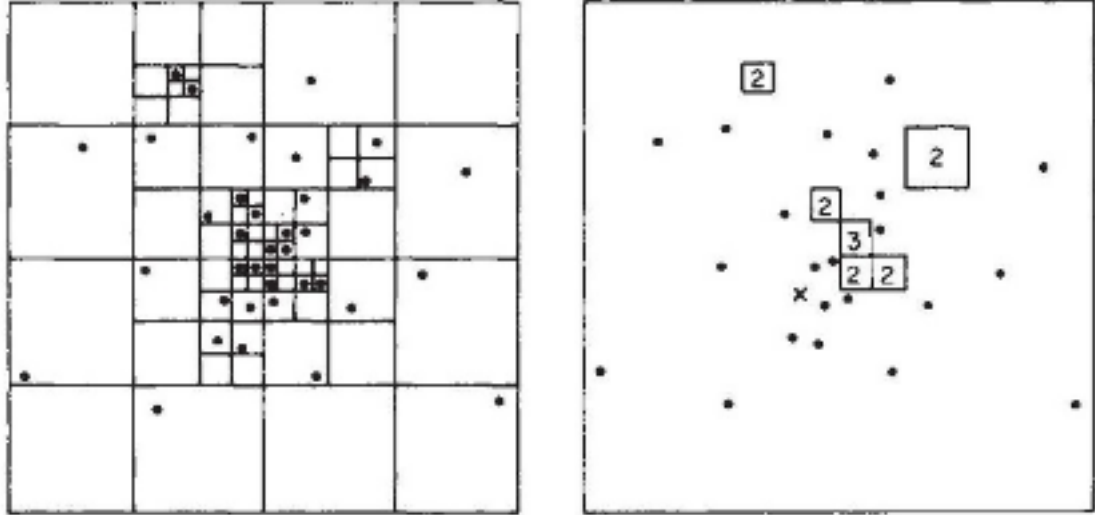


FIGURE 1.4: Fig 1 from Barnes & Hut 1986. The left represents a quadtrees subdivision of 2D space. The right represents an example of the gravity calculation - boxes represent nodes that failed the opening angle criterion relative to particle  $x$ , hence gravity is calculated for those boxes as a whole as opposed to the individual particles within.

This approximation is done via subdividing the simulation space into eight subdivisions recursively until each region contains a single particle. The data stored in a tree structure, with each node representing a region and its children representing its subdivisions. Relative to some particle, each node's particles will span some volume, which will span some angle (the opening angle) from that particle's perspective. With some opening angle criterion, gravity calculations are performed throughout the tree, but stop at nodes which fail the opening angle criterion - gravity is calculated based on the properties of that node (which represents some subdivision of space), as opposed to each individual particle within that node. This speeds up the calculation time from  $O(N^2)$  to  $O(N \log N)$  Figure 1.4 shows a simple schematic in 2D.

The simplest approximation takes  $\vec{g}_S$  as a single object with the mass of the entire node, but it can be modified to be a multipole expansion of the node’s particles for higher accuracy. More elaborate and efficient schemes have since been developed - for instance, CHANGA employs the Fast Multipole Method, which computes node-node interactions as opposed to particle-node interactions (Menon et al. 2015).

## 1.5 Outline for Thesis

Jellyfish galaxies have been studied extensively observationally, and in isolated wind tunnel simulations. In this work, we present a study on galaxy tails in some relatively unexplored areas: using a simulation (described in Chapter 2), we present an algorithmic method of tail identification and a statistical study on a large sample of galaxies. We also study the origins and time evolution of a set of visually identified jellyfish galaxies, and explore the role of ram pressure and other possible mechanisms in the formation of their tails.

In Chapter 2 we will characterize our sample of galaxies and discuss a series of general analysis methods used in the study. In Chapter 3 we will discuss our tail identification algorithm, representing a series of physically motivated velocity and density cuts. In Chapter 4 we present three sets of results:

- We perform some comparisons with existing statistical analysis done in Yun et al. 2019 and Roberts et al. 2021a with the tail orientations, and explore correlations between tail mass, star formation rate and ram pressure.

- We track the evolution of four specific jellyfish galaxies exhibiting well defined tails during infall. We track star formation rates, ram pressure, tail mass and disk mass over time, and explore how these quantities change with respect to each other.
- For a particular tail, we explore its origins and find evidence of entrainment and mixing as seen in Lee et al. [2022](#) and Choi et al. [2022](#). We explore a new mechanism of tail formation.

# Chapter 2

## Dataset and Methods

In this chapter we characterize our galaxy dataset and present a collection of methods used throughout this thesis, both for the purposes of tail identification in Chapter 3 and data analysis in Chapter 4. Unless otherwise specified, all methods are developed in python, using primarily the pynbody (Pontzen et al. 2013), numpy and scipy packages.

### 2.1 The Simulation Setup

This thesis uses a zoom-in simulation of a galaxy group (Joshi et al. 2019). This simulation was ran using the code Gasoline2 (Wadsley et al. 2017), a SPH code that includes physics such as star formation, radiative cooling and stellar winds as well as the superbubble feedback model (Keller et al. 2014). The initial conditions were generated using the code MUSIC (Hahn & Abel 2013) and standard  $\Lambda$ CDM cosmology where  $\Omega_\Lambda = 0.6914$ ,  $\Omega_M = 0.3086$ ,  $h = 0.6777$ ,  $n_s = 0.9611$  and  $\sigma_8 = 0.8288$  (Planck Collaboration et al. 2014). The 100 Mpc<sup>3</sup> simulation was initially run with dark matter only from  $z = 100$  to  $z = 0$ . A group of interest was

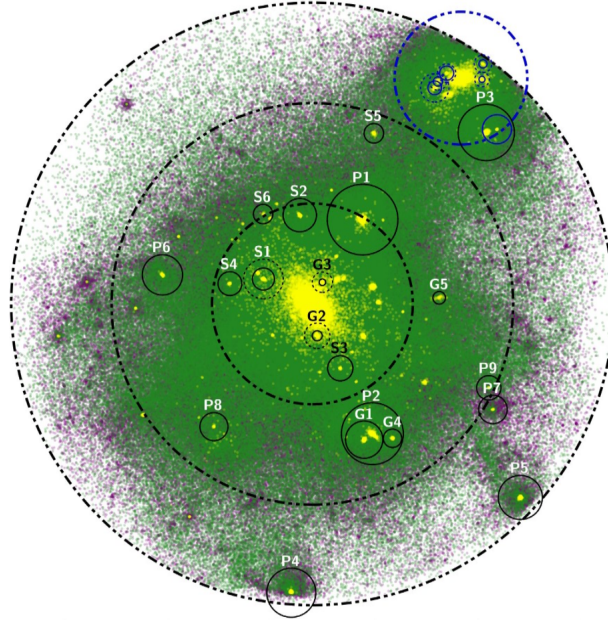


FIGURE 2.1: A projection of the simulation used for this study from Joshi et al. 2019. Dark matter particles are shown in purple, gas particles are shown in green, and star particles in yellow. The large black dotted rings represents 1, 2 and 3 virial radii of the group. The black circles represent a selection of individual halos.

identified, and tracing those the particles in that group at  $z = 0$  back to  $z = 100$ , the simulation was rerun with baryons included. At  $z = 0$  the group has a mass of  $1.87 \times 10^{13} M_{\odot}$  and a virial radius of 665 kpc, making it much smaller than rich cluster like Virgo. Within the high resolution zoom-in region, each baryonic particle has a mass of  $7.2 \times 10^5 M_{\odot}$  and each dark matter particle has a mass of  $3.9 \times 10^6 M_{\odot}$ . There are 128 snapshots in total, separated by 107.64 Myr. The full details of this simulation can be found in Joshi et al. 2019, and a projection of the group can be seen in Figure 2.1

## 2.2 Halos

In this section we discuss our setup for halos in preparation for analysis. This process involves extracting the particle data for each halo, and then performing a series of centering and orientation schemes.

### 2.2.1 Finding and Loading Halos

#### The Rockstar-Galaxies Problem

The Rockstar-Galaxies halo finder is chosen to identify halos (Behroozi et al. 2013). The halo finder has the benefit of employing a phase space friends-of-friends finder on both baryons and dark matter, which is feature lacking in both the original Rockstar halo finder as well as contemporary halo finders such as AHF (Knollmann & Knebe 2009).

Rockstar-Galaxies outputs consist of both particle data outputs and halo catalogues. The particle data outputs are binary files containing information on each particle in the simulation as read in and understood by Rockstar-Galaxies, while the halo catalogue consists of a list of halos and their general properties such as mass, position and velocity. To perform analysis using pynbody (Pontzen et al. 2013), it must be able to read in and understand the Rockstar-Galaxies particle data, and map it back to the simulation’s particle data, as well as the halo catalogue. The result is a list of halos, their properties, and all particles associated with the halo loaded into pynbody. Pynbody has been used successfully in reading the outputs of a number of halo finders, but integrating Rockstar-Galaxies into pynbody has proven to be a difficult task. We have been able to alter parts of

pynbody to load in both the Rockstar-Galaxies’ particle data and catalogues, but there were issues mapping the halo finder’s particle data onto the simulation’s particle data, resulting in the wrong particles associated with the halos. We were unable to adequately address this issue, so we proceed with a workaround

### The Workaround

Within the halo catalogues is a list of every halo’s position and virial radius ( $R_{\text{vir}}$ ), among many other properties.  $R_{\text{vir}}$  represents a radius within which the density represents some multiple  $\Delta_c$  of the critical density  $\rho_c$ . The virial overdensity parameter  $\Delta_c$ , as defined by Bryan & Norman 1998, can be expressed as:

$$\Delta_c = 18\pi^2 + 82x - 39x^2 \quad (2.1)$$

$$x = \frac{\Omega_{M,0}(1+z)^3}{\Omega_{M,0}(1+z)^3 + \Omega_\Lambda} - 1 \quad (2.2)$$

where  $\Omega_{M,0}$  represents the value of  $\Omega_M$  at  $z = 0$ .  $\Delta_c$  has a value of 102 at  $z = 0$  in this simulation given our cosmological parameters, but will vary depending on redshift. We can carve out a sphere of radius  $R_{\text{vir}}$  about the position of each halo, and choose all particles within this sphere to be those defining the galaxy. We then remove stellar subhalos by removing particles within  $3r_e$  (see Section 2.3.1) of subhalo positions as identified by Rockstar-Galaxies. We will reference information from the Rockstar-Galaxies halo catalogue when describing the overall properties of the halo such as stellar mass, position or gas mass, while for specific computations we will use the particles within the  $R_{\text{vir}}$  sphere. This definition is relatively loose, given  $R_{\text{vir}}$  is an idealized measure for local overdensities, and does not mean all particles within are bound. However, for the purposes of this work,

this approach is sufficient. Most of our particle-based computations are based on either the tightly bound stellar disk where there is no ambiguity on whether or not the particles are bound to the halo, or based on the large, asymmetrical tail (see Chapter 3) where the "boundedness" of the particles does not really matter.

## 2.2.2 Centering and Orienting

To perform proper analysis on and make mock images/maps of halos, we need to switch to the frame of reference of the halo, and choose a plane of projection to create 2D maps. These represent transformations and rotations of the particles' positions and velocities. In this thesis we need to orient galaxies such that one of its vector quantities of interest points along a principal axis: either orienting the angular momentum vector along  $\hat{z}$  or  $\hat{x}$  which projects the galaxy side on or face on respectively, or orienting the velocity vector along  $\hat{x}$  and the tail direction vector into the  $xy$  plane.

### The Galaxy's Frame of Reference

Centering a halo requires two translations: a positional translation such that center of mass sits at the origin, and a velocity translation such that the velocity of the galaxy is zero. The positional translation is straightforward to compute - the position of the center of mass  $\vec{r}_c$  is subtracted from the positions of all particles  $\vec{r}_i$ .

$$\vec{r}_{i,0} = \vec{r}_i - \vec{r}_c \quad (2.3)$$

The velocity translation is computed in a similar manner. The velocity of the galaxy is taken as the average velocity  $\vec{v}_c$  of star particles within a sphere of radius

1 to 3 kpc about the center of mass, with the translation applied to all particle velocities.

$$\vec{v}_{i,0} = \vec{v}_i - \vec{v}_c \quad (2.4)$$

The 1 kpc sphere is chosen to encapsulate the central bulge, but for smaller galaxies with fewer star particles, the sphere size is increased up to 3 kpc to include part of the stellar disk. The stellar bulge is chosen as the reference frame thanks to its stability.

### **Orientation and Projection**

Both orientation and projection involve solving for some rotation matrix  $\mathbf{R}$  which is applied to the position and velocity vectors of all particles in the halo:

$$\vec{r}_{i,0} = \mathbf{R}\vec{r}_i \quad (2.5)$$

$$\vec{v}_{i,0} = \mathbf{R}\vec{v}_i \quad (2.6)$$

Orientation of a galaxy involves some rotation such that some vector  $\vec{u}$  characterizing the galaxy is oriented onto some vector  $\vec{w}$  which is usually one of the cartesian principle axes. This can be accomplished via a change of basis  $\mathbf{B}$  such that  $\vec{u}$  and  $\vec{w}$  lie on a plane and then applying a standard rotation matrix  $\mathbf{R}_0$ .

$$\mathbf{R} = \mathbf{B}^{-1}\mathbf{R}_0\mathbf{B} \quad (2.7)$$

The standard rotation matrix depends on which plane  $\vec{u}$  and  $\vec{w}$  lie along in the new basis. If they lie along the  $xy$  plane in the new basis, the standard rotation matrix represents a rotation about  $\hat{z}$

$$\mathbf{R}_0 = \begin{bmatrix} \cos \theta & -\sin \theta & 0 \\ \sin \theta & \cos \theta & 0 \\ 0 & 0 & 1 \end{bmatrix} \quad (2.8)$$

We define matrix  $\mathbf{B}$  by the principles axes of the new basis in the original coordinates, which we construct using  $\vec{u}$  and  $\vec{w}$ .

$$\mathbf{B} = \left( \begin{matrix} \text{norm}(\vec{u}) & \text{norm}(\vec{w} - \vec{u}) & \text{norm}(\vec{u} \times \vec{w}) \end{matrix} \right)^{-1} \quad (2.9)$$

We allow  $\hat{x}$  in the new basis to point along  $\vec{u}$ , and let  $\hat{y}$  in the new basis line in the plane spanned by  $\vec{u}$  and  $\vec{w}$ .

Summarizing the process of orientation and defining the rotation matrix  $\mathbf{R}$  from Equation 2.7:

- $\mathbf{B}$  changes the basis such that  $\vec{u}$  and  $\vec{w}$  lie in the  $xy$  plane of the new basis
- In the new basis, apply the standard rotation matrix  $\mathbf{R}_0$  about  $\hat{z}$ . The angle  $\theta$  represents the angle between  $\vec{u}$  and  $\vec{w}$ .
- Finally, we return to our original basis with  $\mathbf{B}^{-1}$

As mentioned earlier, in this thesis galaxy orientation is done most commonly through orienting galaxy disks face on or edge on. The angular momentum vector

$\vec{L}_{\text{gal}}$  of the galaxy is aligned to  $\hat{z}$  for a face on orientation, or  $\hat{y}$  for an edge on orientation. In this case,  $\vec{L}$  would be  $\vec{u}$  and  $\hat{z}$  or  $\hat{y}$  would be  $\vec{v}$ .

To define a plane of projection, we require an additional initial vector  $\vec{v}$  such that  $\vec{u} \times \vec{v}$  define the normal. We define the two matrices  $\mathbf{P}$ ,  $\mathbf{Q}$  representing the initial and desired normalized vector orientations, supposing we wish to align  $\vec{u}$  with  $\vec{w}_1$  of some new orthonormal basis  $(\vec{w}_1, \vec{w}_2, \vec{w}_3)$  and such that the vectors  $\vec{u}$  and  $\vec{v}$  lie in the plane defined by  $\vec{w}_1$  and  $\vec{w}_2$ .

$$\mathbf{P} = \begin{pmatrix} \text{norm}(\vec{u}) & \text{norm}(\vec{u} \times (\vec{u} \times \vec{v})) & \text{norm}(\vec{u} \times \vec{v}) \end{pmatrix} \quad (2.10)$$

$$\mathbf{Q} = \begin{pmatrix} \vec{w}_1 & \vec{w}_2 & \vec{w}_3 \end{pmatrix} \quad (2.11)$$

We apply the Kabsch algorithm (Kabsch 1976) to determine the rotation matrix

$$\mathbf{H} = \mathbf{P}\mathbf{Q}^T \quad (2.12)$$

$$\mathbf{R} = (\mathbf{H}^T\mathbf{H})^{\frac{1}{2}}\mathbf{H}^{-1} \quad (2.13)$$

The Kabsch algorithm creates a rotation matrix that rotates column  $i$  in  $\mathbf{P}$  onto column  $i$  of  $\mathbf{Q}$ . In this thesis, projection is used to orient the galaxy's velocity onto  $\hat{x}$  and the galaxy's tail direction onto the  $xy$  plane. The vectors  $\vec{u}$  and  $\vec{v}$  are the galaxy's velocity  $\vec{v}_{\text{gal}}$  and tail direction  $\vec{r}_{\text{cen}}$  (to be discussed in Chapters 3 and 4). The columns of  $\mathbf{Q}$  are simply the principle axes  $\hat{x}$ ,  $\hat{y}$  and  $\hat{z}$  in cartesian coordinates, meaning the matrix  $\mathbf{Q}$  is the identity matrix  $\mathbf{I}$ .

## 2.3 Galaxy Properties

Now that we have loaded in the halos, let us derive some quantities of interest that will be relevant to our analysis.

### 2.3.1 The Effective Radius

To perform meaningful, normalized calculations across galaxies of various sizes and masses, it is important to define a characteristic radius. We define this characteristic radius to be the effective radius, representing the theoretical half-light/half-mass radius of the stellar disk. Our choice of a stellar mass effective radius allows for a stable, observationally relevant measure of a characteristic radius, from which we can study large fluctuations in the gas distribution without having those fluctuations affecting our characteristic radius.

We define the effective radius  $r_e$  as the stellar half mass radius, where

$$\frac{M(< r_e)}{M_{\text{tot}}} = 0.5 \quad (2.14)$$

We compute  $r_e$  using an expanding sphere method, iterating over a range of radii between  $0 < r < R_{\text{vir}}$ , centered about the position of the halo as identified by Rockstar-Galaxies. At iteration  $i$  we perform the following calculation and check

$$M_i = \sum_{r_n < r_i} M_n(r_n), \quad M_i/M_{\text{tot}} \leq 0.5 \quad (2.15)$$

where  $M_n(r_n)$  refers to individual star particles at a distance  $r_n$  from the center. We iterate over larger and larger spheres, computing the mass inside the sphere

and comparing it to the total stellar mass. Once the ratio reaches or exceeds 0.5, we take the resulting  $r_i$  as the effective radius  $r_e$ . This method is only applicable for sufficiently large number of particles and for a (at least roughly) spherically symmetric or axisymmetric stellar distribution. Beyond this, our expanding sphere method make no assumptions on the stellar distribution. This allows us to calculate an effective radius for both lower resolution, blob-like galaxies and higher resolution disk-like or elliptical galaxies.

### **2.3.2 The Disk**

For the purposes of this work we need to isolate the ISM from the galaxy’s environment. We can characterize a size for the stellar distribution based on the effective radius. After much exploration across all galaxies in our sample (to be discussed later this chapter), we determined a radius of  $3r_e$  to be the optimal definition for the disk. Since we make no assumptions on the shape of the stellar disk, the  $3r_e$  cut is applied radially, meaning the disk represents a sphere of radius  $3r_e$  about the center of the galaxy.  $3r_e$  was chosen to be a minimal radius that captures the entire stellar distribution of as many galaxies as possible such that the stellar properties are not sensitive to this choice, though properties of the less tightly bound ISM are sensitive to this choice. Figure 2.2 shows a schematic summarizing our defined regions and scale lengths for a halo.

### **2.3.3 Star Formation Rate**

Traditionally, star formation rates have been calculated using the stellar mass. Each star particle tracks its own time since formation  $t_{\text{form}}$ , so a rough SFR can

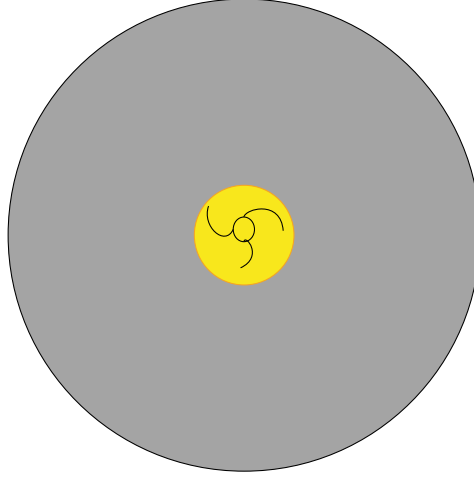


FIGURE 2.2: A rough schematic of a halo. The outer black circle represents the virial radius of the halo at  $R_{\text{vir}}$ ; the inner orange circle on the boundary of the yellow region represents the spherical "disk" at  $3r_e$ ; the grey and yellow coloured regions roughly represent the CGM and ISM.

be calculated by looking for star particles with  $t_{\text{form}} < t_{\text{step}}$  ( $t_{\text{step}} = 107.64$  Myr). However this method has two flaws:

- The SFR has a lower limit defined to be:

$$\text{SFR}_{\text{lim}} = \frac{M_{\text{baryon}}}{nt_{\text{step}}} \quad (2.16)$$

which represents a single gas particle collapsing and forming a star particle within  $n$  timesteps. For a single timestep this works out to be roughly  $6.7 \times 10^{-3} M_{\odot} \text{Yr}^{-1}$ . Galaxies with a lower single timestep SFR will show no star formation. While multiple timesteps would allow us to probe lower SFRs, it also averages the state of a galaxy over a large time window, making the SFR less reflective of the galaxy's current state.

- This measure of SFR relies on star particles, and cannot probe star formation in regions without star particles. This limits where we can detect star formation in our simulation.

To account for these limitations we devised an alternative method for calculating star formation rate using the properties of the gas particles. A similar approach is used by studies employing the Gadget2 Code (Bischof et al. 2015, Springel & Hernquist 2003). We provide two prescriptions to each of the two flaws above

- Based on the state of a gas particle, Gasoline2 will assign a certain probability of a gas particle collapsing into a star particle. We convert this probability into a measure of star formation - specifically a  $X\%$  chance of turning into a star particle represents  $X\%$  of the gas particle that is star forming over a single timestep. This prescription allows us to probe star formation in gaseous regions.
- Star formation can only occur when certain criteria are met, such as a sufficiently high density. This means that for most gas particles, the star formation probability will either remain at zero, or fluctuate between zero and some small positive value. To account for these fluctuations, instead of using the instantaneous value of this star formation probability, we average this value for a given particle across four snapshots representing a total time window of around 321 Myr ( $3t_{\text{step}}$ ). This prescription can also be applied to the traditional method of using star particles to lower the limit to  $2.23 \times 10^{-3} M_{\odot} \text{Yr}^{-1}$ .

We can compare the results of both SFR calculations in Figure 2.3. Overall

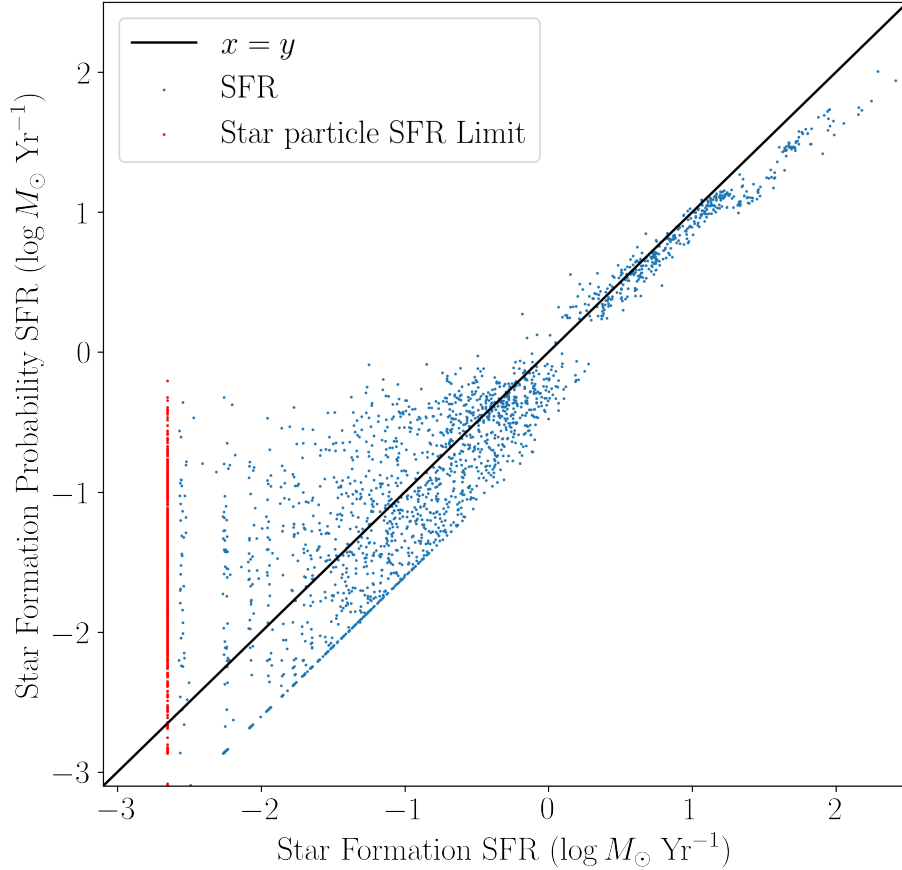


FIGURE 2.3: A scatter plot comparing the star formation rates of galaxies as calculated using star particles versus using the star formation probability in gas particles. These galaxies are well resolved and chosen between  $z = 0.67$  and  $z = 0$  (Further discussion of our sample in Section 2.5). In blue are all galaxies exhibiting non zero SFRs using both methods, and in red are all galaxies exhibiting zero SFR using star particles but non zero SFR using gas particles - their values on the  $x$  axis are set to the star particle SFR floor of  $2.23 \times 10^{-3} M_{\odot} \text{Yr}^{-1}$ . Out of a total of 4548 galaxies, 3148 exhibit non zero SFR using gas particles, and 2023 exhibit non zero SFR using star particles.

we see that the distribution of SFRs derived from the star formation probability is more continuous compared to the SFRs derived from the star particles, though there remains some stochasticity in the former, in the clumps of blue points near the bottom left. We are also able to probe star formation in galaxies where the

traditional method would show no star formation, though interestingly the SFRs of the red points are not significantly below the SFR floor mentioned earlier, with only 221 of the extra 1125 galaxies with non zero star formation actually showing SFR below the floor. In conclusion, while this method does help probe lower SFRs in a small fraction of cases, it primarily allows us to probe non-zero SFRs in more galaxies, and probe SFRs in regions with no star particles.

### 2.3.4 Ram Pressure and the Modified Stripping Criterion

A computation of the ram pressure requires a consistent definition of the group medium. We choose a half-shell with a thickness of 30 kpc in front of the halo and centered about the galaxy’s velocity vector. The inner radius and outer radius of the shell are  $R_{\text{vir}} - 30$  kpc and  $R_{\text{vir}}$  respectively. Mathematically, our hemispheric shell domain  $D$  can be expressed as:

$$D = \vec{v}_{\text{gal}} \cdot \vec{r}_{\text{particle}} < 0, R_{\text{vir}} - 30 \text{ kpc} < |\vec{r}_{\text{particle}}| < R_{\text{vir}} \quad (2.17)$$

To compute the ram pressure, we require the density and velocity of the galaxy relative to the medium. The density is computed by dividing the total mass of all gas particles in  $D$  by the volume of  $D$ , while the velocity is taken as the average velocity of all gas particles in  $D$  in the rest frame of the galaxy.

$$P_{\text{ram}} = \rho \bar{v}^2 \quad (2.18)$$

$$= \left( \sum_{\vec{r}_n \in D} dM_n \right) V_D^{-1} \left| \sum_{\vec{r}_n \in D} \vec{v}_n \right|^2 \quad (2.19)$$

The gravitational force per unit area  $2\pi G\Sigma_s\Sigma_g$  (Gunn & Gott 1972), as discussed in Chapter 1, can be compared to the ram pressure to determine whether or not the gas in a galaxy is likely to be stripped. However, resolution limits prevent us from computing surface densities near the edge of the disk, where we would expect gas to be most prone to stripping effects.

We modify the stripping criterion to compare acceleration instead of pressure, and move from cylindrical geometry to spherical geometry. Modeling ram pressure as a force acting across some surface with some area (in this case the projected area of the galaxy's ISM), we can derive a "ram acceleration":

$$a_{\text{ram}} = \frac{P_{\text{ram}}}{\Sigma_{\text{gas}}} \quad (2.20)$$

We define  $\Sigma_{\text{gas}}$  as the average surface density of the galaxy

$$\Sigma_{\text{gas}} = \frac{M_{\text{disk}}}{\pi(r_{\text{disk}})^2} \quad (2.21)$$

Finally, we define the modified stripping criterion as a dimensionless ratio between the ram acceleration and gravitational acceleration:

$$S = \frac{a_{\text{ram}}}{a_{\text{grav}}} \quad (2.22)$$

$$= \left( \frac{P_{\text{ram}}}{\Sigma_{\text{gas}}} \right) \left( \frac{GM(< r_{\text{disk}})}{r_{\text{disk}}^2} \right)^{-1} \quad (2.23)$$

The order of magnitude of this stripping criterion tells us how prone to stripping a galaxy is. This value can be compared across all tailed galaxies with varying properties.

## 2.4 Group Characteristics

Before proceeding with analysis let us first characterize our group. We cut galaxies below  $10^8 M_\odot$  in stellar mass (representing approximately 150 star particles) to eliminate low resolution galaxies, and galaxies outside 2 virial radii to eliminate far away galaxies not associated with the group. As we can see in Figure 2.4, while ICBS cluster and EDisCS group survey data (Vulcani et al. 2013) show a plateau in the mass function for  $M_* < 10^{11} M_\odot$ , our group shows a steady linear trend upwards with decreasing mass. This discrepancy could indicate that our group is disproportionately dominated by low stellar mass objects, but a very small sample of well resolved galaxies within 2 virial radii makes it difficult to state this confidently.

In Figure 2.5 we see that our group lies very clearly above the CFHTLenS derived stellar halo mass function (Hudson et al. 2015). We see a stellar mass fraction an order of magnitude greater than expected. This indicates insufficient amounts of feedback, causing runaway star formation. This group has a lack of galaxies above  $10^{12} M_\odot$  in halo mass, with most galaxies concentrated between  $10^{10} M_\odot$  and  $10^{11} M_\odot$  (an approximate stellar mass range of  $10^8 M_\odot < M_* < 10^{10} M_\odot$ ).

Overall, we can characterize our group as one dominated by lower mass galaxies with disproportionately high stellar mass fractions across all mass ranges. One possible explanation for a part of this enhanced star formation is the lack of AGN feedback present in the simulation, which is known to quench higher mass galaxies (Tremmel et al. 2017).

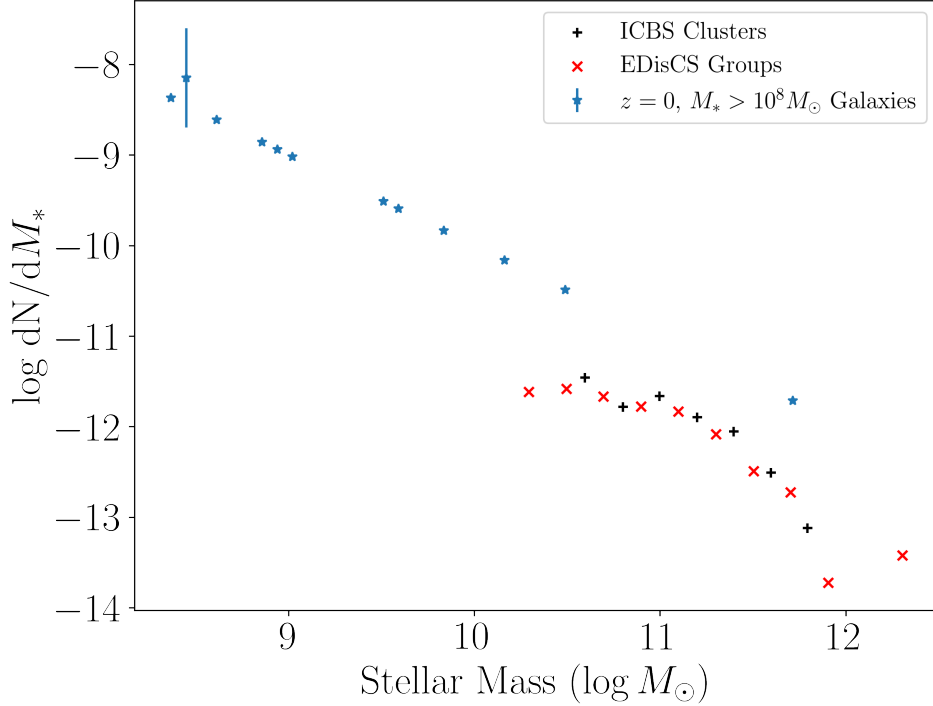


FIGURE 2.4: Stellar mass function of  $M_* > 10^8 M_\odot$  galaxies at  $z = 0$ , normalized by mass. ICBS cluster stellar mass functions and EDisCS group stellar mass functions are also shown (Vulcani et al. 2013). Error bars are  $\sqrt{N}$ , with no error data points representing single galaxies. The normalized values do not matter - what matters are the shapes of the mass functions.

## 2.5 The Galaxy Sample

In each snapshot, there are only approximately 300 or so galaxies with stellar mass, and less than 100 or so with a mass above  $10^8 M_\odot$  and relatively well resolved. This limits our ability to do statistics on our sample. However we are not necessarily restricted to  $z = 0$  - we have access to a wide range of timesteps from  $z = 100$  all the way to the present day. We choose our sample to include all galaxies from  $z = 0.67$  to  $z = 0$ , meeting the following criteria

- The galaxy is not the central BGG

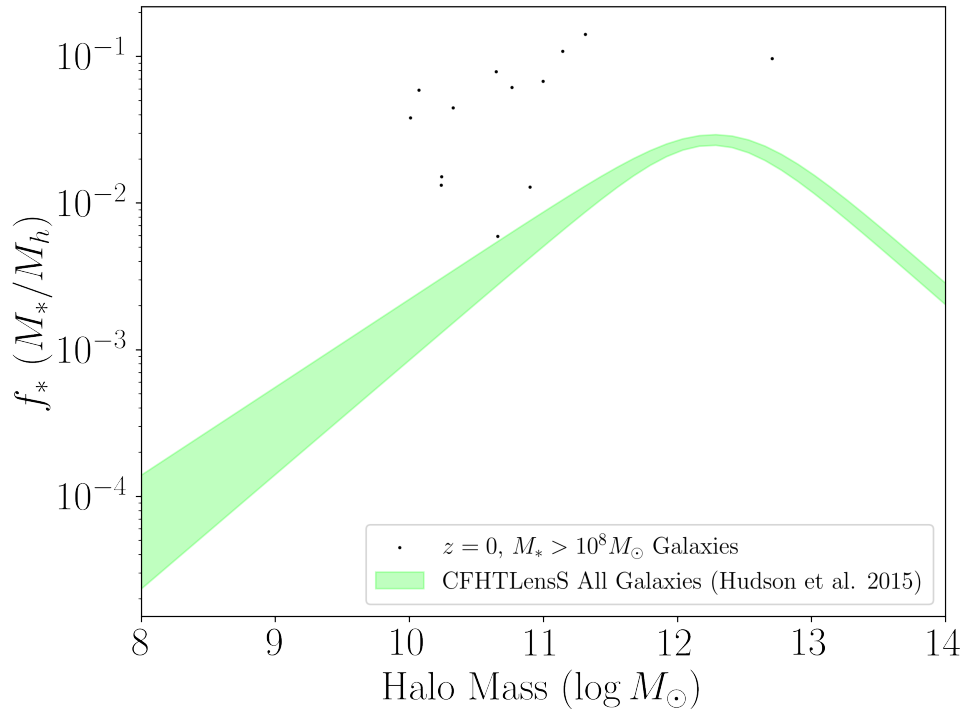


FIGURE 2.5: Stellar halo mass relation of  $M_* > 10^8 M_\odot$  galaxies at  $z = 0$ . A double power law fit of CFHTLenS data is also shown (Hudson et al. 2015). The y axis shows the stellar mass as a fraction of the total halo mass. The diagonal cut represents both the  $M_* > 10^8 M_\odot$  cut and the resolution limits of lower mass galaxies.

- The halo position is correctly identified by the halo finder and contains a stellar disk surrounded by gas (There were instances of the halo finder providing the incorrect location for a halo, resulting in no star and few gas particles loaded in)
- The galaxy has no low resolution dark matter particles
- The galaxy has a stellar mass above  $10^8 M_\odot$
- The galaxy has more than 20 gas particles (approximately  $10^7 M_\odot$  in mass)

The result is a large sample of 4548 well resolved galaxies, with large populations of stellar and gas particles. Unfortunately, a major issue we encounter is that our galaxies are not independent from each other. Galaxies are heavily correlated with their progenitors and descendants, especially across adjacent snapshots. The result is that any distribution in some derived quantity such as star formation rate will be dominated by small group of galaxies with a high number of repeat occurrences, and it will not be representative of our group. To do meaningful statistics on 4548 galaxies across 58 snapshots, we apply a weight that depends on the number of each galaxy’s occurrence in the sample, as will be discussed in the following sections.

### **2.5.1 Merger Trees**

Since we are using galaxies across multiple snapshots, it is not sufficient to simply store galaxy data using 2D arrays, since we need to determine which galaxies represent the same galaxy across different times. We use the n-ary tree data structure in this case to connect the galaxies across different snapshots, a simple version of which is shown in Figure 2.6. The Rockstar-Galaxies halo catalogues provide the IDs of each halo in each snapshot, as well the ID of the descendant halo in the next snapshot. Using this descendant information but in reverse, we build merger trees for all galaxies starting at the  $z = 0$  galaxies. If we were to track every single galaxy, a list of root nodes at  $z = 0$  would capture all galaxies in all snapshots - however using our filters as discussed above means galaxies at  $z = 0$  that were cut, or galaxies that merged with the central BGG right before  $z = 0$  will have their entire trees missing, even if progenitors of these objects do survive our resolution cuts and are included in our sample.

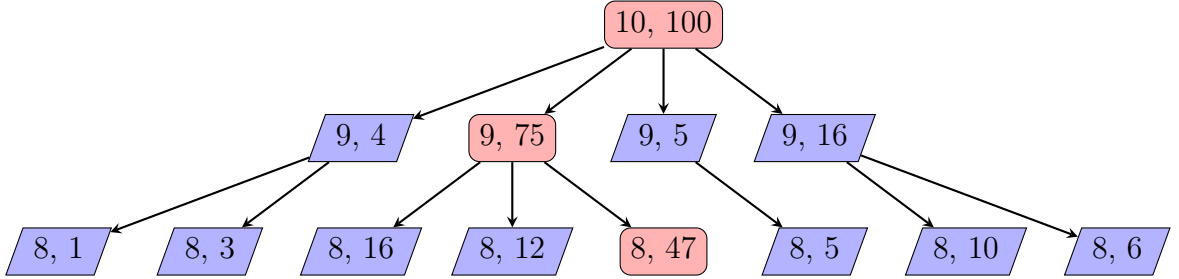


FIGURE 2.6: A simplified visualization of a merger tree. Each node represents a halo, with the two numbers representing the time (left) and mass (right). For a given halo, the halos it points to one level down represent direct ancestor halos that will merge and form the given halo, with the halo mass in each node is split among its direct ancestors. For the purposes of tracking halos over time, each halo is also linked to its most massive child. The pink rounded rectangles represents a single halo tracked over time, with the blue parallelograms represent other halos that will merge onto the tracked halo. A better visualization of the time tracking of multiple individual halos can be seen in Figure 2.8

As a quick sidenote, we will be using the terms node and halo interchangeably in this section. We capture a merger tree using the n-ary tree data structure such that each node represents a halo. The parent node represents the direct descendant halo, and the child nodes represent the direct ancestor halos.

To account for these missing halos, we build merger trees for all halos. Iterating through all halos in our sample, we start at  $z = 0$  and go back in time. At each iteration, we check whether or not the current halo resides in an existing merger tree. If so, we skip the current halo, and if not, we build a merger tree. The result is a list of over a hundred unique merger trees spanning  $z = 0.67$  to  $z = 0$ . Most of these merger trees start within the latest few snapshots around  $z = 0$ , with around a dozen or so merger trees starting earlier than  $z = 0.3$ . Merger trees that start before  $z = 0$  represent halos at  $z = 0$  that failed our resolution cuts but have ancestors that survive our resolution cuts.

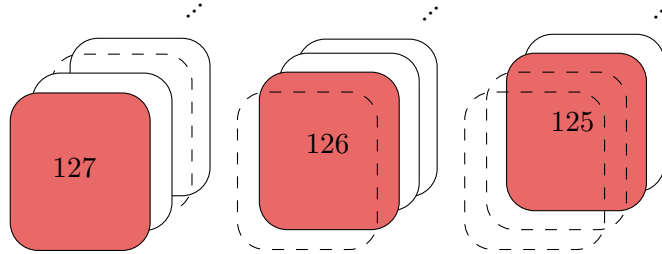


FIGURE 2.7: A representation of the evolutionary history of three halos. The pink square represents the latest time the halo exists at in our sample, with squares behind it representing the halo at earlier times. A dotted square represents a descendant or ancestor of the pink square halo that is excluded from our sample. Our merger trees account for ancestor halos not in our sample (left stack), as well as  $z = 0$  halos not in our sample but whose ancestors are in our sample (middle and right stacks).

Our merger trees include all ancestors from the catalogues, with galaxies that do not exist in our sample having a flag. This accounts for the existence of holes in our merger trees, where a certain galaxy may be cut from our sample but its direct ancestor or descendant is not. Figure 2.7 shows a simple visualization of these holes using a single halo and its descendants. We will refer to the long chain of the most massive ancestors (child nodes) of a given node in a merger tree as a branch.

### 2.5.2 Ancestor Tracking and Branches

As discussed earlier each node is linked to its most massive child node. Physically that child node would represent the direct ancestor halo in the previous snapshot. Repeating this process for a node creates a long chain of halos representing the time evolution of a single halo, which we call a branch. For the less massive children of some node, we apply the same process - among its child nodes (AKA its ancestor halos), we link it to its most massive child. This entire process is done recursively

on all nodes in the merger tree. For a single halo with multiple ancestors, that halo and its most massive ancestor represent two nodes along a larger branch (possibly the beginning of the branch), while the less massive ancestors represent the beginnings of their own branches.

Branches are tracked by a count stored in each node. This count is initialized to 0 at the root node, and increments up by one along its branch by checking all child node masses and incrementing only the count value of the most massive child node, setting all other child node count values to zero. The result is a count value in each node specifying the number of nodes before it along the branch, with the count value at the end of the branch (at the earliest time) representing the total length of the branch. Tracking this count value allows for easy traversal along branches, as well as extraction of branches for time evolution analysis from any node to any other node.

While a single count is more than sufficient for a general merger tree, it is not sufficient for our merger trees with holes. As a reminder, these holes are galaxies that exist in the halo catalogues and full merger trees, and are either the result of halos eliminated due to failing the resolution cuts, or a classification-based cut <sup>1</sup>. To account for these holes, we store additional values in our nodes - specifically two additional count values, an integer from 1 to 4, and a boolean. The integer from 1-4 labels the class the galaxy belongs to. During the building of our merger trees, we check if the galaxy in the current node is a part of our sample and classification of interest. The boolean is marked True or False depending on if the galaxy is in our sample; our sample count increments up by one if the direct

---

<sup>1</sup>To be discussed in more detail in Chapter 4 but our sample is also divided into four classes. These can be individually treated as an additional cut to our sample

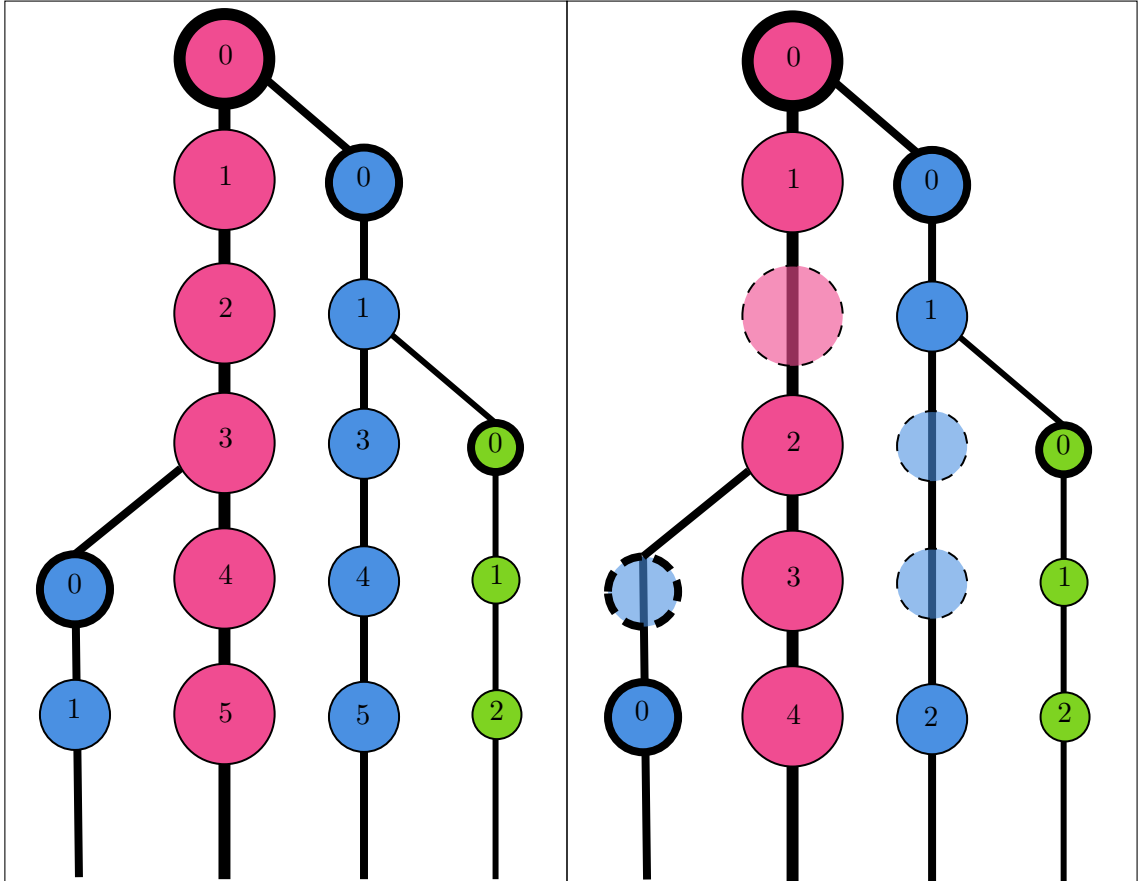


FIGURE 2.8: A diagram illustrating branches and subbranches. Here we refer to the branches originating from the child nodes of some node in a branch as subbranches. The node representing the beginning of each branch is shown with a thick black outline, and the number on each node shows the count. The figure on the left shows a merger tree with no holes and a total count, while the figure on the right shows a merger tree with holes and the modified count. The varying colours and sizes represent separate branches - the blue branch originates from an ancestor of a halo along the pink branch, and the green branch originates from a direct ancestor of a halo along the blue branch (these ancestor halos are not the most massive ancestor, hence they represent the beginning of distinct branches as opposed to the direct ancestor of original halo). When there are holes present, the sample/class count value is held constant when traversing a branch until a galaxy present in the sample/belonging to the class is encountered.

progenitor is in our sample, and remains constant otherwise; our classification count increments up by one if the direct progenitor has the same class label as the root node, remaining constant otherwise. The boolean and class integer essentially act as flags, telling us whether or not to include a specific node in their respective counts. A comparison between a "full" merger tree using total count vs our holed merger tree using sample/class count can be seen in Figure 2.8.

### **2.5.3 Branch Length and Weighting**

Using this aforementioned count value, we can not only track branches, but also determine the length of a branch starting from any node along it, without the need to track down the root node. Since the count stores the number of nodes between itself and the root node, we only need to march along the branch back in time until the end, where the count value at that node is one less than the length of the branch.

With branch length we can now properly weight each galaxy. As mentioned previously, it would be difficult to perform proper statistics on our sample of galaxies without any form of weighting since galaxies are heavily correlated with their direct ancestor and descendant - any irregularities at one given snapshot are magnified as those galaxies are captured over and over again in the sample, creating statistical results that do not exist.

An initial approach one can take is to weight these galaxies by their branch length - galaxies with branch length  $N$  will have a weight  $N^{-1}$ . This is equivalent of treating every galaxy along a branch as the same galaxy. However, objects may undergo significant evolution throughout their lifetimes. It would be unreasonable

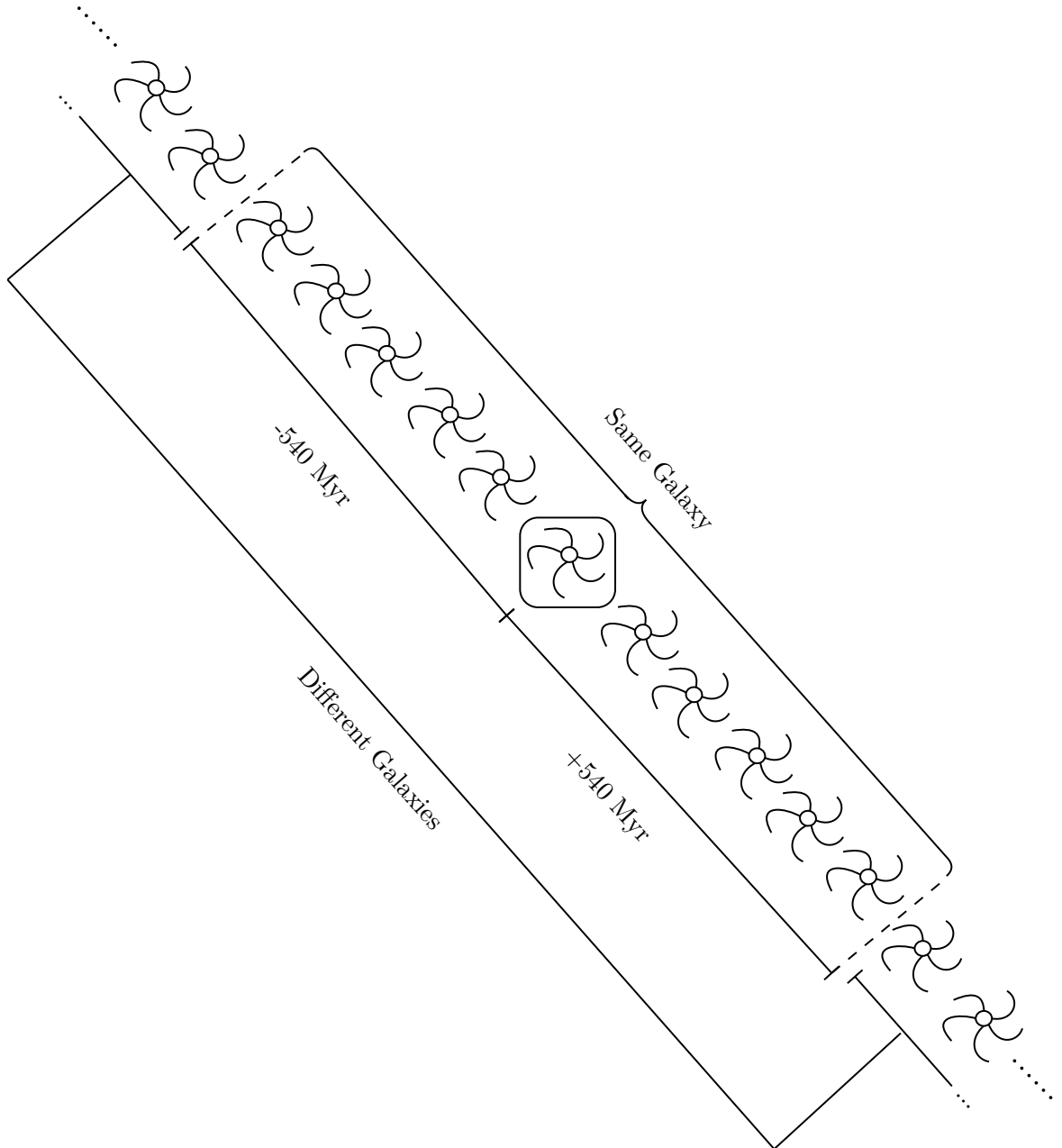


FIGURE 2.9: A schematic of our weighting scheme. The line of galaxies represents galaxies along some branch. The galaxy of focus (enclosed in the rectangle) is defined by the same as at most the 5 galaxies forwards and backwards along the branch.

to consider a galaxy far out from the group with a healthy CGM, and that galaxy’s descendants a few Gyrs later that is now within the virial radius and gas depleted, to be the same galaxy. To account for this we apply a simple adjustment: we set a lower bound of the weight to be 0.1. This lower bound was chosen such that the galaxy is the same object as objects 5 snapshots forwards and backwards along its branch, and different from all other objects along its branch (see Figure 2.9). This solution accounts for both the uniqueness of galaxies along a branch with a large temporal separation while still allowing for dynamic weighting of short branches.

#### 2.5.4 Sample Characteristics

With our sample and weights defined, we examine some characteristics of our sample. In Figure 2.10 we can see that the stellar mass-halo mass relation of our sample remain higher than those of Hudson et al. 2015. We also observe string-like trends, which indicate repeat sampling of the same galaxy across different times. Examining Figure 2.11, we see that our sample shows a near identical stellar mass function to the  $z = 0$  galaxies, with the same linear count increase towards lower stellar mass.

Figure 2.12 shows the star forming main sequence for our sample of galaxies. Our star forming main sequence matches relatively well with sequences of field galaxies such as SDSS (Elbaz et al. 2007) and COSMO2015 (Laigle et al. 2016), while being lower than the SpARCS (Nantais et al. 2020) sequence of clustered galaxies. What’s immediately obvious is a lack of fully quenched galaxies, with all galaxies lying above the green valley (Martin et al. 2007).

The horizontal lines on the dot plot show some of the stochasticity seen in

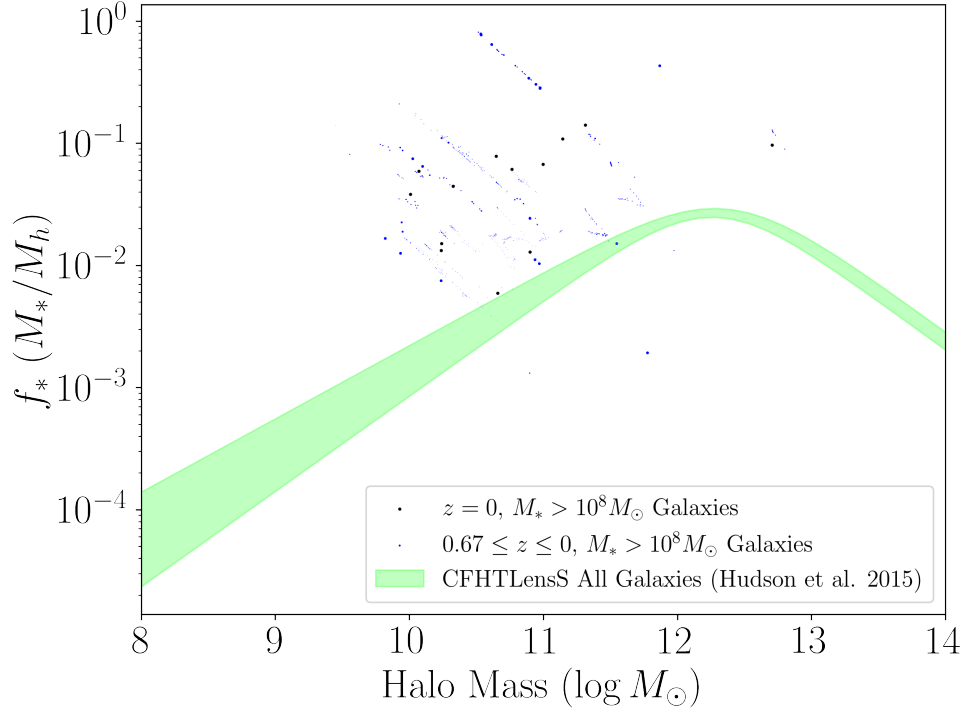


FIGURE 2.10: Stellar halo mass relation of our sample of galaxies from  $z = 0.67$  to  $z = 0$ . The same relation for the  $z = 0$  galaxies in Figure 2.5 is shown, alongside the double power law fit of CFHTLenS data (Hudson et al. 2015). The size of each dot is scaled by each galaxy’s weight

the blue clumps of points in Figure 2.3. The vertical string-like trends reflect similar features in Figure 2.10, where the same galaxy is sampled repeatedly across different snapshots. As mentioned in an earlier section, out of the 4548 galaxies in our sample, 3148 register non-zero SFR.

While there appears to be indications of some galaxies moving off the main sequence, there are no red and dead galaxies. There are likely three reasons:

- Despite our attempts of boosting our sample using multiple snapshots, we are still examining one galaxy group. Merger tree branch length weighting

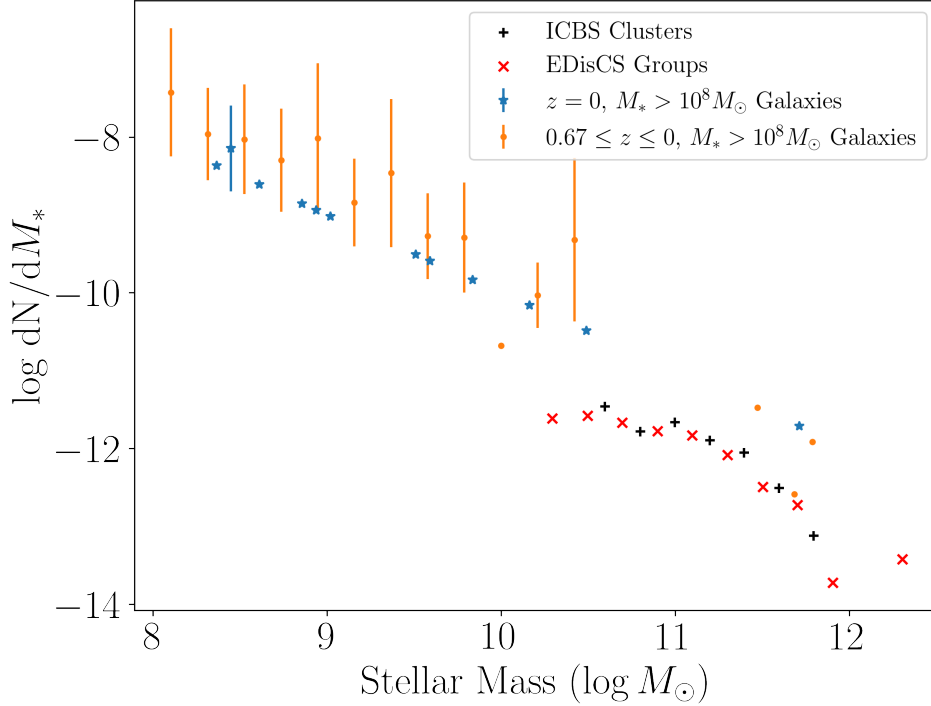


FIGURE 2.11: Stellar mass function of our sample of galaxies from  $z = 0.67$  to  $z = 0$  shown in orange and normalized by mass. The same relation for the  $z = 0$  galaxies in Figure 2.4 is shown in blue, alongside ICBS cluster stellar mass functions and EDisCS group stellar mass functions (Vulcani et al. 2013). Error bars are  $\sqrt{N}$ -data points with no error bars indicate only a single galaxy exists in those mass bins. The normalized values do not matter - what matters are the shapes of the mass functions.

doesn't make our sample more representative of a galaxy group dominated by low-medium mass galaxies.

- The high star formation rates reflect what we saw earlier in Figure 2.10 where galaxies had disproportionately high numbers of stars. As mentioned earlier, this simulation does not have AGN feedback, which is known to be a significant source of quenching for larger galaxies (Tremmel et al. 2017). Without this additional source of feedback, larger galaxies (mainly those

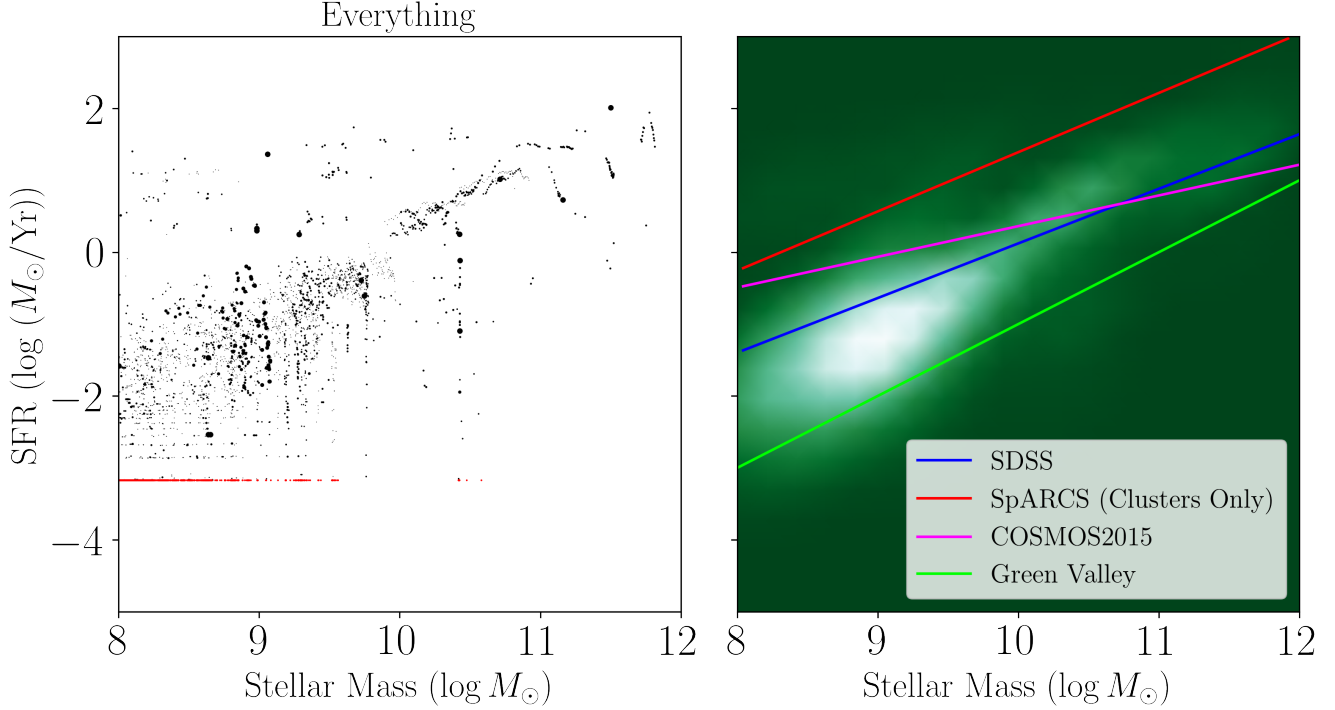


FIGURE 2.12: The star forming main sequence of our sample. The left shows a weighted dot plot where each dot represents a galaxy. The size of each dot is scaled based on each galaxy’s weight, as described in Section 2.5.3. 0 sfr galaxies are shown in red, with their sfr values set to the minimum positive sfr. The right shows a gaussian kernel density estimate of the left plot. Star forming main sequences from SDSS blue galaxies (Elbaz et al. 2007), SpARCS clusters (Nantais et al. 2020) and COSMOS2015 galaxies (Laigle et al. 2016) are plotted on the right. The star forming green valley is shown in lime, representing a star formation rate of  $10^{-11} M_*$  (Martin et al. 2007).

with halo masses above  $10^{12} M_{\odot}$  are likely to see runaway star formation (Keller et al. 2016b).

- When it comes to smaller quenched galaxies, resolution limits prevent us from probing their star formations. As we saw in Figure 2.3, we were not able to probe much star formation below  $2.23 \times 10^{-3} M_{\odot} \text{ Yr}^{-1}$  despite using the star formation probability of gas particles. The lowest non-zero specific

star formation a low mass  $10^8 M_\odot$  galaxy would register is around  $10^{-11}$ , which is right on the green valley.

## 2.6 Explored Unused Numerical Methods

In this section we briefly discuss some alternative methods used for certain computations that were later discarded due to resolution limits or being overly complex. We recommend exploration of these methods in future work.

### 2.6.1 The 6-D Phase Space Convex Hull

A convex hull represents a  $N$ -dimensional convex polygon consisting of the outermost points of a set of points in  $\mathbb{R}^N$ . Every point in the set is contained within, or on the surface of, the hull.

We explored this method in our process of developing a tail identification algorithm (see Chapter 3). Our goal is to identify particles that live close to a pre-selected subset of particles in phase space. This subset consists of particles above a certain threshold, such as density or temperature. We build a convex hull using that subset of particles, and check which particles in the entire set fall within this convex hull

We designate a phase space coordinate  $\vec{w} = (\vec{r}, \vec{v})$  for each particle. We define some subset of particles, and using the QuickHull Algorithm ([Barber\\_1996](#)), we build a 6D convex hull around this subset. To determine whether or not a point  $\vec{w}$  lies within this hull, we check for intersections between the Delaunay triangulation for this convex hull and  $\vec{w}$ .

The convex hull was explored as a method of tail identification (see Chapter 3), but was ultimately rejected in favour of simpler and better physically motivated methods

## 2.6.2 The Impulse Criterion

Similar to the stripping criterion, the impulse criterion is a ratio between a stripping force and a gravitational restoring force. In this case, that stripping force is neighbour-neighbour tidal force, which may occur for galaxies flying by each other. For two isolated bodies of masses  $m$  and  $M$ , the expected tangential velocity perturbation for mass  $m$  in the frame of mass  $M$  (Binney & Tremaine 1987) can be expressed as

$$|\delta v_{\perp}| = \frac{2mbv_0^3}{G(M+m)^2} \left( 1 + \frac{b^2v_0^2}{G^2(M+m)^2} \right)^{-1} \quad (2.24)$$

where  $b$  is the impact parameter and  $v_0$  is the initial velocity.

Attempts were made to compute this impulse, including attempts at adapting Equation 2.24 for the galaxies in our sample and attempts to compute the sum of all tidal forces acting on a galaxy. We were unable to adequately characterize impulse so this was not taken into account.

# Chapter 3

## Tail Identification

In this chapter we discuss our process of identifying the gas particles of galaxy tails, with a physically motivated series of phase space particle cuts, which can be applied algorithmically across all galaxies.

### 3.1 Motivation

As discussed in Chapter 1, observational methods of jellyfish tail identification involve studying emissions from gas tracers such as HI. Such techniques can be replicated with simulation data through the use of mock maps, where the 3D gas density distribution is projected onto a 2D plane followed by post processing in the form of SPH-based smoothing (Pontzen et al. 2013) or convolutions with a simulated aperture/beam. While this would be faithful to observational techniques, they would share the same problems:

- Tail identification through mock maps is heavily dependent on the orientation of the galaxy. Tails with significant components along the line

of sight will be more difficult to accurately identify than tails that lie in the plane.

- Visual identification can be time consuming across large sample sizes, and subject to individual biases.

Additionally, our goal with this study is to probe the properties and formation mechanisms of galaxy tails in depth using simulated galaxies, so we need not limit ourselves to observational constraints. Thus, we opt for an identification method based on the properties of gas particles, making full use of the simulation’s available phase space information for each particle. Full use of 3D positional data resolves any issues with orientation, and algorithmic identification resolves both the time consumption and human biases of visual identification. The algorithm used to identify the tails consists of a series of density, velocity and temperature based cuts described in the next sections. These cuts will be motivated by studying the properties of a series visually identified jellyfish galaxies, which will also be used to tweak and constrain these cuts.

The result is a physically-motivated algorithm that is optimized to isolate tail particles for jellyfish galaxies, but can be applied to any tailed galaxy. We will explore the tailfinding algorithm in detail in this chapter. To illustrate the our process of picking and constraining our particle cuts, we primarily examine the prominent jellyfish galaxy 648-1286, but these features are shared across many tailed and jellyfish galaxies.

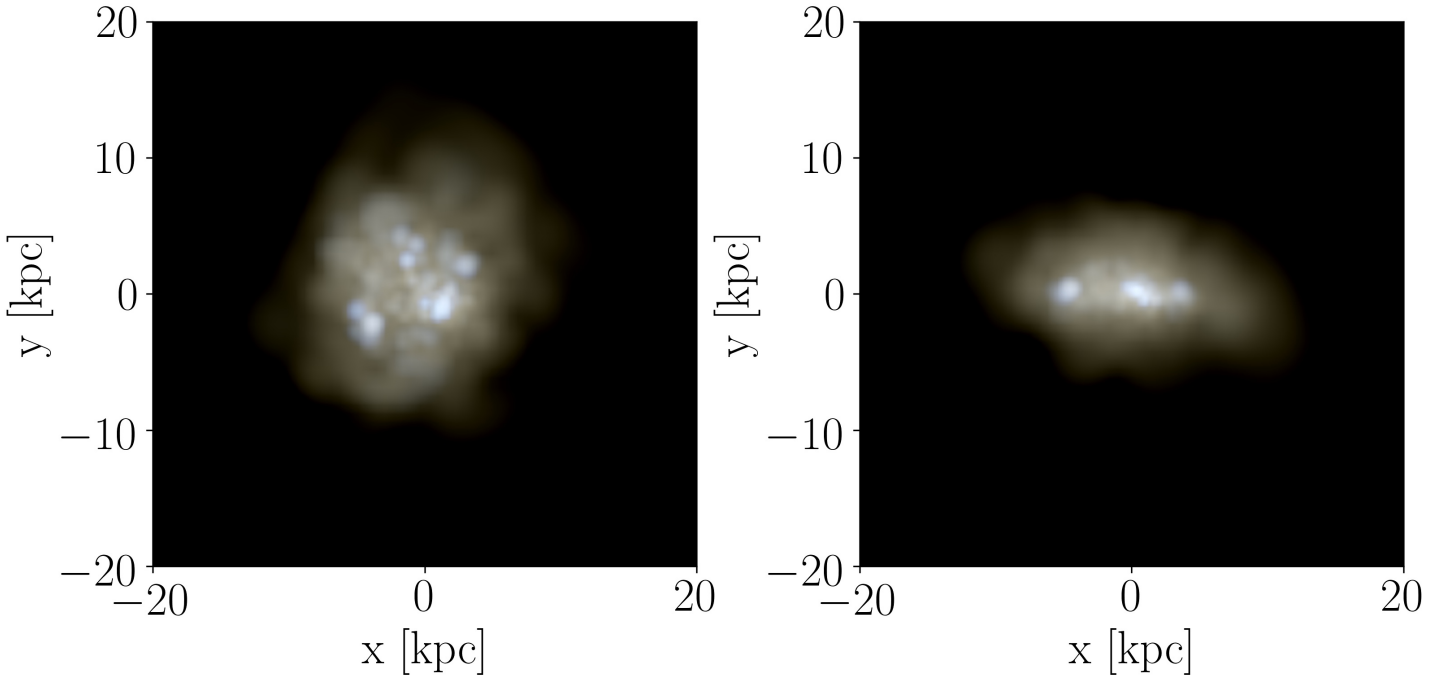


FIGURE 3.1: Optical mock images for galaxy 648-1286, representing the R, G and B colour bands. The left shows the galaxy oriented face on (see Section 2.2.2) about its angular momentum  $\vec{L}_{\text{gal}}$ , and the right shows the galaxy without any orientation applied (as it is in the simulation). This galaxy is relatively low mass with  $M_{\text{star}} \approx 10^{9.08} M_{\odot}$ , and has a disk-like morphology. This galaxy is shown at  $z \approx 0.5$  with a cluster-centric distance of 0.9 virial radii. It is falling into the group center.

## 3.2 Observable Features of a Jellyfish Galaxy

In Figure 3.1 alone, the galaxy looks like an unremarkable galaxy lacking in any interesting structure. However, it is when we zoom out and examine the gas that we begin to see significant extended structures. In Figure 3.2, we see highly asymmetrical tail like structure distinct from the background medium, with a characteristic length on order of  $R_{\text{vir}}$ , far exceeding the effective radius of the disk.

The relative density of this tail combined with a bow-like morphology towards the upper-left of the disk, strongly suggests this tail consists of material stripped out of the ISM.

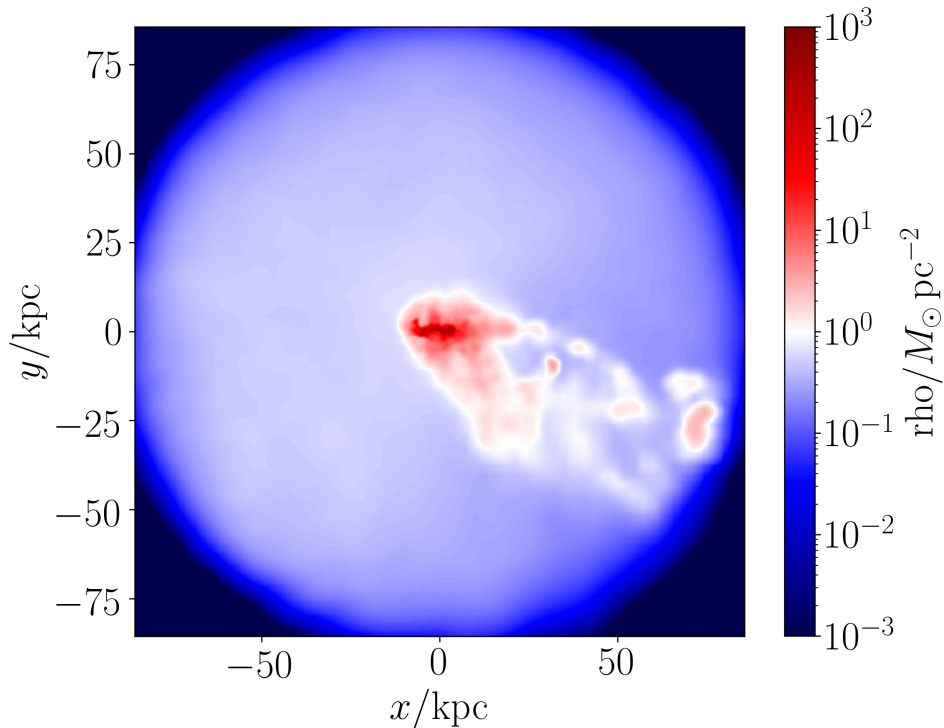


FIGURE 3.2: Gas surface density map for galaxy 648-1286, following the same orientation as the right panel of Figure 3.1. The map is smoothed by some fixed smoothing length and weighted by each particle’s mass and density. The circular background shows the  $R_{\text{vir}}$  cut for halos as discussed in Chapter 2. The surface density was computed via integrating the particles along the  $z$  axis. The most noticeable feature is a large, asymmetrical tail like structure encapsulating the dense ISM in its "head".

In Figure 3.3 we see that the disk and tail are significantly colder than the surrounding medium, which is further evidence that the ISM is stripped out. We also see somewhat smooth gradient-like boundaries between the cool tail and hot

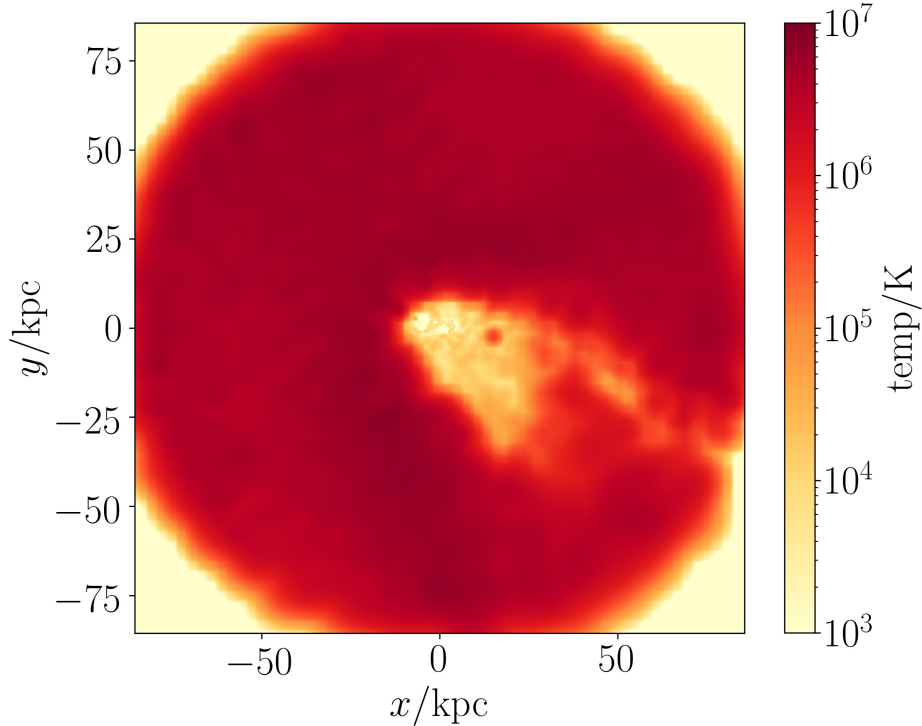


FIGURE 3.3: Temperature map for galaxy 648-1286, taken as a thin slice about the  $z = 0$  plane. It shares the same orientation, image bounds, distinct  $R_{\text{vir}}$  boundary, and mass/density dependent smoothing and weighting as Figure 3.2. The overall morphology is also very similar, although the ISM is not distinctly visible here.

medium, particularly far away from the disk. This suggests the occurrence of mixing processes between hot medium gas and cool tail gas. However, its possible that some of these smooth boundaries are artifacts of blurring in forming the map (we will explore this in more detail in Sections 3.3 and 4.3.3). Another very interesting but hard to see feature of Figure 3.3 is a faint high temperature bow shock in front of the disk and wraps around the galaxy.

Figure 3.4 shows a velocity field. For this galaxy, we see a bulk laminar flow around the galaxy, indicative of the galaxy’s motion through the group medium.

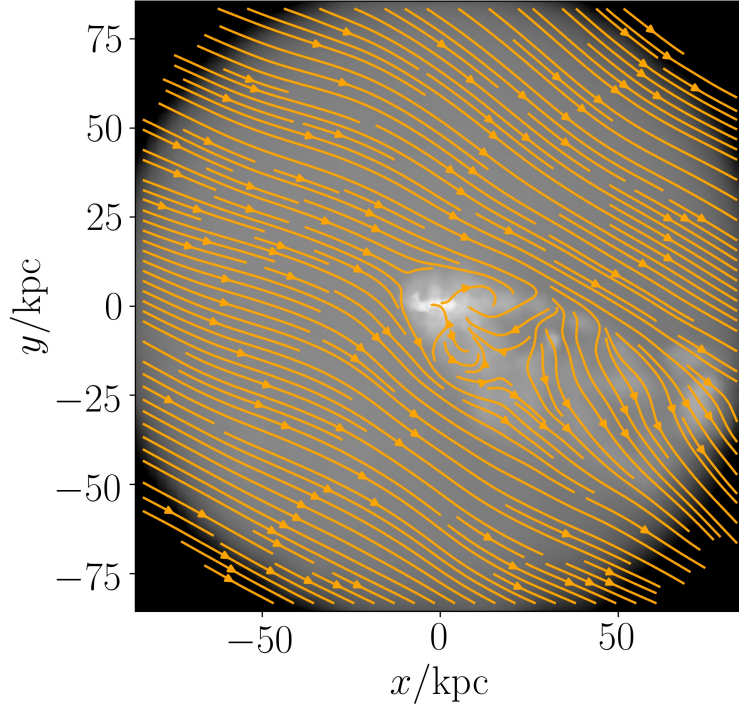


FIGURE 3.4: Velocity field overlaid on top of a gas surface density map for galaxy 648-1286. The magnitude of the arrows do not represent the magnitude of the flow velocities. All velocity field lines are relative to the galaxy’s velocity.

In the wake of the tail we see more turbulent flow and what appears to be vortex-like structures near the disk. We see a laminar boundary flow around the front of the galaxy transitioning into turbulence forming eddies in the wake. The turbulent features of the tail suggest significant velocity offsets between the turbulent tail flow and laminar group medium flow. Additionally, the inwards-pointing velocity field lines forming vortex-like structures could indicate both compression of the ISM and turbulent mixing between the stripping ISM and the hot IGM. These qualitative observations are consistent with isolated wind tunnel simulations of tailed galaxies undergoing ram pressure stripping (Lee et al. 2022, Choi et al.

2022).

In summary, from Figures 3.2, 3.4 and 3.3 we can conclude that these tails are dense, cool, and turbulent, and deduce that these tails are the result of a combination of stripping and mixing processes. Based on these features and properties, we devise a series of particle cuts to isolate the galaxy gas tail.

### **3.3 Tail Characteristics of a Jellyfish Galaxy in Phase Space**

The tail exhibits distinguishable features in density, temperature and velocity space. We can further probe this in phase space using the particle data. Tracking the density, temperature and velocity of each particle we can examine some of their phase diagrams as seen in Figure 3.5.

We see two distinct regions in all phase diagrams - a low density, high velocity and hot population of gas, and a higher density, low velocity and cool population of gas. The region in phase space occupied by the latter population of gas has properties consistent with those observed in the previous section. Additionally, the presence of a smooth "valley"-like transition between the two regions could be indicative of mixing processes.

In this section we seek to quantify the properties of the cool, lower velocity and dense region of gas, based on which we can perform particle cuts to identify the tail particles.

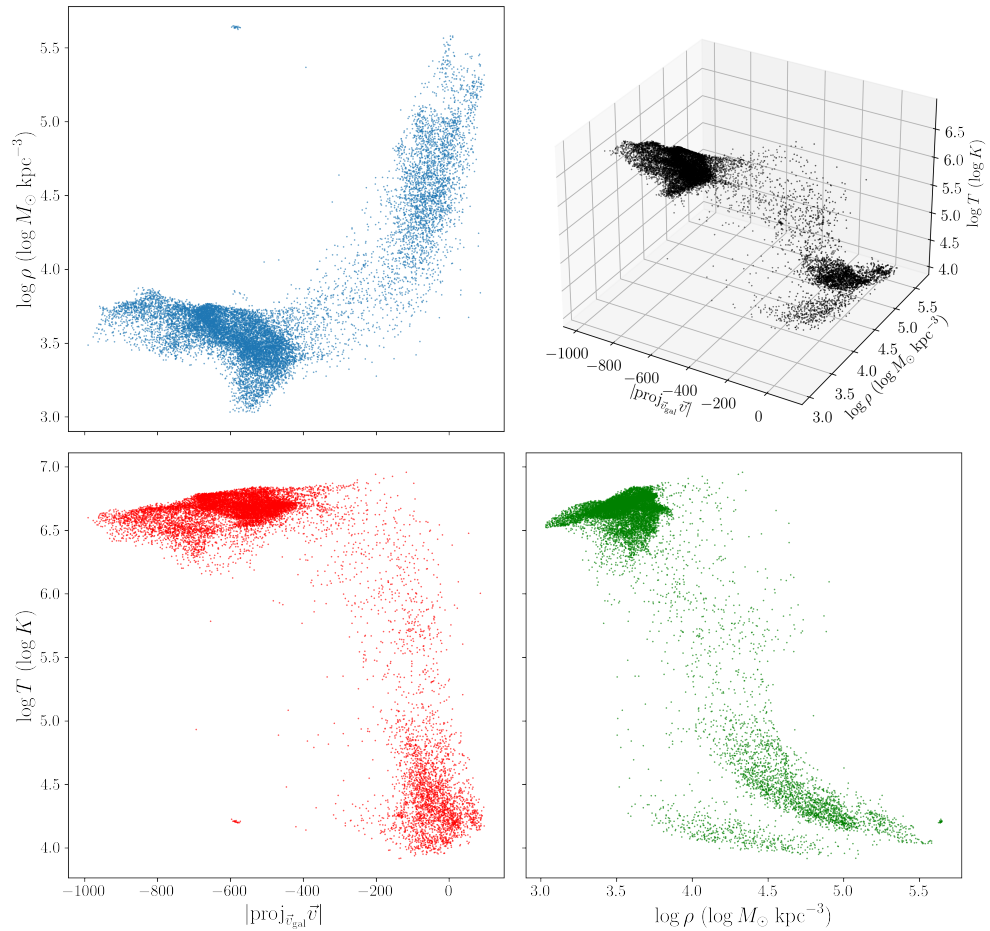


FIGURE 3.5: Density-velocity, temperature-velocity and temperature-density phase diagrams for all particles in the annulus between  $3r_e$  and  $R_{\text{vir}}$  for galaxy 648-1286. A projected 3D phase diagram between all three quantities is shown on the top right.

### **3.3.1 The Background and Direction of Interest**

Before proceeding it is important to define a background and direction of interest. As we've seen from Figure 3.2, the tail visually consists of gas denser than the background. However, to meaningfully quantify this difference, we must define the background. With most of the gas in the galaxy's environment being non-tail gas, the goal is to capture and characterize that background distribution with as little contamination from the tail as possible. These tails, being the product of ram pressure stripping, have a significant preference in their orientation - away from the galaxy's velocity through the medium. Given this preference, we can define the galaxy's velocity vector as the direction of interest, and know that most tails will point away from that.

The background is defined as a truncated cone centered about the velocity vector, with a width of  $60^\circ$  and a inner/outer radial cut of  $6r_e$  and  $R_{\text{vir}}$  respectively, as seen in Figure 3.6. An inner cut of  $6r_e$  was chosen instead of the disk's  $3r_e$  to minimize any interference from the ISM, but our results are not sensitive to this specific choice and any reasonable wider inner cut would suffice.

### **3.3.2 Density Space**

A primary characteristic of these tails appears to be their density. The first and obvious cut to do is a density cut, where we choose particles above a certain density threshold. As we can see in Figure 3.7, the density of the gas particles roughly follows a normal distribution spanning an order of magnitude about  $10^{3.5} M_\odot \text{ kpc}^{-3}$ , but there is also an extended plateau spanning several orders of magnitude at

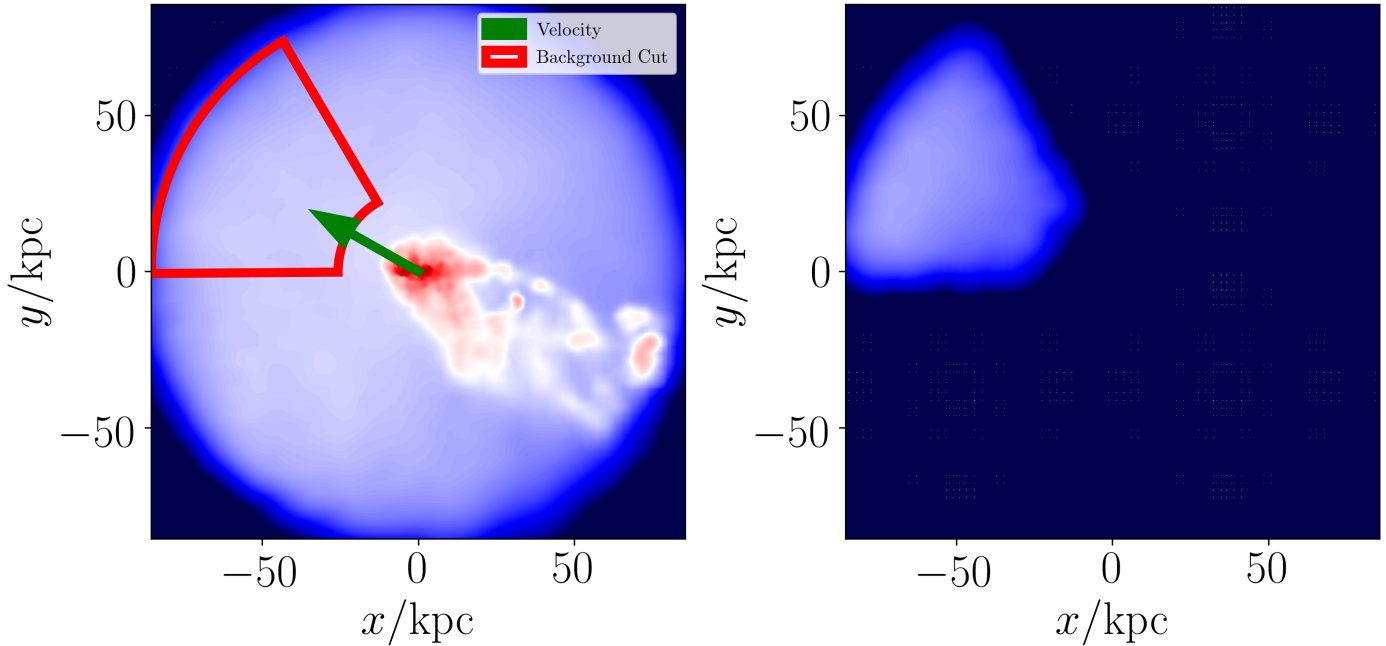


FIGURE 3.6: Visual representation of the background cut, shown on a gas surface density image. The red highlights a slice of the conic cut, and the green arrow shows the galaxy’s projected velocity. The plot on the right shows the result of the cut

higher densities. Contained within the main peak is the normal-looking background distribution, but without the extended plateau. Using this background distribution we can perform a density cut to eliminate the bulk of the low density annulus gas, keeping only the plateau which is associated with the tail, as seen with the red line. We can also see the benefit of defining a background - examining the lime line, had we chosen a cut based on the entire distribution (the entire blue histogram), not only is the distribution not normal, but the plateau also biases the mean towards higher densities, unnecessarily cutting over half the particles associated with the tail.

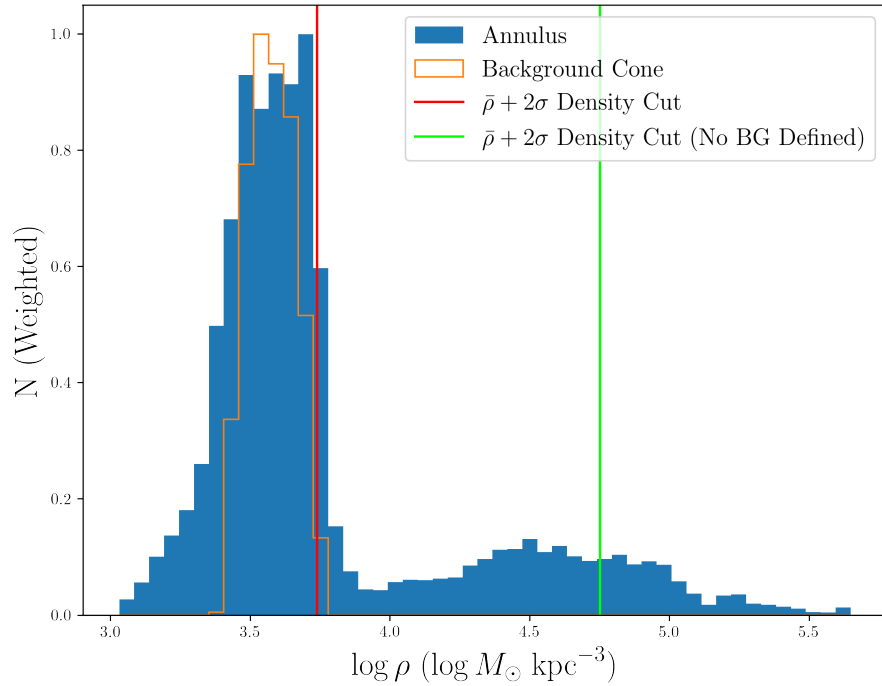


FIGURE 3.7: Distribution of particle densities for galaxy 648-1286. In blue is the distribution of all gas particles within the annulus between  $3r_e$  and  $R_{\text{vir}}$  and in orange is the distribution of background gas particles. The red line shows a  $2\sigma$  density cut based on the background distribution, and the green line shows a  $2\sigma$  density cut based on all gas in the annulus. Both histograms are normalized such that the maximum height of the bins is 1.

It is important to note that dense gas is a visible feature of tails as seen in Figure 3.2, but that does not automatically mean all tail particles are dense. With appropriate additional cuts which we will discuss next, we can lower the threshold of the density cut to include more particles without introducing too many non-tail particles. We explored different density cuts, and settled on the  $2\sigma$  cut as the best discriminator in identifying tails.

### 3.3.3 Temperature Space

Another important characteristic of these tails is their temperature. As we see in Figure 3.3, the tail is much cooler than the disk. This is a relation we expect, given each gas particle has the same mass and that temperature and density share an approximately inverse relationship through hydrostatic equilibrium (assuming isobaric processes). From Figure 3.8 we can see two very distinct populations of cold and hot gas peaking at around  $10^{4.5}$  K and  $10^{6.7}$  K. The cool peak is also close to but distinctly offset from the temperature distribution of the disk gas, which peaks at around  $10^4$  K, which is further suggestive of heating of stripped ISM gas through mixing with group medium gas. We observe a valley from  $10^5$ - $10^6$  K where almost no particles reside. Based on the  $2\sigma$  gas (in orange) and disk gas (in green) temperature distributions, we see that the cool gas in the annulus traces the tail gas quite well.

Interestingly, if we examine Figure 3.9, where we plot the combined distributions of all galaxies in our sample (with weighting, as discussed in Section 2.5.3, applied to each galaxy), we see almost the exact same trends at very similar temperatures. We observe again two distinct peaks, a  $10^5$  K valley, and the disk gas distribution's proximity to the cool peak, all with very similar values to those of Figure 3.8. The effects of superbubble feedback (Keller et al. 2014) can be seen in the small high temperature spike of disk gas at around  $10^7$  K. Our observations of very similar trends between the two figures suggest that this cool gas tracing of tail gas is a universal feature of all galaxies in our sample.

As mentioned earlier, introducing a direct temperature cut alongside a direct density cut would be somewhat redundant given their direct inverse relationship.

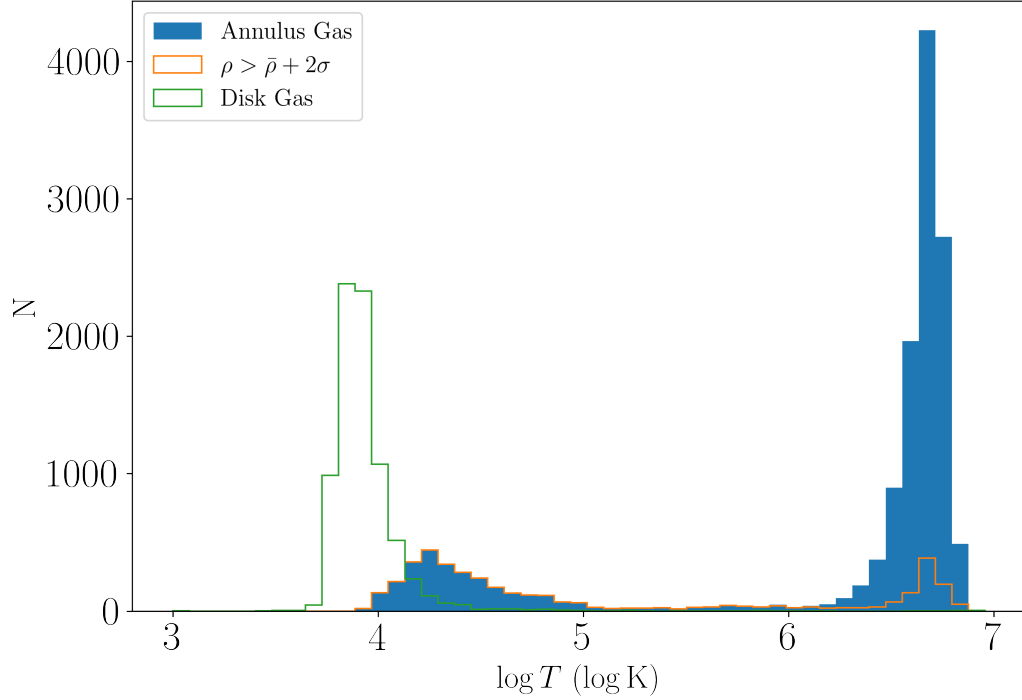


FIGURE 3.8: Distribution of gas particle temperatures for galaxy 648-1286. In blue is the distribution of all gas particles within the annulus between  $3r_e$  and  $R_{\text{vir}}$  and in orange is the distribution of gas particles with a density  $2\sigma$  above the mean density. In green is the distribution of gas in the disk ( $r < 3r_e$ )

However, as we will discuss in the next section, we use the cool gas distribution to greatly simplify our velocity-space computations. In this study, we chose gas in the annulus below  $10^{5.5}$  K as our cool gas distribution.

### 3.3.4 Velocity Space

The turbulence in the tail from Figure 3.4 is suggestive of a large velocity offset between the turbulent flow in the wake of the tail and the bulk laminar flow of the group medium. However, with the flow becoming laminar further along the tail,

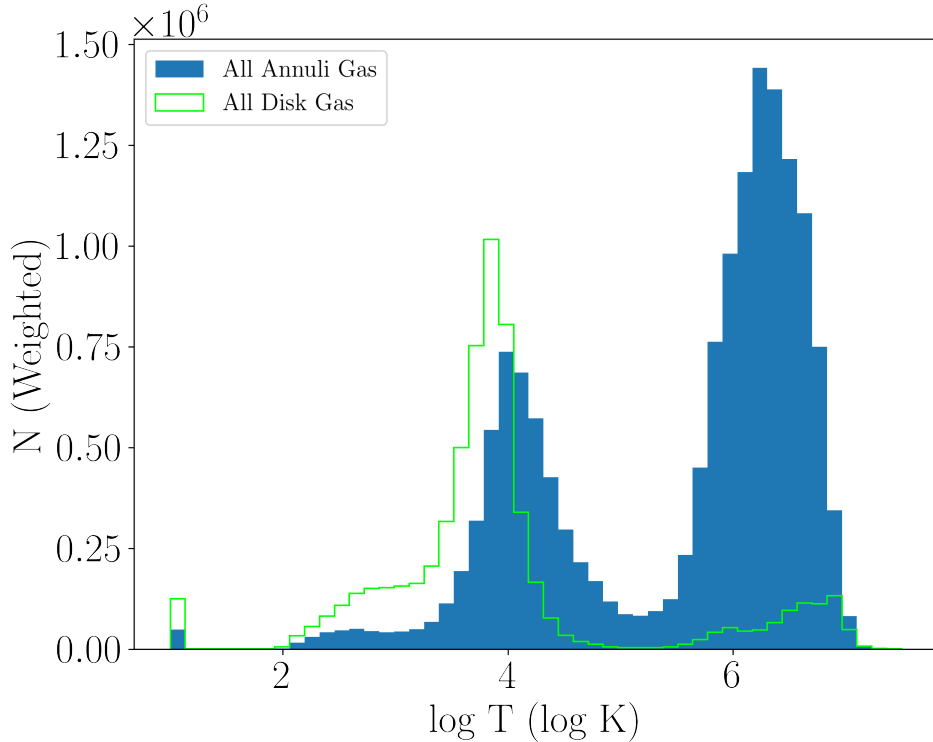


FIGURE 3.9: Distribution of gas particle temperatures for all sampled galaxies (see Chapter 2) across all snapshots. Each galaxy’s particles are weighted using the scheme described in Chapter 2. In blue is all the gas particles in all the annuli and in lime is all the gas particles in all the disks.

it is not immediately obvious whether or not the velocity offset is only present for stripped ISM near the disk or for the entire tail. Since ram pressure is the dominant force stripping the disk, we can perform a rough calculation to estimate the expected velocity and positional offsets for particles in the ISM.

We can approximate an equation of motion for a gas particle in the disk. We enter the rotating frame of the galaxy with the same angular frequency as some bound particle such that it is at rest. We approximate the ram pressure as some

force applied to the particle, which translates to an acceleration. We ignore centrifugal and coriolis effects for simplicity. In Chapter 2 we derived an acceleration due to ram pressure when defining a modified stripping criterion. We borrow this term to define the equation of motion:

$$\ddot{r} = a_{\text{ram}} \quad (3.1)$$

$$= \frac{\rho v^2}{\Sigma_{\text{gas}}} \quad (3.2)$$

Here we take  $\Sigma_{\text{gas}}$  as the average surface density of the entire disk, since this is difficult to define for individual particles. We assume constant acceleration across a single timestep  $\Delta t$  such that the shift in velocity and position can be expressed as

$$\Delta v = \ddot{r} \Delta t \quad (3.3)$$

$$\Delta r = \Delta v \Delta t + \frac{1}{2} \ddot{r} \Delta t^2 \quad (3.4)$$

Examining the relative magnitudes of these values in Table 3.1, we notice that they are relatively small, with velocity shifts on the order of 1 - 10 km/s and positional shifts of order 1 kpc. These calculations are very rough and likely only accurate to within an order of magnitude, but they demonstrate that stripped gas will show minimal shifts in velocity and position within single timesteps.

Examining the velocity histogram in Figure 3.10, as with earlier figures we see two distinct populations of gas. In one population we see the particle velocities distributed slightly off-center of zero, while in the other population we see particles with very negative velocities offset by more than typical galaxy velocity dispersions.

Galaxy	$M_{\text{star}}$ ( $\log M_{\odot}$ )	$3r_e$ (kpc)	$\Delta v$ (km/s)	$\Delta r$ (kpc)
936-4690	9.229	5.886	18.09	0.9948
960-4637	9.24	5.961	15.81	0.8694
688-3253	8.835	6.501	7.447	0.4096
872-6518	9.194	5.501	1.332	0.07328
848-4632	8.63	5.19	1.17	0.06436
896-7144	9.212	5.639	2.765	0.1521
648-11540	8.51	5.702	123.7	6.806
568-5059	8.589	3.765	35.85	1.972
1024-4392	9.43	6.827	0.6056	0.03331
632-4890	8.508	5.714	80.3	4.417
952-7024	9.235	5.945	17.83	0.9807
840-7294	9.177	5.329	1.233	0.06783
888-5124	9.203	5.622	1.416	0.0779
624-3146	8.819	5.353	1.34	0.07369
928-3429	9.225	5.794	13.98	0.769
904-1418	9.215	5.641	4.73	0.2602
912-8675	9.216	5.704	8.686	0.4778

TABLE 3.1: Table of galaxies and the expected velocity/position shifts for their ISM over a single timestep (107.64 Myr) due to ram pressure. The columns from left to right represent: galaxy ID, stellar mass,  $3r_e$  disk radii, velocity shift and positional shift (as calculated using Equation 3.1). It is important to note that this is a highly simplified calculation, and these values should be taken as their order of magnitude.

Examining the distributions with temperature and density cuts applied, we see that most of the high velocity gas is hot and of low density.

Unlike earlier, implementing appropriate cuts in velocity space is more challenging, and requires characterization and fitting of the velocity distribution. The velocity offsets of both the stripped gas and background gas are heavily dependent on the galaxy’s environment and its own velocity through the group medium. It would not be practical to define a universal separation line as we did with temperature, thus velocity cuts would need to be calculated separately for each galaxy.

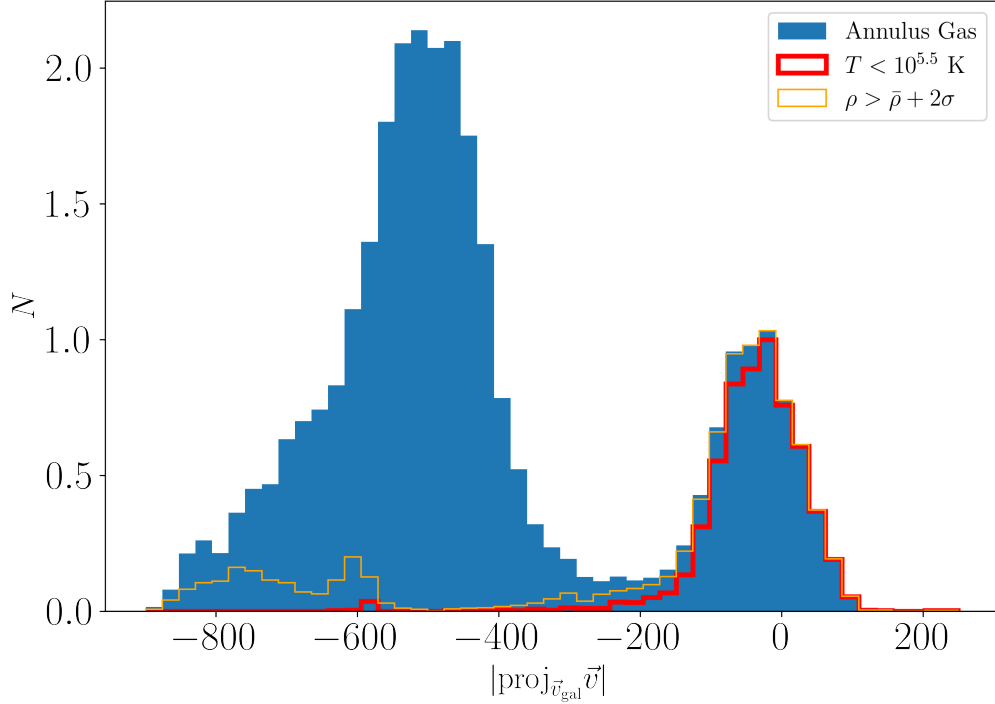


FIGURE 3.10: Distribution of projected velocities within the CGM for galaxy 648-1286, alongside distributions following a density and temperature cut. Each particle’s velocity (relative to the galaxy) is projected onto the velocity vector of the galaxy, the magnitude of which is plotted. Each histogram shares the same normalization

Separating the two distributions and cutting them would require a bimodal fit. This is where we return to the universal temperature cut from earlier. Unlike velocity, a  $10^{5.5}$  K valley is universal among nearly all galaxies. Implementing both direct density and temperature cuts is redundant, but in this case we use temperature not as an explicit cut, but as a constraint in parameter space while curve fitting monomodal distribution in velocity space. We can see from the red histogram in Figure 3.10 that isolating the cooler gas reduces the bimodal distribution down to a monomodal distribution.

The benefit of a monomodal fit over a bimodal fit is the decreased number of parameters that need to be fit. A bimodal gaussian fit requires seven parameters: each distribution’s amplitudes  $A_1, A_2$ , means  $x_1, x_2$  and standard deviations  $\sigma_1, \sigma_2$ , and the  $y$  offset  $C$ . Proper least-squares curve fitting requires well constrained bounds and initial guesses for all these parameters. While the bounds and guesses for the cool, stripped gas can be constrained using the properties of the disk, those of the hot group medium gas are much more difficult to constrain. A monomodal gaussian fit on the cool stripped gas reduces the number of required parameters

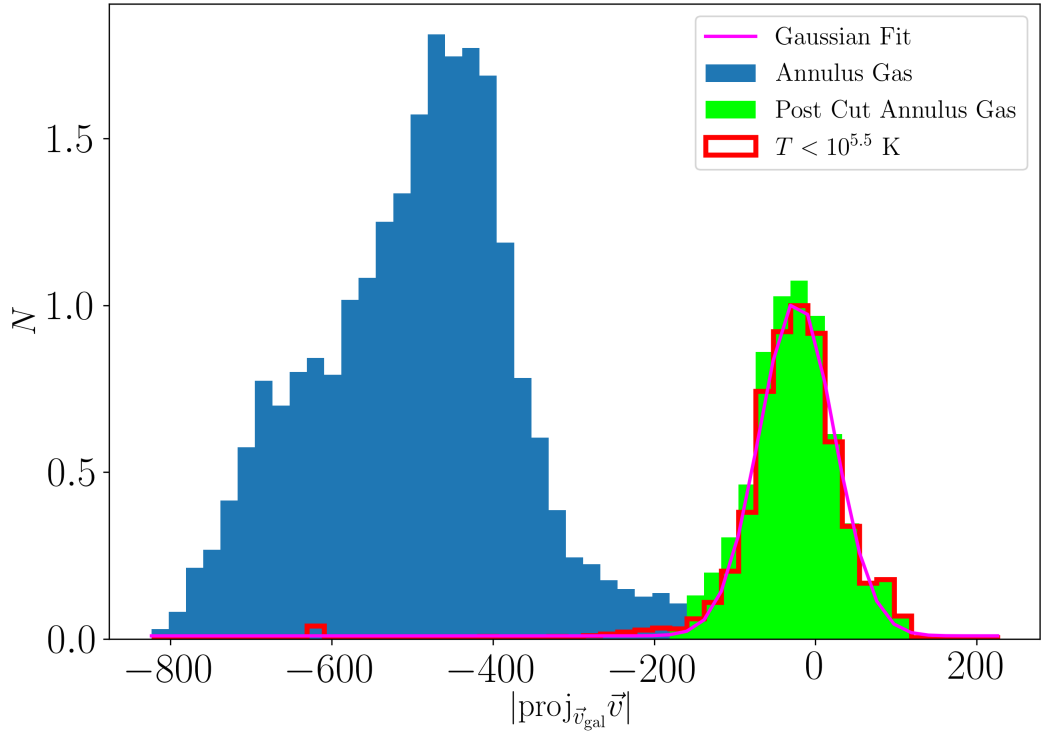


FIGURE 3.11: Same velocity distribution as Figure 3.10. The magenta gaussian curve fit is based on the velocity distribution of the cool  $T < 10^{5.5}$  K gas, and the lime distribution represents a two-ended  $3\sigma$  cut of the fitted gaussian on the entire distribution. As with Figure 3.10, each histogram shares the same normalization

down to four and greatly reduces the amount of parameter space exploring required for fitting.

We define our velocity cut as follows: we fit a gaussian onto the velocity distribution of the cool gas, perform a  $3\sigma$  velocity cut on both ends, and apply that velocity cut onto the total velocity distribution. Figure 3.11 shows the results for galaxy 648-1286, where we see not only a clean curve fit and cut, but also the capture of additional particles (where the lime peeks out from the red) that would have been missed with a pure temperature cut.

## 3.4 Putting It All Together

### 3.4.1 The Tailfinding Algorithm

Below is our succinctly summarized tailfinding algorithm. We will reference Figure 3.12 for visualization purposes.

- Cut out the ISM (all particles within  $3r_e$ ) and use the galaxy’s velocity vector to compute the background density distribution.
- For the remaining CGM (annulus of gas between  $3r_e$  and  $R_{\text{vir}}$ ), isolate the cool particles with  $T < 10^{5.5}$  K (red particles in the bottom left plot of Figure 3.12 below the green dotted line), and fit a gaussian curve to the projected velocity distribution of particles.
- Define  $3\sigma$  projected velocity cuts on both sides of the mean (dashed, dark red lines in both the bottom left and top left plots of Figure 3.12), and then perform this cut on the projected velocity distribution of the entire annulus

- Finally, perform a  $2\sigma$  density cut (dashed, black line on the top left and bottom right plots of Figure 3.12) on the remaining particles based on the background distribution.

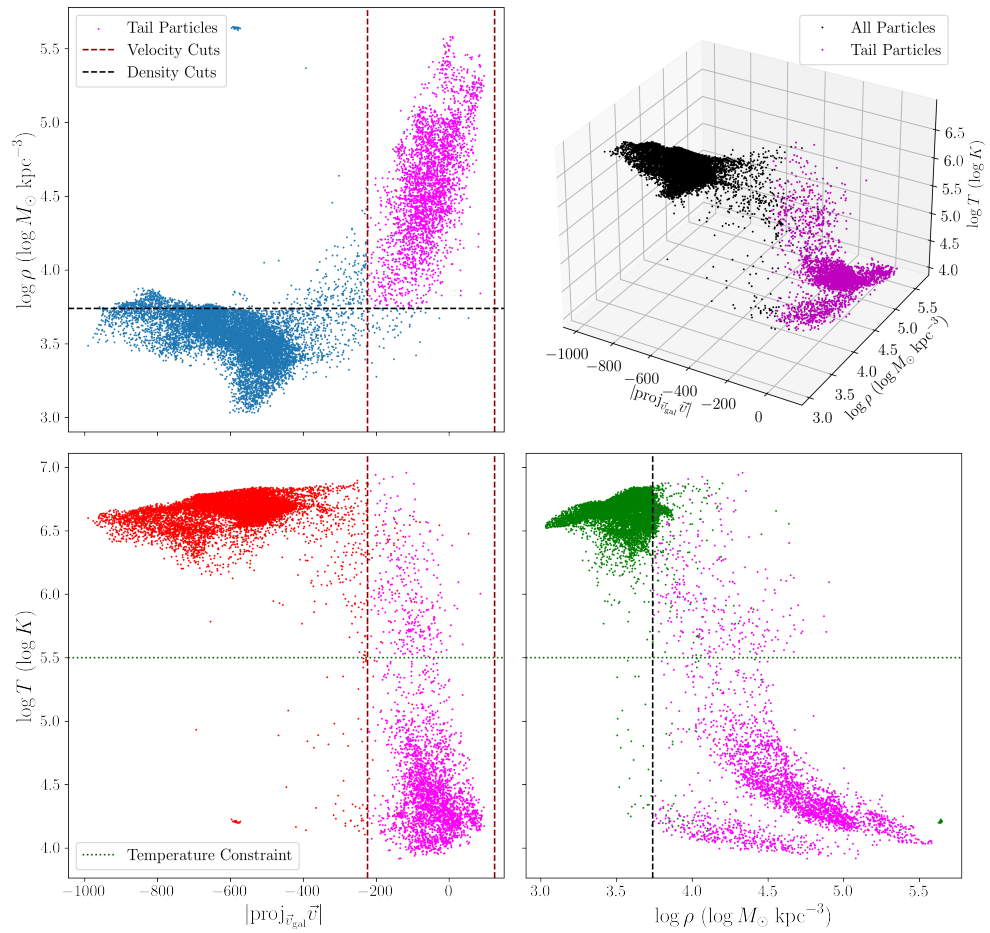


FIGURE 3.12: The same density-velocity, temperature-velocity, temperature-density and density-temperature-velocity phase diagrams from Figure 3.5, except with the cuts shown. The brown and black dashed lines represent the density and velocity cuts, while the dark green dotted line represents the temperature constraint which helped define the velocity cuts. The result of the algorithm is shown in all panels with tail particles shown in magenta.

### 3.4.2 Result

In all phase diagrams in Figure 3.12, our series of cuts is successfully able to isolate the population of interest, as seen in the rectangular areas captured by the dashed line cuts. The magenta particles show the result of our cuts - to interpret the bottom two plots (temperature-velocity and temperature-density), it's important to remember that the dotted green line is not a direct cut but a constraint for the velocity cuts, and effectively they only show one direct cut each. Overall, we can see that we're successfully able to capture not only the cool, dense and slow gas population, but also some gas particles transitioning/mixing towards that gas

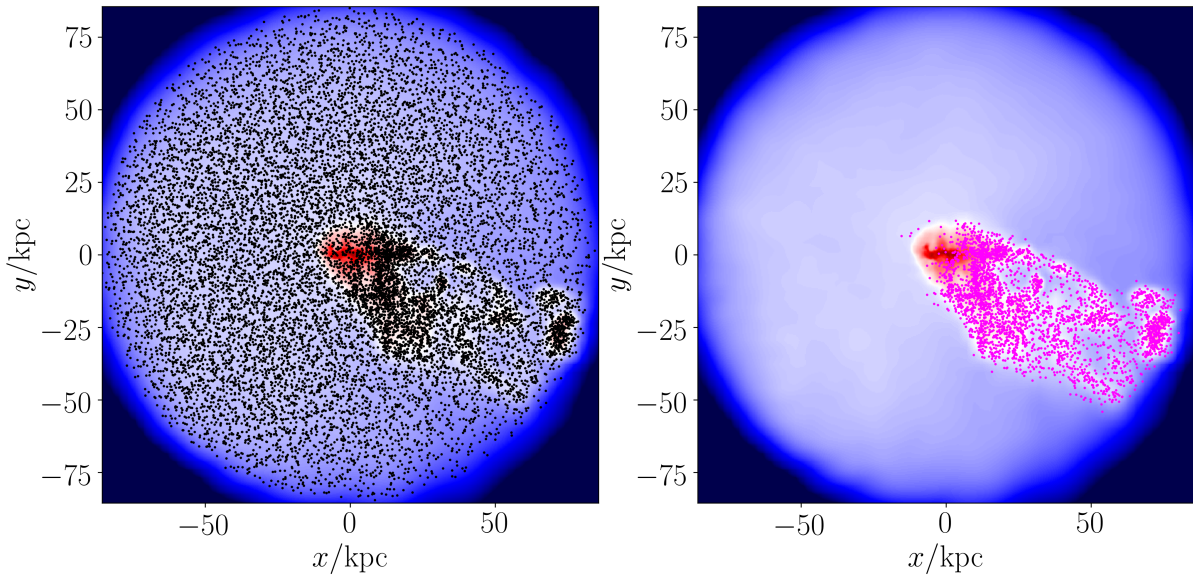


FIGURE 3.13: Gas density maps of galaxy 648-1286, with tail particle positions plotted on top. The left plot shows all gas particles in the annulus in black, and the right plot shows the tail particles in pink. It's important to note that only x and y positions are shown, so particles that appear to be inside the disk are actually either above or below the  $3r_e$  sphere in  $z$

population. The addition of the velocity cut also allows us to capture more of these transitioning particles with a lowered density cut without unnecessarily capturing the hot group medium gas, as seen in the top left and bottom right plots where hot, low density particles peek beyond the density cut but are not counted in our tail due to not satisfying the velocity cuts. In Figure 3.13 we can also see that the tail particles picked out by our algorithm trace the observed stripped tail very well.

### 3.4.3 The Necessity of Multiple Cuts

Figures 3.13 and 3.12 might raise the question on the necessity of both a velocity and density cut. While usage of both cuts allows us to probe lower density thresholds as mentioned above, it may not seem wholly necessary. Specifically for galaxy 648-1286, we can achieve a very similar result with a single density cut at a slightly higher threshold.

To illustrate the necessity of both cuts, we turn to a different tailed galaxy - galaxy 608-108, as shown in Figure 3.14. Like with Figure 3.2, this galaxy also exhibits a clear tail. However, there is high density structure within the halo. If we apply a direct density cut on this galaxy, as seen in Figure 3.15, we end up capturing this structure (as well as a large amount of "fluff" in front of the galaxy in the  $2\sigma$  case). Particles within this structure remain captured with higher density thresholds up to  $4\sigma$ , and while even higher thresholds may entirely eliminate the extraneous particles, it would unnecessarily cull particles in the tail itself.

If we apply all the cuts as seen in Figure 3.17, we are able to successfully cut out this non-tail structure and even some of the extra fluff in front of the galaxy

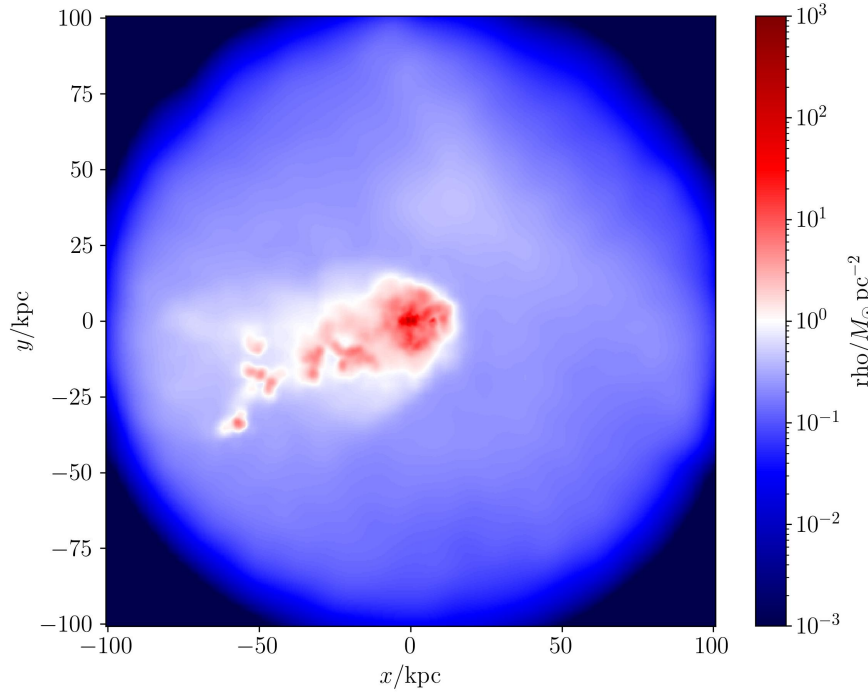


FIGURE 3.14: Gas surface density map for galaxy 608-108. As with Figure 3.2, the map is smoothed by some fixed smoothing length and weighted by each sph particle's mass and density. The circular background shows the  $R_{\text{vir}}$  cut for halos as discussed in Chapter 2. The surface density was computed via integrating the particles along the  $z$  axis. The most noticeable features are a large, asymmetrical tail like structure encapsulating the dense ISM in its "head", and a higher density "strip" cutting through the halo like a chord.

while maintaining a low  $2\sigma$  density cut. Examining Figure 3.16, we can identify this structure as some clump of hot gas with a high velocity offset, meaning it is likely something the galaxy is flying by and it is not associated or bound to the galaxy. We can see in the bottom left how the introduction of velocity cuts helps eliminate that structure from our tail. For this particular galaxy, it is important to note that the background density for this galaxy is quite low, resulting in the

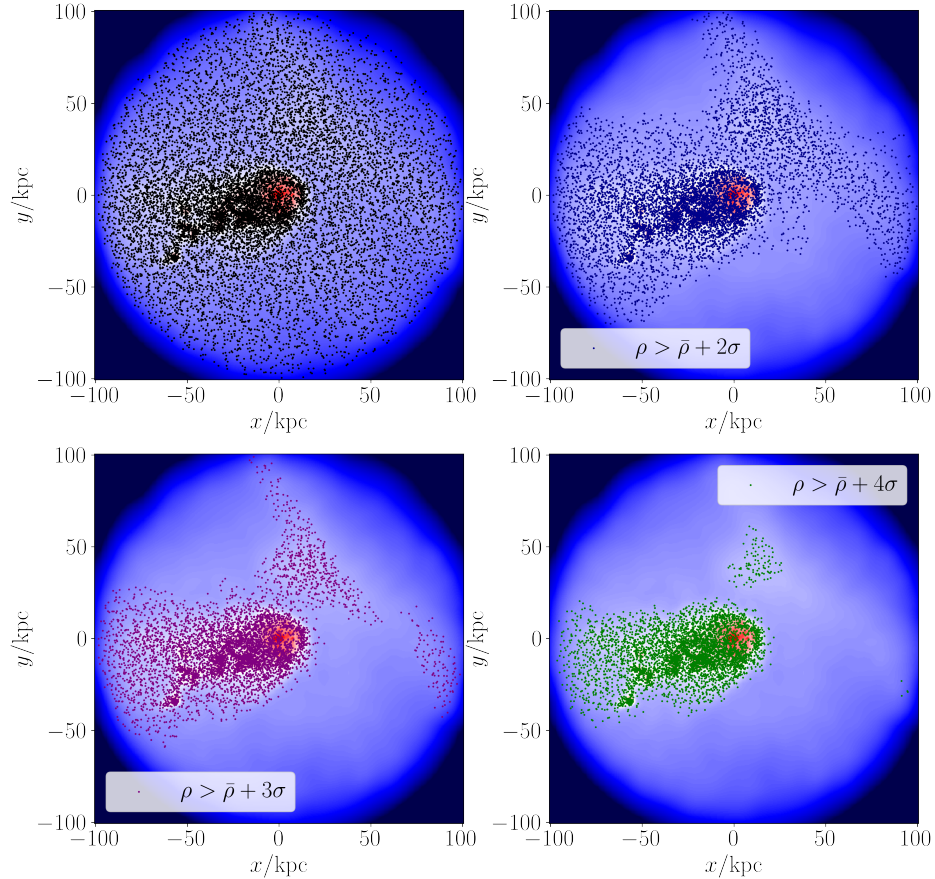


FIGURE 3.15: Gas density maps of galaxy 608-108, with dense particle positions scattered on top. The top left plot shows all gas particles in the annulus, and the top right, bottom left and bottom right plots show the  $2\sigma$ ,  $3\sigma$ , and  $4\sigma$  particles respectively. As with Figure 3.13, it's important to note that only x and y positions are shown, so particles that appear to be inside the disk are actually inside the  $3r_e$  sphere in z

capture of some hot gas, as evident in the hot magenta particles in the bottom plots and the density cut including some gas from the low density population in the top-left plot of Figure 3.16.

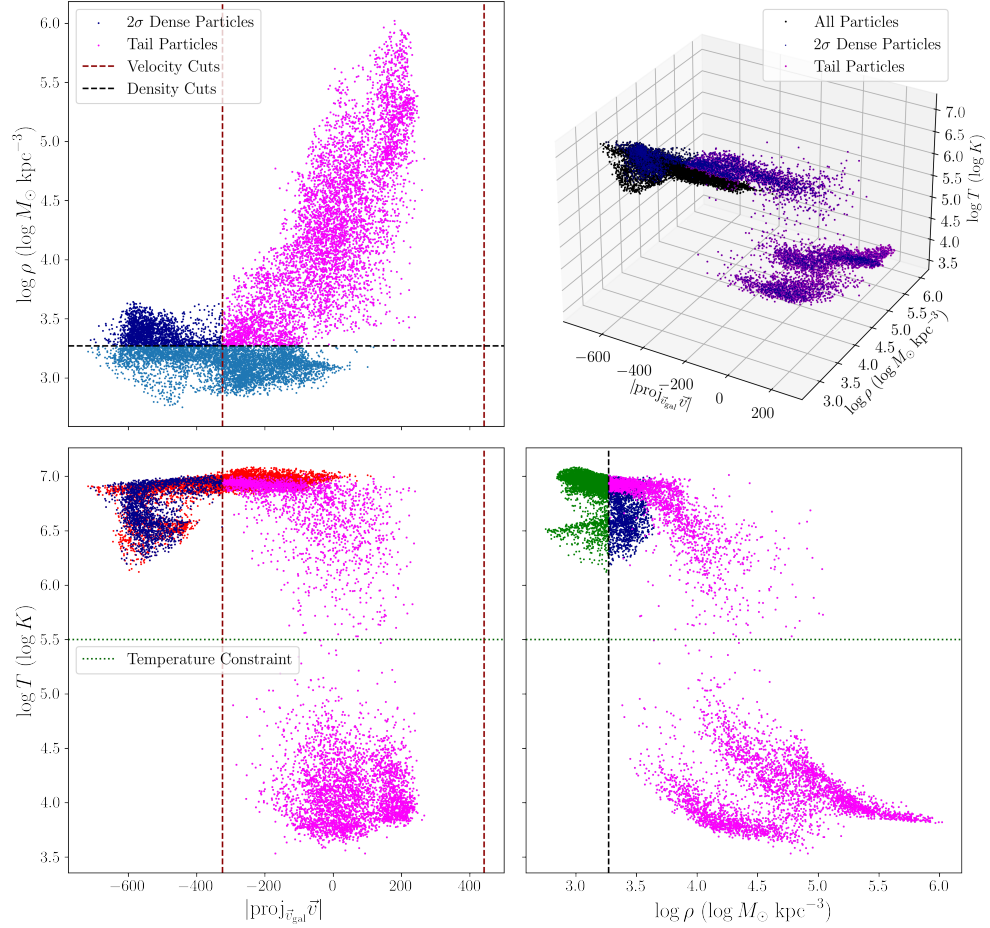


FIGURE 3.16: The same density-velocity, temperature-velocity, temperature-density and density-temperature-velocity phase diagrams from Figure 3.12, but for galaxy 608-108. The brown and black dashed lines represent the density and velocity cuts, while the dark green dotted line represents the temperature constraint which helped define the velocity cuts. The result of the algorithm is shown in all panels with tail particles shown in magenta. Additionally, the results of a pure  $2\sigma$  density cut are shown in dark blue dots.

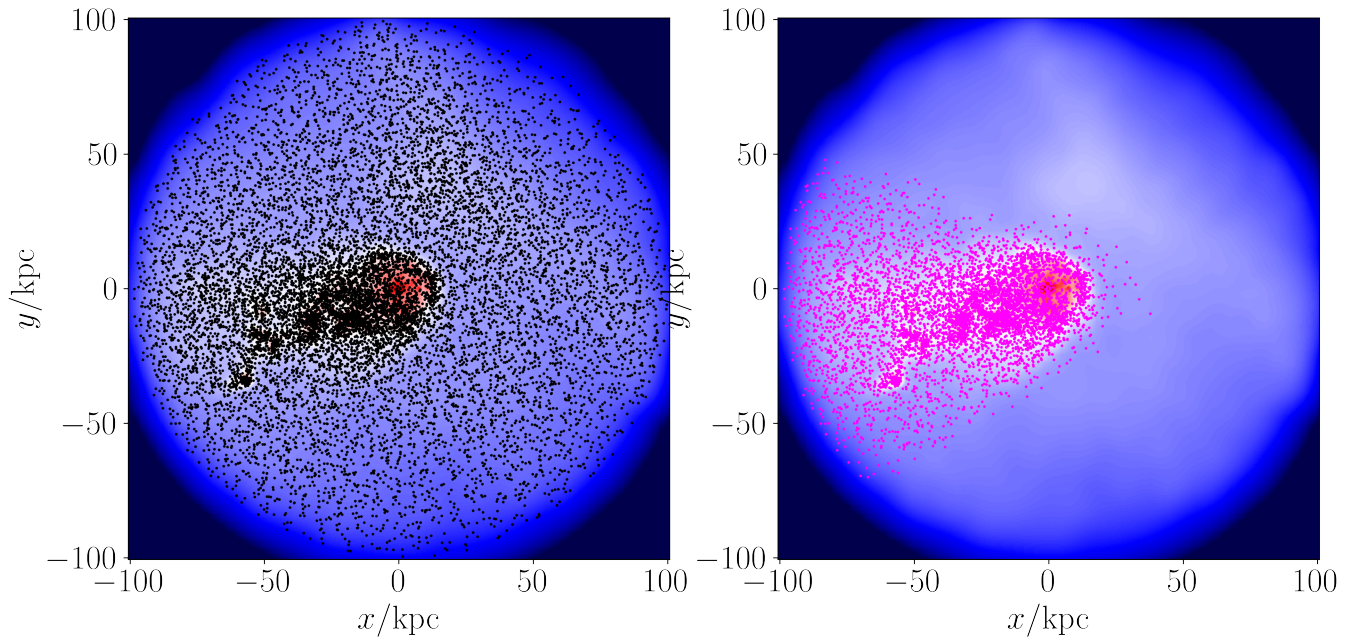


FIGURE 3.17: Gas density maps of galaxy 608-108, with tail particle positions scattered on top. The left plot shows all gas particles in the annulus, and the right plot shows the tail particles. As with Figure 3.13, it’s important to note that only x and y positions are shown, so particles that appear to be inside the disk are actually either above or below the  $3r_e$  sphere in z

To summarize the justifications for our cuts:

- The density cut captures the most visually identifiable feature of these tails in form of a dense, cool ISM getting stripped out of a galaxy. This cut eliminates most of the low density background.
- The temperature constraint reduces the the amount of parameter space exploration needed for velocity distribution curve fitting by transforming a

bimodal distribution to a unimodal distribution. The physical basis on using the cool gas is again based on observations that the ISM and stripped tail are cooler than the background.

- The velocity cut captures the turbulence of the tail and represents a general "association" requirement where the tail should only have a small velocity offset from the galaxy and still be associated with the galaxy. This cut eliminates dense unbound structures that happen to be passing by the galaxy in a given snapshot.

We explore some additional justifications and fine tuning in Appendix [A](#).

### **3.5 Limitations**

The tailfinding algorithm is based on a series of assumptions outlined in this chapter. Galaxy 648-1286 was one among many galaxies we visually surveyed and we believe these assumptions to be well motivated. However, in our assumptions of a dense, cool and slow (relative to the disk) moving tails there are a few critical limitations

- The mean density of the IGM increases the closer a galaxy gets to the group center, increasing significantly within a virial radius. The higher background density results in a higher threshold for a density cut, lowering the number of true tail particles that survive the cuts. Additionally, as the galaxy approaches its pericentre passage well within the virial radius, the velocity of group medium particles relative to the BGG increases, meaning the velocity of these particles in the frame of the galaxy decreases. This results in the

velocity cut unintentionally capturing hot group gas. To address this, we set  $10^{5.5}$  K as a rigid temperature cut for galaxies within 0.75 virial radii of the group. While this would inevitably cull the galaxy's "true tail", we deemed this to be a simple but effective fix to the larger problem. We were not able to adequately address the issue of increasing background density on pericenter approach.

- The tailfinding algorithm presupposes that tails are a product of ram pressure stripping, where we expect to see the properties outline in this chapter. However, ram pressure stripping is not necessarily the only mechanism for creating asymmetrical tail-like structures, and one such mechanism we observed is tidal stripping between merging galaxies. Tidal stripping can be a significantly more violent process and we would expect much more background contamination from the neighbouring galaxy's CGM. Additionally, tails produced by tidal stripping may have vastly different properties than tails produced by ram pressure stripping. We addressed this by removing any galaxy undergoing major mergers in our sample (more discussion in Chapter 4), focusing our analysis on galaxies with ram pressure stripped tails
- As galaxies become increasingly gas depleted, the extent of the ISM and tail shrink inwards towards the galaxy center. Meanwhile, the stability of the stellar mass distribution of the disk maintains  $3r_e$  at a relatively static value over time. For some galaxies well within the virial radius, their tails lie well within  $3r_e$ , which unfortunately means they are undetectable. We did not adequately explore solutions to this problem, but one possible prescription is an algorithmic truncation of the  $3r_e$  cut based on the morphology and mass

of the remaining ISM for galaxies within the virial radius.

- Not all galaxies exhibit a tail, but we did not have a prescription to account for non-tailed galaxies (though we did explore methods such as studying angular gas distributions). Figure 3.18 shows an example of a galaxy in our sample, which despite the presence of asymmetries, does not exhibit any significant tail-like asymmetries and has a relatively uniform angular distribution of gas. Applying the tailfinding algorithm gives us particles, but these particles have no physical interpretation beyond being dense and having their velocities fall within some range.

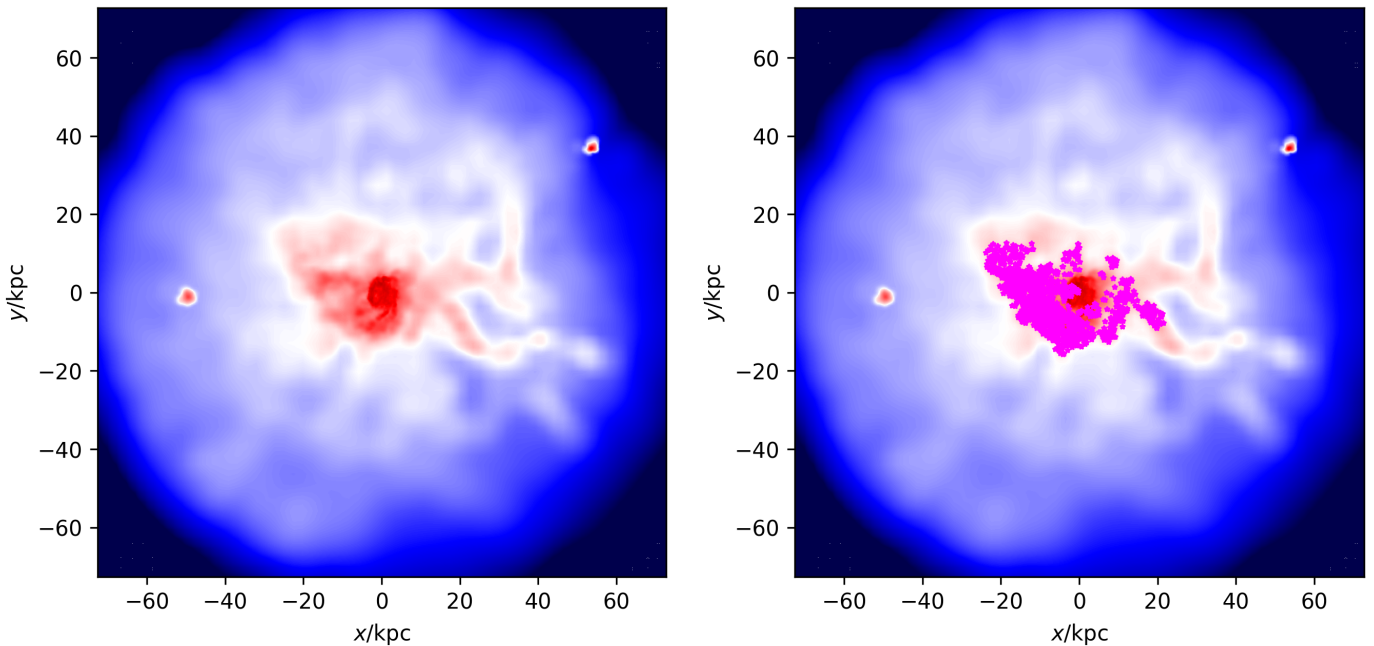


FIGURE 3.18: The gas density map of galaxy 568-5023 on the left, with the particles identified by the tailfinding algorithm overlaid on the right. 568-5023 is an ancestor of infalling galaxy 648-1286, and is many virial radii away from the group at the time this gas density image is taken at.

# Chapter 4

## Results

### 4.1 Statistical Galaxy Tail Correlations

In this section we examine our sample of galaxies as a whole. We explore distributions in tail orientations and possible correlations between tail properties and their host galaxy properties

#### 4.1.1 Galaxy Classifications

We classify our galaxies into four distinct categories: infalling galaxies, backsplashing galaxies, merging/post-merging galaxies and far away galaxies (see Table 4.1 for definitions). Infalling galaxies are chosen to be objects falling into the group within 2 virial radii; backsplashing galaxies are chosen to be objects moving away from the group center within 2 virial radii; mergers are defined as objects that will undergo, or have undergone a major merger with a mass ratio greater than 0.3 within the past or future 535 Myr (major merger within 1.07 Gyr time window);

Category	Definition	Count
Infaller	$\vec{v}_{\text{gal}} \cdot \vec{r} < 0, d < 2R_{\text{vir}}$	307
Backsplasher	$\vec{v}_{\text{gal}} \cdot \vec{r} > 0, d < 2R_{\text{vir}}$	236
Merger	$M_{\text{gal}}/M_{\text{merger}} > 0.3,  t - t_{\text{merge}}  < 535 \text{ Myr}$	1058
Far Away	$d > 2R_{\text{vir}}$	2947

TABLE 4.1: Our sample selection table. Here  $R_{\text{vir}}$  refers to the virial radius of the group.

far away galaxies are chosen to be objects outside 2 virial radii. Infallers, back-splashers and far away objects are categorically distinct classes, while mergers may comprise of objects at all distances and velocity directions. 2 virial radii is chosen as a radial cut to distinguish galaxies that are likely to experience significant ram pressure near the group. Each class is distinct - no galaxy appears in more than a single class.

For the purposes of tail specific characteristics we ignore the mergers and far away galaxies. We eliminate mergers since they are more likely to exhibit tails produced by non-ram pressure mechanisms such as tidal stripping. Through visual inspection of many gas density maps, and the physical justification that ram pressure is weak for far away objects (a trait visible in Figure 4.8, where galaxies see their ram pressure increase by several orders of magnitude as they fall into the group), we eliminate the far away galaxies. Additionally, as we saw with Figure 3.18, there are galaxies in our sample that do not exhibit clear tails. Culling the pre/post merging and far away galaxies, on top of the reasons above, is also a prescription for removing as many of the non-tail galaxies as possible.

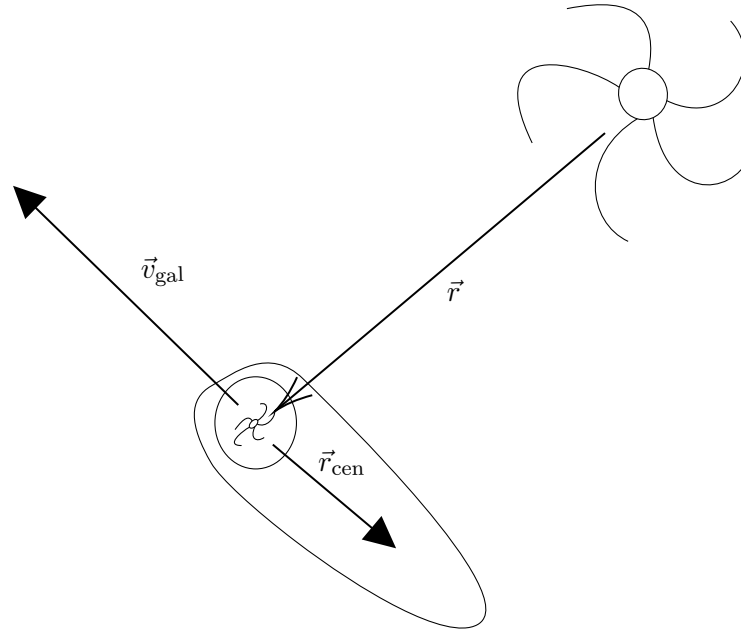


FIGURE 4.1: A diagram illustrating the three vectors of interest. The large galaxy represents the BGG, the smaller galaxy our galaxy of interest, the circle around it the  $3r_e$  disk cut, and the extended blob the tail.

### 4.1.2 Tail Orientation

We examine the orientation of these tails. Each galaxy has three vectors of interest as shown in Figure 4.1. The radial vector  $\vec{r}$  represents the galaxy’s position relative to the central BGG, the velocity vector  $\vec{v}_{\text{gal}}$  the galaxy’s velocity relative to the group, and the tail centroid vector  $\vec{r}_{\text{cen}}$  the center of mass of the tail relative to the galaxy’s position.

In Figure 4.2 we can examine the correlations between the positions, velocities and tail centroids of all galaxies in our sample. The position-velocity column tells us that most galaxies are falling towards the BGG. This is expected given our sample selection and the properties of our simulation - our galaxies are objects

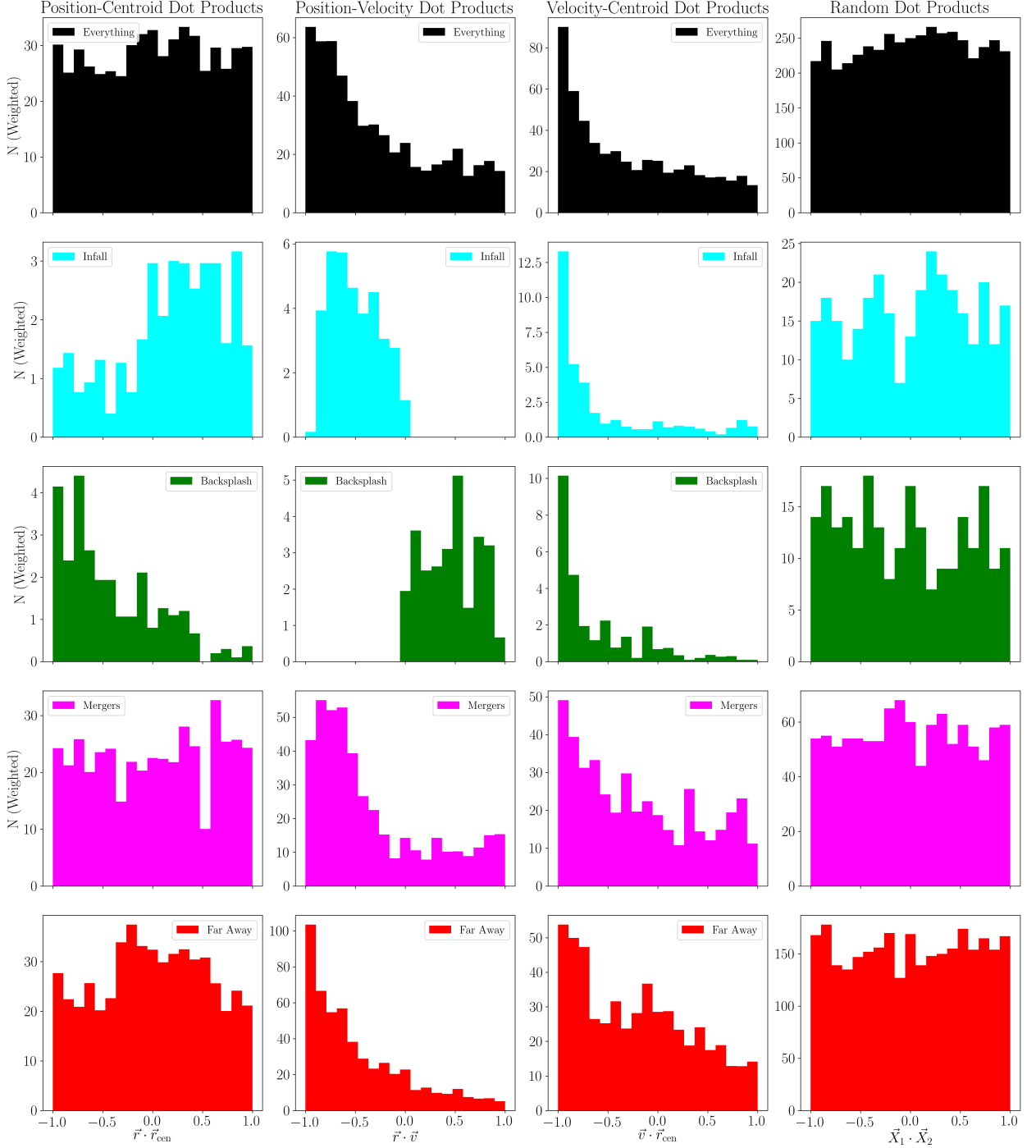


FIGURE 4.2: Dot products between the position, tail centroid and velocity vectors. All vectors are normalized so their dot products range from -1 to 1. A histogram of random dot products, with random vectors chosen from a uniform spherical distribution, is shown on the rightmost column as a control. A value of 1 represents perfect alignment, while a value of -1 represents perfect anti-alignment.

that are part of a group at  $z = 0$ , and since we are using galaxies across multiple snapshots, we can expect many galaxies back in time to be falling in towards the BGG. For the infalling and backsplashing galaxies we notice the peak shift away from the extrema, which is expected for galaxies in keplerian orbits near their pericenter.

Examining the velocity-tail centroid column next we see spikes at -1 for all classes, with the spike being especially sharp among infalling and backsplashing galaxies. Physically this represents strong anti-alignment between the galaxy's velocity and tail orientation, and is consistent with the findings of Yun et al. 2019 in the IllustrisTNG galaxies. There are a larger number of mergers and far away galaxies with higher dot products values compared to the infallers and backsplashers, representing a more even spread of tail directions relative to velocity. This could indicate the presence of non tailed galaxies as seen in Figure 3.18 or stripping/tail forming mechanisms alternate to ram pressure stripping where the tail is not necessarily "dragging behind" the galaxy.

Finally we examine the position-tail centroid column. Here we see weaker trends among the infallers and backsplashers, but arguably no trend among the other classes. Doing a weighted two sample KS (Kolmogorov-Smirnov) test (results shown in Figure 4.2) between the position-tail centroid and random distributions statistically show the two distributions are statistically distinct for the infalling and backsplashing sample, and indistinguishable for the mergers. Among the trends we do see and can statistically confirm, we find that infalling galaxies have tails pointed away from the BGG and backsplashing galaxies have tails pointed towards the BGG. Their distributions are more spread from total alignment or

Class	Two Sample KS Test Statistic	p-value
Everything	0.0307	0.0705
Infall	0.2173	$6.846 \times 10^{-5}$
Backsplash	0.3300	$5.176 \times 10^{-9}$
Merger	0.0441	0.3261
Far Away	0.0551	0.0011

TABLE 4.2: A table of weighted two sample KS test statistics between the position-tail centroid dot product distribution of a given class and a uniform random distribution of dot products, with the null hypothesis assuming both distributions are the same. The weights (discussed in Section 2.5.3) are applied via a modification to the empirical CDF such that at some data point  $n_i$ , the eCDF increments by  $w_i/\sum w_i$  for the weight  $w_i$ . To account for variance in the random distribution, the KS test is performed between the position-tail centroid distribution and 1000 random distributions. The statistics and p-values shown on the table are averaged over 1000 tests.

anti-alignment (peaking at 1 and -1 respectively) compared to the velocity-tail centroid distribution due to their orbits not being purely radial.

For some comparisons, we adjust our sample to include both backsplashing and infalling galaxies, and include a tail mass cut of  $10^9 M_\odot$  (such that  $M_{\text{tail}} \approx M_*$ ) to emulate visual identification of jellyfish tails. We also project all vectors onto the x-y plane, and convert our dot products to angles by applying an arccosine. Comparing our results to LoTSS low z radio tails (Roberts et al. 2021a in Figure 4.3, we see peaks in tail orientations at higher angles in both cases, but the LoTSS has comparatively more tails pointed away from the BGG. Our distribution resembles the IllustrisTNG orientation distributions (Yun et al. 2019) much more, representing random orientations drawn from a uniform distribution of angles, with the distribution curve resembling a cosine (given the  $\cos\theta$  dependency in  $\vec{r} \cdot \vec{r}_{\text{cen}}$ ). We can confirm this with two sample KS tests, and despite confident

rejection of the null hypothesis in both cases, the statistic is lower between our tails and the TNG tails. This discrepancy between our tails and LoTSS tails could indicate differences between tails in groups and tails in clusters - in a cluster where the environment is denser, we would expect far more ram pressure stripping on first infall.

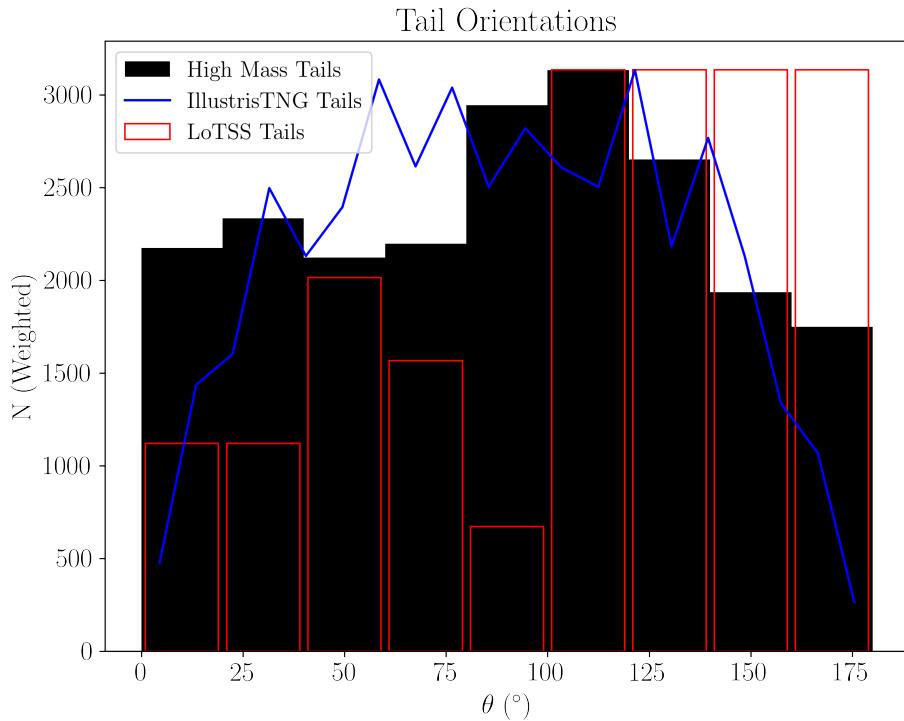


FIGURE 4.3: Tail orientation histogram of our sample (black), LoTSS cluster tails (red), and IllustrisTNG group and cluster tails (blue). The galaxies chosen here are infallers and backsplashers with  $M_{\text{tail}} > 10^9 M_{\odot}$ , and all shown are projected onto a plane. The two sample KS test statistic is 0.2883 with a p-value of  $9.431 \times 10^{-7}$  between our sample as the LoTSS tails, and 0.08326 and  $2.524 \times 10^{-26}$  between our sample and the IllustrisTNG tails. LoTSS tail data taken from figure 7 of Roberts et al. 2021a and TNG tail data taken from figure 7 of Yun et al. 2019

### 4.1.3 Tail Mass Correlations

If the galaxy tails we identify are primarily driven by ram pressure stripping, we would expect correlations between ram pressure and tail mass. In Figure 4.4 we show the modified stripping criterion (Section 2.3.4) vs tail mass for each galaxy, and surprisingly find a negative correlation. From the top row, both the linear regression fits and correlation coefficients show strong indications of a downwards trend in tail mass. Normalizing the tail masses by the stellar mass of their galaxies eliminates this negative trend for all galaxies and leaves behind weak negative correlations for the infalling and backsplashing galaxies. Physically, a high stripping criterion should represent the ram pressure force acting on the ISM greatly exceeding the gravitational pull of the stellar disk, stripping the ISM and forming a tail.

Examining Figure 4.5, we see that the stripping criterion appears to have a weak but clear negative correlation with stellar mass, particularly for the infallers and backsplashers. This is by construction, given the acceleration term in the stripping criterion depends on the galaxy’s mass. Physically, this means it is harder to strip more massive galaxies since their gas tends to be much more strongly gravitationally bound. The second row seemingly shows another set of negative correlations. However, considering the worse linear regression fits, and the fact that the correlations are already weak given they’re across four orders of magnitude, we cannot confidently say stellar mass correlates with normalized tail mass. What this lack of correlation does show however, is that despite being harder to strip, larger galaxies appear to have more tail mass simply because they contain more gas.

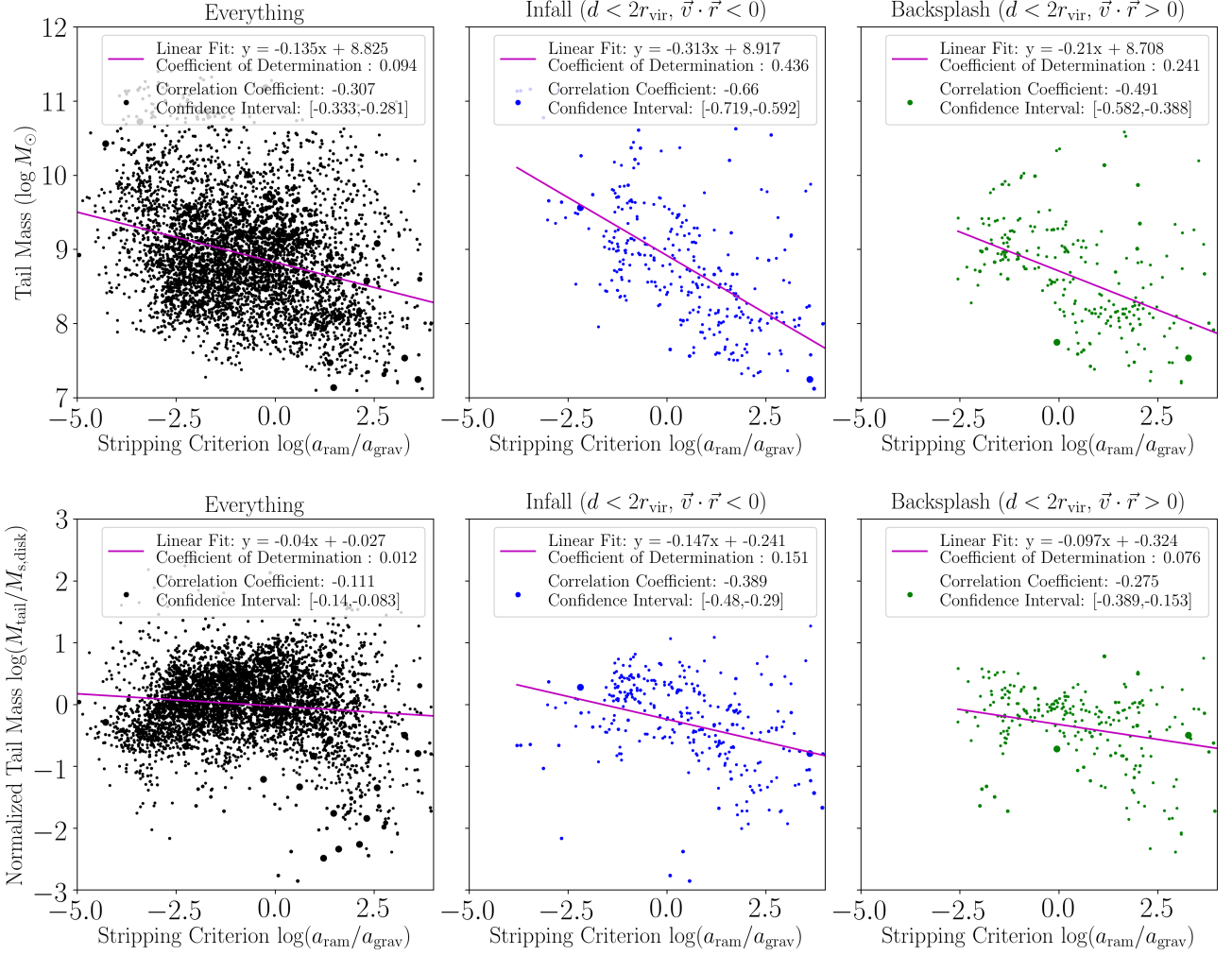


FIGURE 4.4: Stripping criterion vs tail mass and normalized tail mass scatter plots for the infalling and backsplashing classes alongside all galaxies. Dot sizes are scaled by each galaxy’s weighting. The linear fit is calculated using linear regression, with the coefficient of determination being a value between 0 and 1, evaluating the goodness of fit.

Unfortunately we cannot draw definitive conclusions from Figures 4.5 and 4.4. The correlations in normalized tail mass are too weak to draw conclusions from, and the correlations in stripping criterion reflect the built in correlation between our stripping criterion and stellar mass, and the obvious expectation that larger

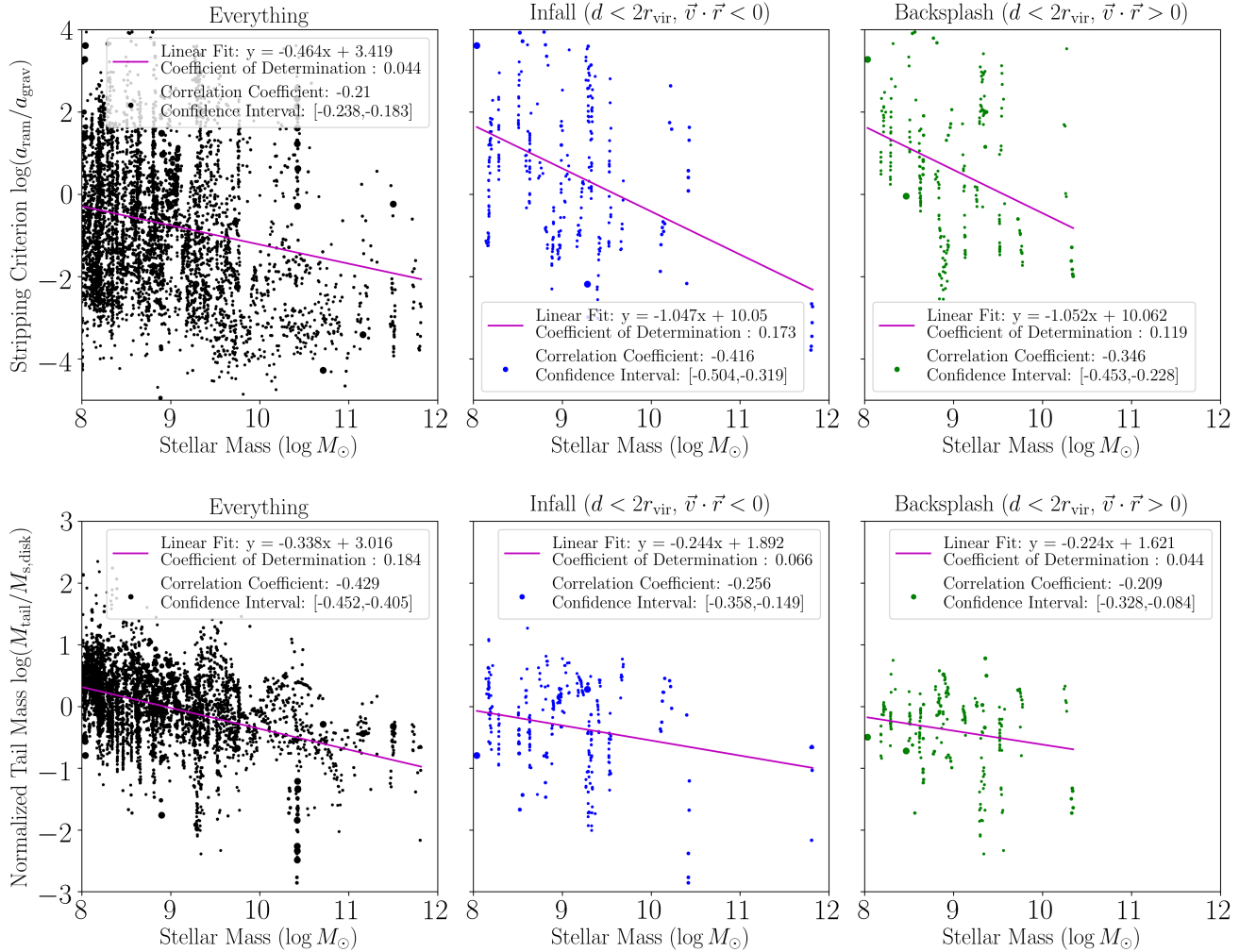


FIGURE 4.5: Star mass vs stripping criterion and normalized tail mass scatter plots for the infalling and backsplashing classes alongside all galaxies. As with Figure 4.4, point sizes are scaled by weighting, and linear regression is used for the linear fit. The vertical lines represents repeat sampling of the same galaxy, and emphasize the stability of the stellar disk, based on which we derived the characteristic radius Chapter 2

galaxies strip more gas because they have more gas. This may be reflective of a poorly defined stripping criterion, so to remove the built in galaxy mass correlation, we consider only ram pressure. However, from Figure 4.6, the correlations

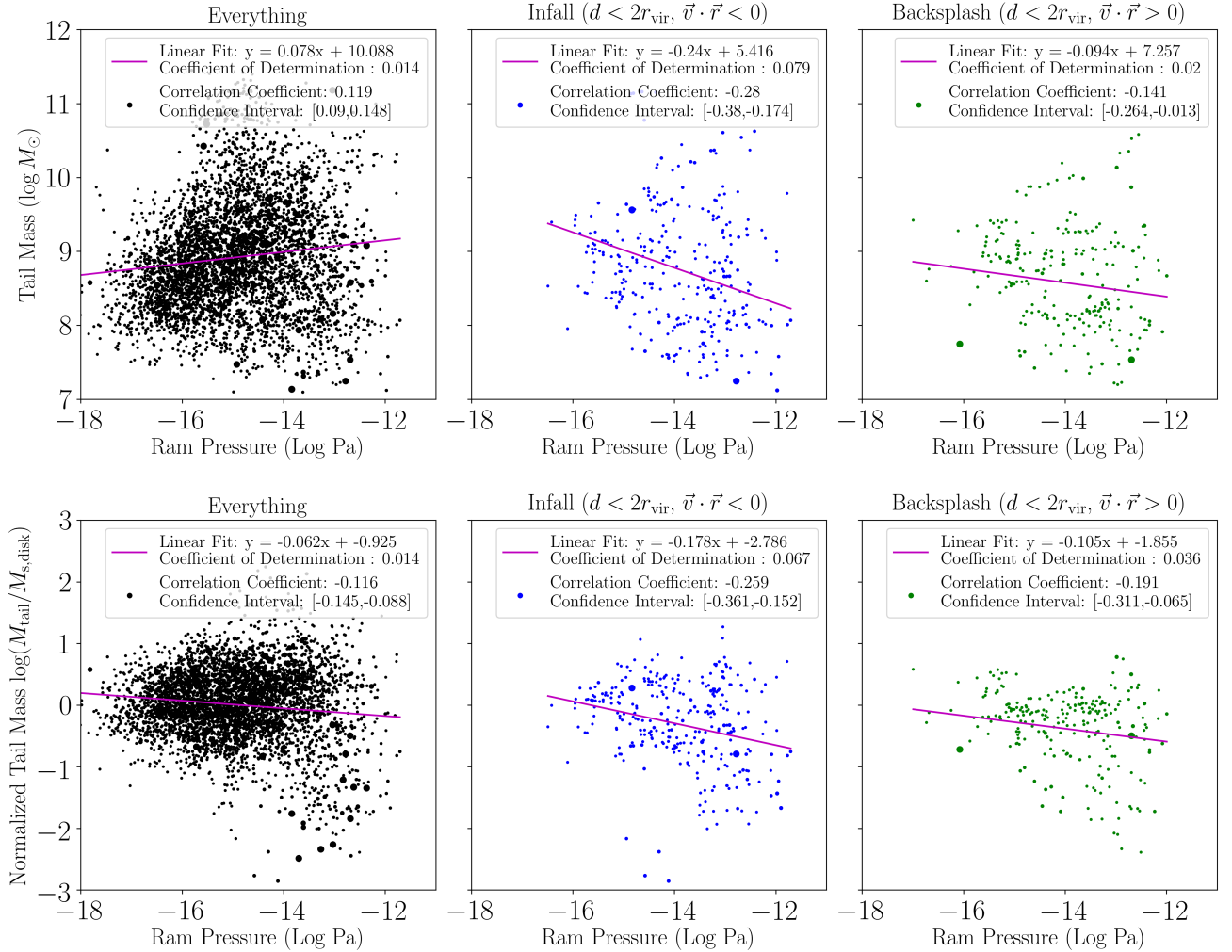


FIGURE 4.6: Ram pressure vs tail mass and normalized tail mass scatter plots for the infalling and backsplashing classes alongside all galaxies. As with Figure 4.4, point sizes are scaled by weighting, and linear regression is used for the linear fit.

are practically non-existent. As with the earlier figures, any mathematical correlation is practically non-existent considering it's observed over several orders of magnitude in ram pressure.

An alternative quantity we examine is the mass flux across the disk. From Figure 3.1 we saw that stripped material should see minimal shifts in velocity

and position across single snapshots, so there could be significant temporal offsets between an increase in ram pressure and an increase in tail mass. Mass flux should theoretically react more quickly to ram pressure. We define the mass flux as the rate of change of the gas mass within the disk. Numerically, we approximate this rate as follows:

$$\frac{dM_{\text{g,disk}}}{dt} \approx \frac{M_{\text{g,disk}}(< r_{\text{disk}}, t + \Delta t) - M_{\text{g,disk}}(< r_{\text{disk}}, t)}{\Delta t} \quad (4.1)$$

where the timestep is  $\Delta t$  (which as a reminder is 107.64 Myr in our simulation).

In Figure 4.7, we plot the ram pressure versus the stripping rate for each galaxy. We notice that ram pressure shows very weak but positive correlations with both mass loss and mass gain. As with the tail mass correlations, these correlations are weak and visible across seven orders of magnitude in ram pressure. Considering the fact this flux varies across over six orders of magnitude and that there are significant amounts of positive mass flux, it is difficult to ascertain whether our approximated mass flux represents anything physical beyond noisy fluctuations near the boundary of the disk. We can say that this noise correlates with ram pressure, but we cannot draw definitive physical conclusions.

Overall, we do not see significant links between tail mass and ram pressure stripping, and we are not able to draw definitive conclusions on the formation mechanisms of these tails. Recall that our definition of the tail particles represents gas particles between  $3r_e$  and  $R_{\text{vir}}$  with a particular velocity and a high density. The lack of correlation does not necessarily question the role of ram pressure stripping in the formation of galaxy tails - rather, it represents a lack of a correlation

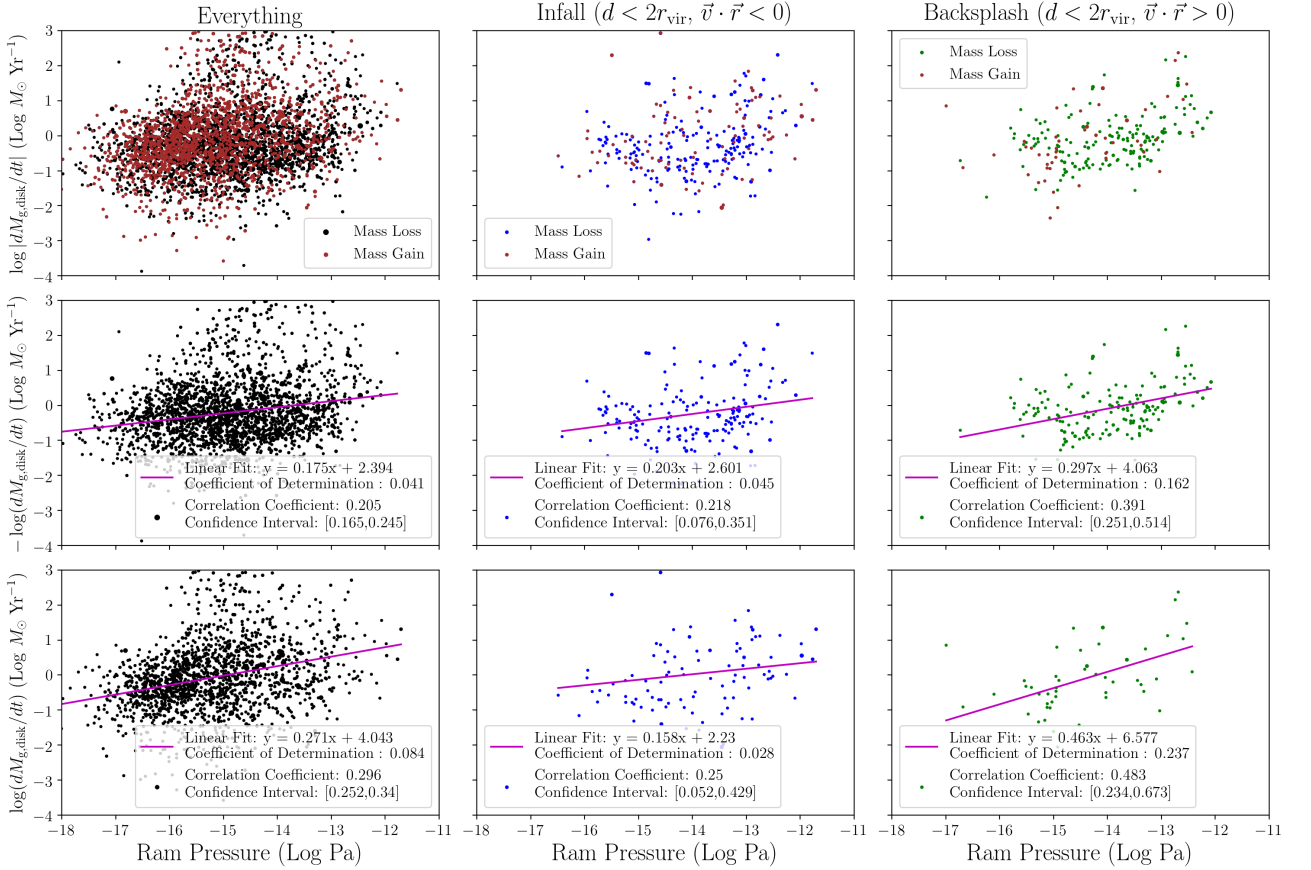


FIGURE 4.7: Ram pressure vs ISM mass flux over a single timestep for the entire sample and the infalling and backsplashing classes. As with earlier figures, each point size is scaled to their weights. The top row shows the absolute value of the mass flux, with negative fluxes shown in black and positive fluxes shown in brown. The middle and bottom rows separate out the negative and positive mass fluxes.

between our definition of the tail and our definition of ram pressure. It is possible that alternate definitions of the tail, such as a wider outer cut, different constraints

in phase space, or algorithmic morphological definitions, would show stronger statistical correlations with ram pressure. Additionally, as discussed earlier in Sections 3.5 and 4.1.1, our only sample cut attempting to eliminate non-tailed galaxies is by eliminating merging and far away galaxies. Our backsplashing and infalling samples may still include many non-tailed galaxies, and a properly cut sample of galaxies exhibiting true tails could show stronger statistical correlations with ram pressure.

We can take a different approach. Instead of a statistical analysis, we choose a few specific tailed galaxies to track over time.

## 4.2 Time Evolution

From an array of galaxy maps similar to Figure 3.2, we visually select a group of infalling and backsplashing galaxies with prominent and well defined tails. Using our merger trees, we can trace the entire history of these galaxies. To avoid artificial fluctuations in quantities such as ISM mass, which can be sensitive to the radial cut representing the disk, we fix  $r_e$  to its value at  $z = 0$  when calculating quantities for ancestors. These galaxies were also selected to be massive enough to have good resolution, but low enough mass to be strongly susceptible to ram pressure stripping. From a sample of thirty hand picked galaxies from  $z = 0.67$  to  $z = 0$ , they were all found to represent four distinct branches <sup>1</sup>

---

<sup>1</sup>As a reminder the branch represents the evolutionary history of a galaxy, and was defined and discussed in Section 2.5.2. For the sake of clarity, we will refer to branches as galaxies in the rest of this thesis.

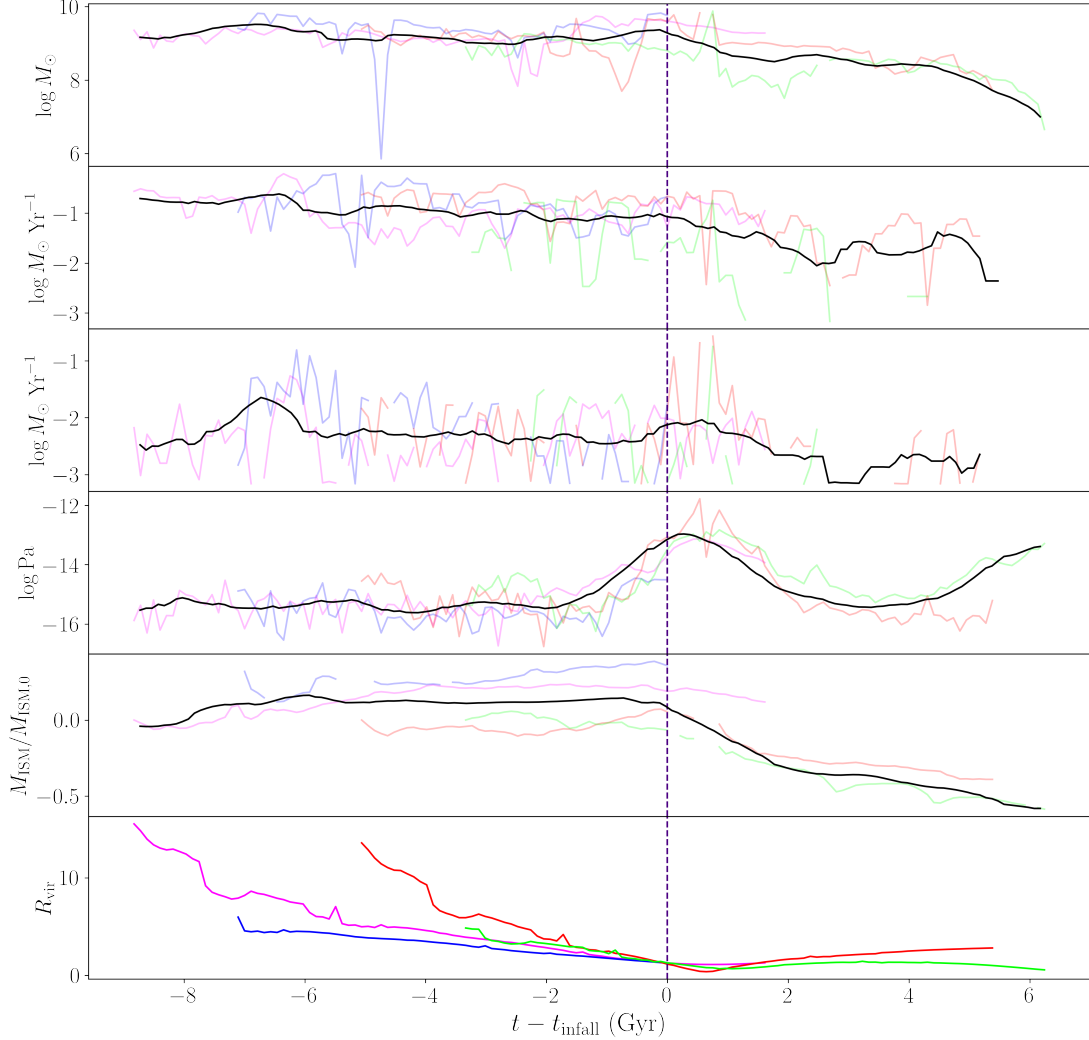


FIGURE 4.8: Six quantities tracked over time for our four galaxies. From top to bottom: tail mass, star formation rate (total), star formation rate (tail), ram pressure, ISM mass ratio, group-centric distance. The ISM ratio represents the ratio between the ISM mass at a given time versus the initial ISM mass. Bad data points in the ISM masses representing inaccurate halo positions from the halo finder are removed (where the mass changes by more than 25% within a single snapshot). The  $x$  axis shows the time subtracted by the time of the galaxy’s first infall within  $1.3 R_{\text{vir}}$  of the group. Each colour represents one of the four galaxies - blue is 4392, magenta is 3626, red is 10641 and lime is 4347. The black lines represent an average curve with a 1 Gyr time window

Halo ID	$M_*$ ( $M_\odot$ )	Status	Pericenter ( $R_{\text{vir}}$ )	$M_{\text{ISM},0}$ ( $\log M_\odot$ )	$M_{\text{ISM}}$ ( $\log M_\odot$ )
10641	$2.704 \times 10^9$	Backsplash	0.3743	9.769	9.378
3626	$6.713 \times 10^9$	Backsplash	1.110	9.599	9.717
4347	$5.729 \times 10^8$	Second Infall	0.5616	9.374	8.787
4392	$1.508 \times 10^{10}$	Infall	1.255	9.681	10.038

TABLE 4.3: A table showing the stellar mass and status of each galaxy at  $z = 0$ .  $R_{\text{vir}}$  here refers to the group virial radius. From left to right we have the halo ID, stellar mass, status at  $z = 0$ , closest pericenter approach, initial ISM mass, and  $z = 0$  ISM mass. Initial ISM mass here refers to the ISM mass of the earliest tracked ancestor of the galaxy. Galaxy 4347’s status as a second infaller means it has already went through a pericenter passage and is falling back in for a second passage. Galaxy 648-1286 (see Chapter 3) is an ancestor of galaxy 10641.

In Table 4.3 we show the properties of these four galaxies. We see that the galaxies at  $z = 0$  have varying masses but generally fall in the same low-medium mass galaxy range as their tailed ancestors. Having three of the four galaxies having already undergone a pericenter passage also allows us to track a more complete history of tail formation and other quantities. To perform proper comparisons between the galaxies, we shift the time axis to their first infall time, which we define to be 1.3 virial radii instead of 1 virial radius to account for galaxy 3626’s closest approach being outside the virial radius and galaxy 4392’s infalling status at  $z = 0$ .

In Figure 4.8, we can see the radial trajectories of the galaxies, and confirm both the  $z = 0$  status and closest approach of the galaxies from Table 4.3. The fluctuations in the radial trajectory plot reflect fluctuations in  $R_{\text{vir}}$  of the group and do not represent actual movement of the galaxies (the same patterns can be seen in several of the trajectories).

While two of the galaxies very recently infell at  $z = 0$ , for the other two galaxies 10641 and 4347 which have both gone through a pericentre passage, we see a steady

drop in ISM mass. This finding consistent with those of Joshi et al. 2019, who saw losses in total gas mass for infalling galaxies. Assuming tails are primarily the product of ram pressure stripping, we should expect decreases in ISM mass to correlate with increases in tail mass, possibly with some offset in time. However, examining the ISM mass and tail mass over time we do not see the expected correlation between them. There are no significant trends in before infall, and a steady decrease in both quantities after infall.

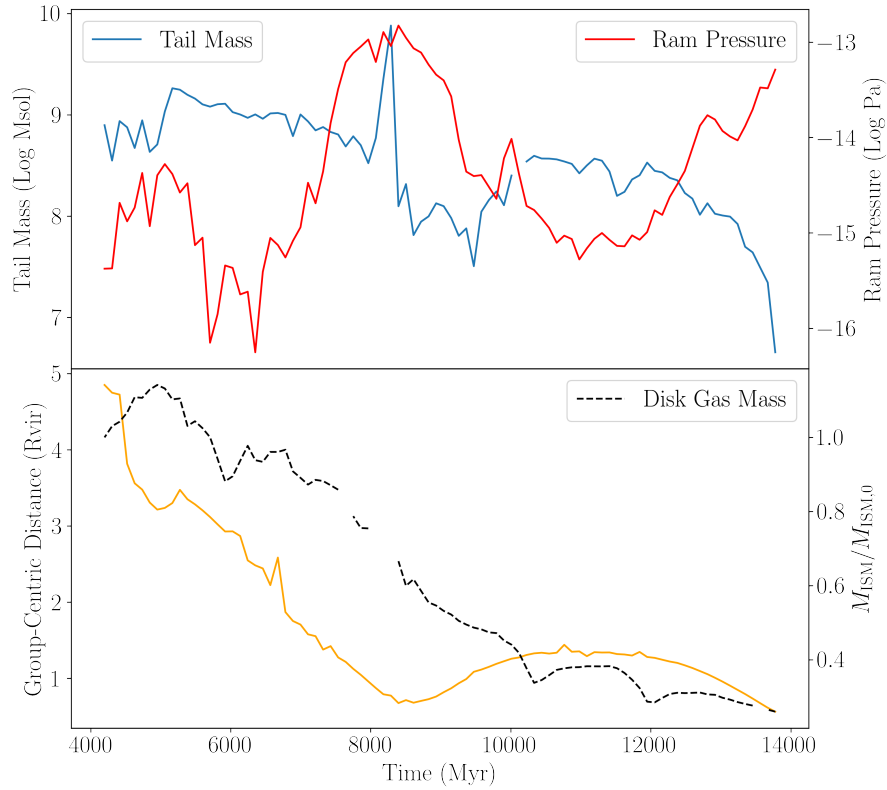


FIGURE 4.9: The time evolution of galaxy 4347. As with Figure 4.8, the bad data points in ISM mass are removed. The yellow curve represents the radial trajectory of the galaxy

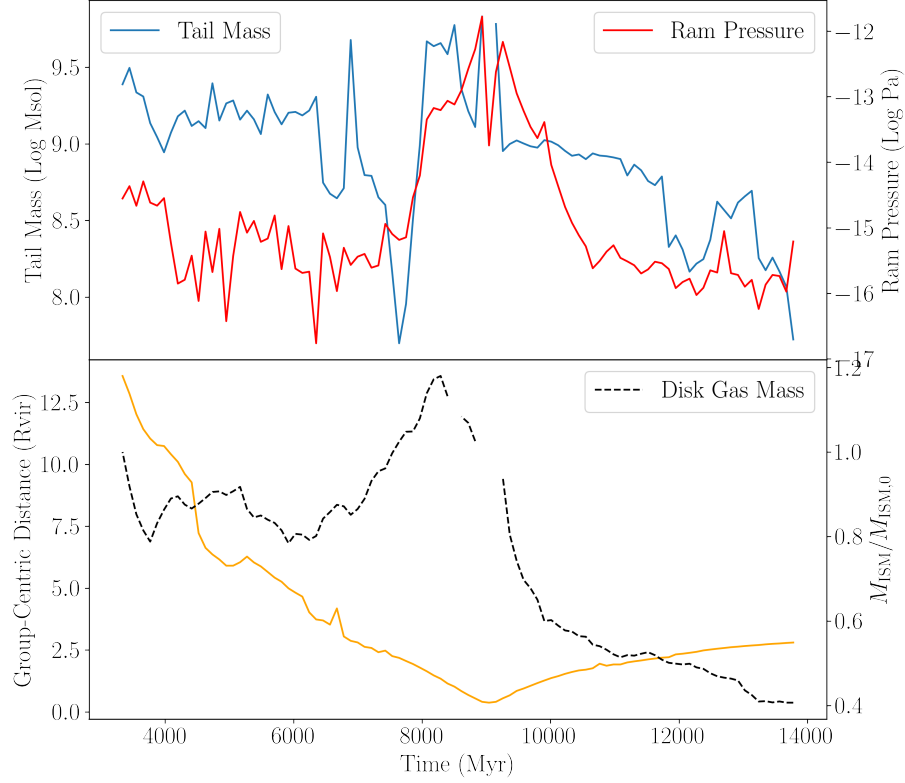


FIGURE 4.10: The time evolution of galaxy 10641. As with Figure 4.8, the bad data points in ISM mass are removed. The yellow curve represents the radial trajectory of the galaxy

Comparing the star formation rates and tail star formation rates, we can see a very slow decrease in overall star formation indicative of starvation-driven quenching, but a slight uptick in tail star formation right after infall indicative of a slight star formation boost possibly driven by ISM compression. Star formation in tails is consistent with observational studies (Vulcani et al. 2018), though we do not observe enhanced total star formation in the entire galaxy as predicted by various isolated wind tunnel simulations (Steinhauser et al. 2012, Ramos-Martinez et al.

2018). This is likely due to having poorer resolution, resulting in high stochasticity in the star formation.

Across all plots in Figure 4.8 only in ram pressure do we see a significant and consistent trend up as the galaxies infall and perform their pericenter passages. This is expected given that ram pressure is a proxy for group-centric distance, given  $P_{\text{ram}} = \rho v^2$ , and the IGM density  $\rho$  increases significantly as galaxies approach the centre.

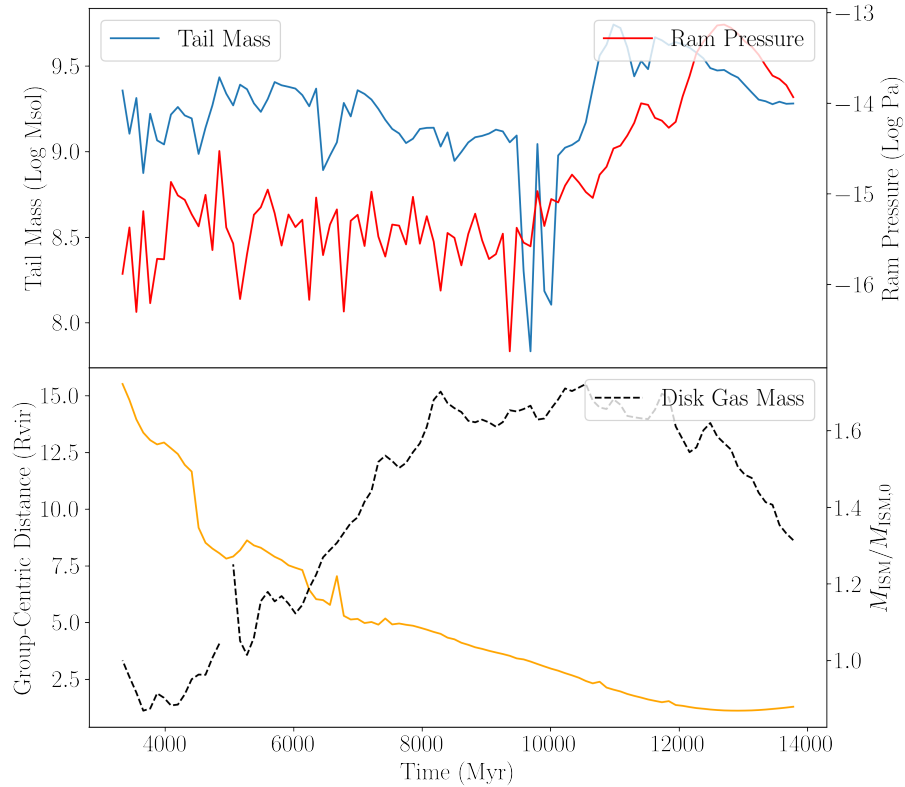


FIGURE 4.11: The time evolution of galaxy 3626. As with Figure 4.8, the bad data points in ISM mass are removed. The yellow curve represents the radial trajectory of the galaxy

To better visualize correlations between tail properties and galaxy properties in individual galaxies, we show the three galaxies 4347, 3626 and 10641 that have undergone a full pericenter passage by  $z = 0$  in Figures 4.9, 4.11 and 4.10. Examining the ISM mass, galaxy 4347 shows a consistent depletion across its entire history, while galaxies 3626 and 10641 show depletion as ram pressure spikes, with active accretion happening before depletion. This is consistent with expectations that ram pressure strips the ISM. Examining the tail mass, in galaxy 4347 we see the tail mass decreasing as a result of the spike in ram pressure, and increase again as the galaxy backslashes before decreasing a second time for its second infall. Galaxies 3626 and 10641 show an increase in tail mass alongside an increase in ram pressure. Curiously however, the tail mass appears to peak before the ram pressure peaks (approximately 500 Myrs for 10641 and 1 Gyr for 3626). This trend is also visible to some extent with the second infall of galaxy 4347, with a local maximum in tail mass at the local minimum of ram pressure. While time offsets are expected between peaks in ram pressure and peaks in tail mass, the tail mass peaking before the ram pressure peak is unexpected under the assumption that ram pressure stripping forms tails. Another peculiar detail is the lack of sensible correlation between ISM mass and tail mass: in galaxy 4347, the second spike in tail mass upon approach to second infall does not appear to line up with any significant and consistent drops in ISM mass; in galaxies 3626 and 10641, the ISM mass remains relatively static or significantly increases as the tail mass spikes. From Figures 4.9, 4.11, 4.10 and 4.8, alongside Table 4.3, we can see that the ISM and tail masses are of comparable values within an order of magnitude, with the tail mass approximately tripling in the spikes for galaxies 3626 and 10641. The changes in tail mass are far more significant than the changes in ISM mass.

Comparing the ram pressure and ISM mass reveals a complicated relation that varies across galaxies, but there is evidence of increases in ram pressure being associated with decreases in ISM mass in all three galaxies. Taking into account our lack of observed statistical correlations across our sample, the lack of correlation between ISM mass and tail mass, alongside the peaks in tail mass preceding peaks in ram pressure suggest additional tail formation mechanisms beyond ram pressure stripping of the ISM. It is clear that increases in tail mass does not correspond to decreases in ISM mass. Either gas is funneled into the ISM as ram pressure stripping is occurring, or tails consist of more than stripped ISM. We turn to more detailed examination of the tail particles themselves.

## **4.3 Entrainment**

In this section we explore the properties of individual tails in more depth and track the individual particles over time to examine their origins. In Figure 4.12, we present two galaxies we examine in more depth, at a time when they are on their first infall. Galaxy 648-1286 is an ancestor of galaxy 10641 at around  $z = 0.5$ , and galaxy 584-5100 is an ancestor of galaxy 4347 at around  $z = 0.63$

### **4.3.1 Where did Tail Particles Originate?**

To trace the origins of tail particles, we must track these particles across multiple snapshots. Each particle has a unique ID across all snapshots it exists in, with no two particles ever sharing this ID, even if one particle is destroyed and another particle is created at some later time.

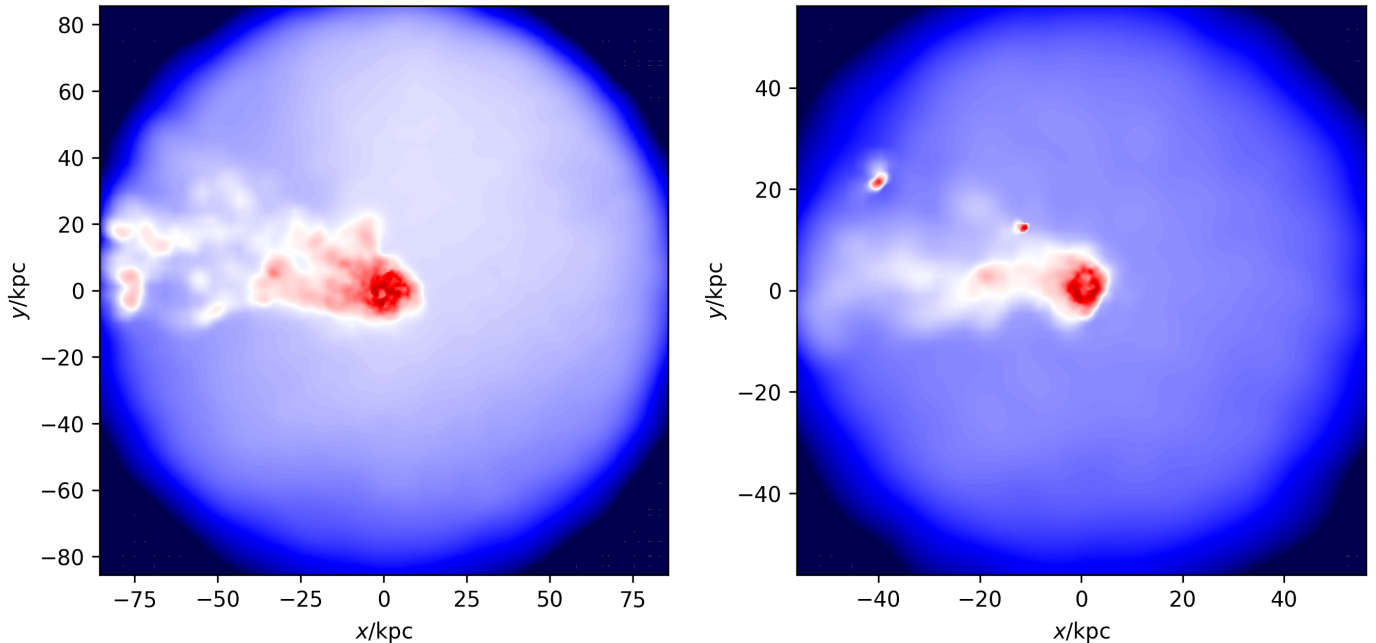


FIGURE 4.12: Gas density maps for galaxy 648-1286 (left) and galaxy 584-5100 (right), representing ancestors of galaxies 10641 and 4347 respectively. These maps are oriented such that the galaxy velocity points in the  $x$  direction and the tail vector lies in the  $xy$  plane.

With all tail particles identified, we track these particles back in time and see where they were at previous snapshots, and flag particles that ever entered the disk. Here we define "ever entered the disk" as a particle having been within  $3r_e$  of the galactic center at some point in the past. This flag will serve as a rough indicator of particles stripped from the ISM. We take a section of galaxies 10641 and 4347 comprising of 31 snapshots (around 3.2 Gyrs), ending at galaxies 648-1286 and 584-5100 respectively, right around when the galaxies cross the virial radius.

Figure 4.13 shows a very surprising result - only 70% of the total tail mass was ever the disk! Considering the fact that this includes particles that sweep by the

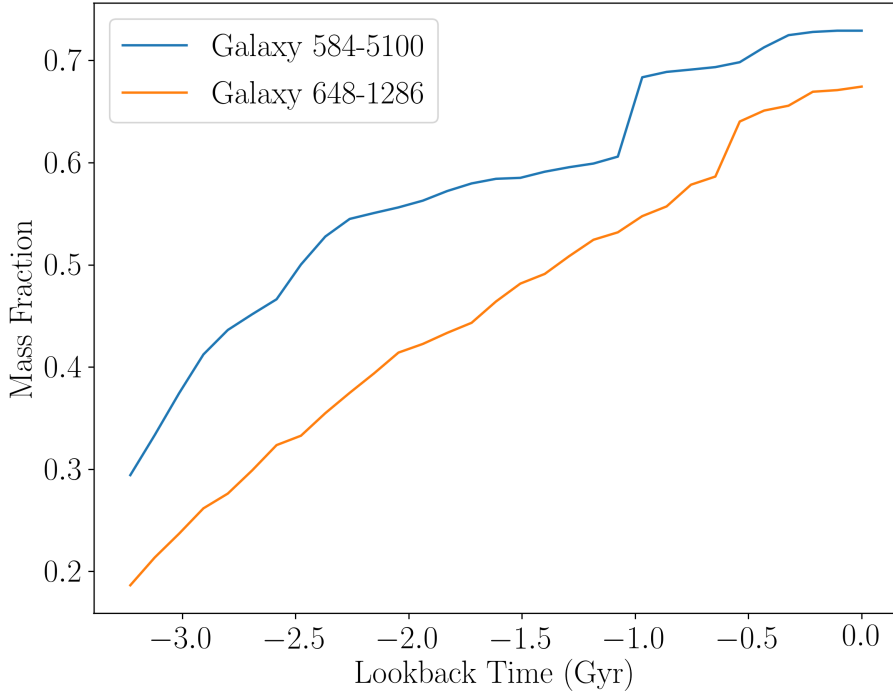


FIGURE 4.13: The mass fraction of tail mass that ever entered the disk vs the total tail mass, over time. This plot is cumulative, meaning any particles that enter the disk are counted, and remain counted even if they leave. The positive mass fractions at -3.2 Gyrs represent tail particles that started out in the ISM.

edge of the disk and are only within  $3r_e$  for one or two snapshots, the real stripped fraction is likely lower. This tells us that at least 30% of the observed tail at a given point in time is not stripped material, and came from other sources such as the CGM or the group. While the value of this stripped fraction is sensitive to the choices made in our tail identification procedure, compared to standard visual identification methods our cuts are more restrictive since we consider not only density but also velocity. A less restrictive set of cuts, say density only, would likely include even more non-stripped-ISM material in the tail. From Figure 4.14

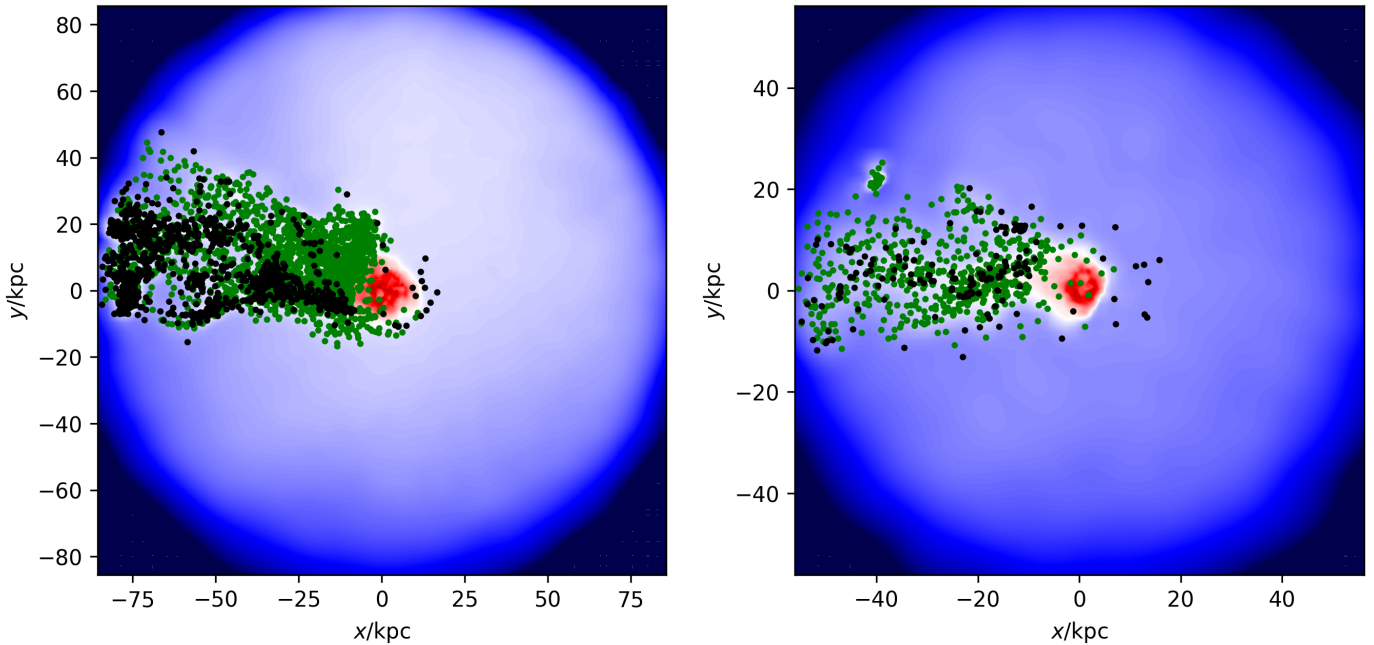


FIGURE 4.14: The same gas density maps as Figure 4.12, but with tail particles positions on top. The green particles represent gas that entered the ISM at some point in the last 3.2 Gyrs, and the black particles represent gas that never entered the ISM.

we can visually see these non-stripped particles represent a significant portion of the tail. We define this population of gas as "Entrained".

In Figure 4.15, we track the positions of the tail particles 3.2 Gyrs back. We see both to-be stripped and entrained particles well distributed amidst the CGM (which as a reminder we define as the annulus between  $3r_e$  and  $R_{\text{vir}}$ , with some to-be stripped particles in the ISM. The to-be stripped particles in the CGM will fall within  $3r_e$  of the galaxy center at some point in the next 3.2 Gyrs.

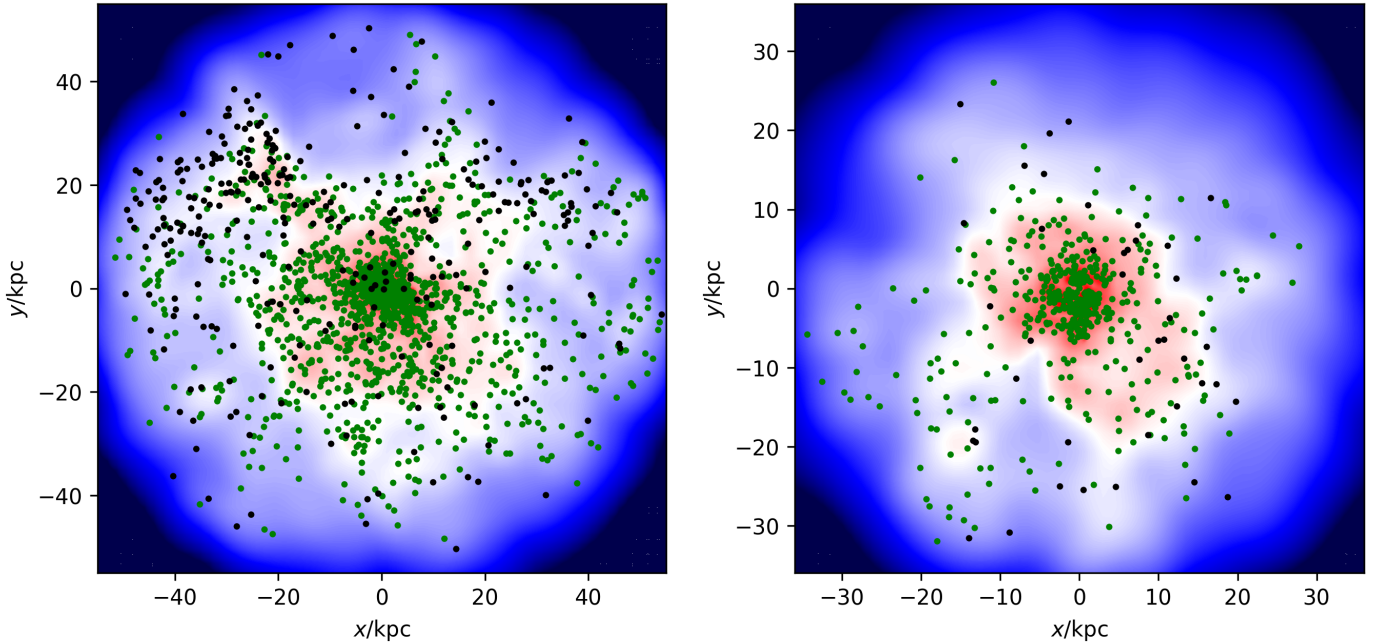


FIGURE 4.15: Gas density maps of galaxy 648-1286 (left) and 584-5100 (right), but 3.2 Gyrs back in time. These galaxies are direct ancestors of galaxies 648-1286 (left) and 584-5100 (right). The tail particles from the current time are tracked back and the positions of the tail particles that remained within  $R_{\text{vir}}$  3.2 Gyrs ago are shown on the maps. The colour scheme of the particles are shared with Figure 4.14. A particle coloured green but in the CGM in the above maps means that particle will enter the disk at some point in the future before becoming a part of the tail.

### 4.3.2 Particle Trajectories

We can get a better grasp on the formation mechanisms of these tails by tracking the trajectories of the particles over time. For the sake of efficiency, we only track particles that survived all 31 snapshots (gas particles created during these 3.2 Gyrs are ignored), which thankfully only amounts to a few ignored particles amidst thousands of tracked particles. Examining Figure 4.16 we see many similarities between the trajectories of stripped and entrained particles for the two galaxies. The entrained gas generally lives in the CGM between 10 and 100 kpc from the

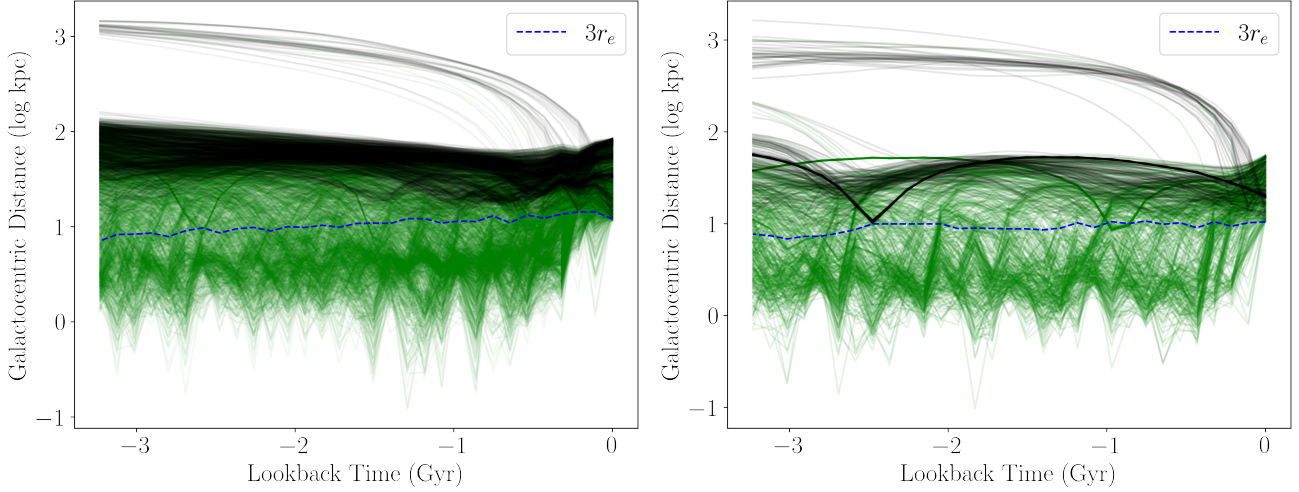


FIGURE 4.16: Radial tail particle trajectories over time for galaxy 648-1286 (left) and galaxy 584-5100 (right). The trajectories of all particles that survived all 3.2 Gyrs are plotted. As with earlier figures, green represents stripped gas, and black represents entrained gas

disk, while the stripped gas occupies the same outer bound but also lives well within the disk, indicative of its accretion onto/existence within the ISM. The arch like structures of trajectories near the disk show particles oscillating between two radii from the center. These resemble pericenter and apocenter passages, representing the particles' keplerian orbits and the rotation of the disk. The thick black line in the trajectories for galaxy 584-5100 represent a dense gas clump undergoing a keplerian orbit about the galaxy, with all particles in the clump sharing near identical trajectories. We also see thick green lines in both trajectories, suggestive of a gas clump that did enter the disk but only for a few snapshots. This helps illustrate the fact that the entrained fractions in Figure 4.13 represent lower limits, since it's clear these clumps are not ISM material. Both galaxies also share a small population of entrained gas that originated from the group, starting at around 1 Mpc away and slowly moving towards the galaxy and accreting onto the tail.

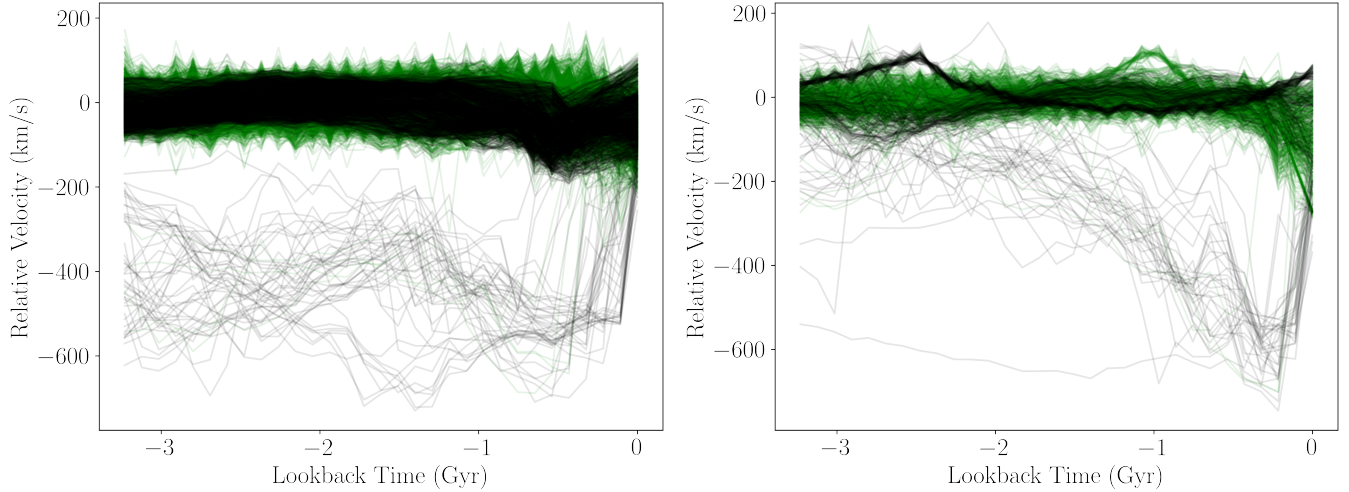


FIGURE 4.17: Projected relative velocity tail particle trajectories over time for galaxy 648-1286 (left) and galaxy 584-5100 (right). The velocity of each gas particle relative to the galaxy are projected onto the galaxy’s velocity vector, and a change of basis is made such that the galaxy’s velocity vector is a principle axis. The resulting projected relative velocities are plot-able scalars. The trajectories of all particles that survived all 3.2 Gyrs are plotted, with appropriate alphas chosen to optimize visibility. As with earlier figures, green represents stripped gas, and black represents entrained gas

The effects of stripping can also be seen starting around -400 Myr in both galaxies. We see the gas in the ISM beginning to rapidly move out of the disk, with all of the green radial trajectories moving up and away from the center of the galaxy. Examining the velocity trajectories in Figure 4.17 we can see a more prominent and dramatic shift starting at around the same time. Galaxy 648-1286 exhibits a small shift in stripped gas velocity, but a large and rather sudden shift in entrained gas velocity, while galaxy 584-5100 exhibits similar shifts in both stripped and entrained gas velocities. It’s also clearer in the velocity trajectory map of galaxy 584-5100 the presence of the orbiting gas clump mentioned earlier - we see one clump accounting for a significant portion of the entrained portion of the tail, and the other clump counted as stripped ISM since it grazed by the disk.

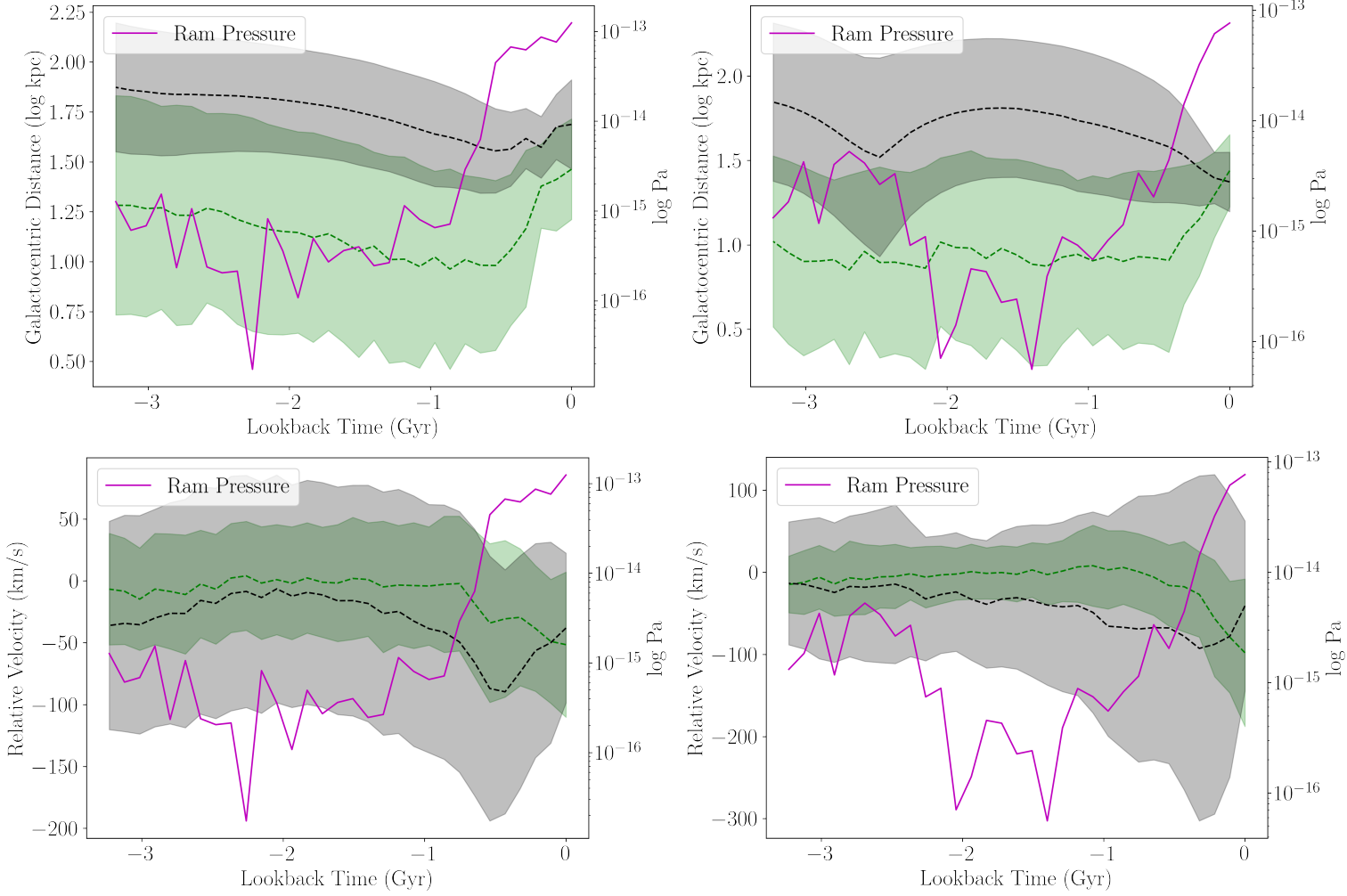


FIGURE 4.18: The same plots as Figures 4.16 and 4.17 (Radial and projected relative velocity trajectories of all particles), modified for visibility. The dashed lines represent the average trajectories, with the shaded region representing one sigma. As with earlier figures, green represents stripped gas, and black represents entrained gas. The solid magenta line shows the ram pressure over time, with values shown on a second y axis on the right.

Both galaxies also show a rapid deceleration of entrained group gas in the last 400 Myrs, though curiously galaxy 584-5100’s group gas shows a slow acceleration preceding this deceleration.

In Figures 4.16 and 4.17 we see significant shifts in position and velocity in the last 400 Myrs, indicative of some stripping force on all gas populations. We also note distinct populations of gas with very high velocity and positional offsets accreting onto the tail at later times, which is strongly indicative of violent momentum mixing processes. In Figure 4.18 we average the trajectories from Figures 4.16 and 4.17, and overlay the ram pressure over time on top. With ram pressure spiking several orders magnitude in the last 400 Myrs alongside these shifts in position and velocity, this strongly suggests ram pressure to be the underlying cause. Interestingly, it is not just stripped gas, but both the stripped and entrained gas, that are perturbed by ram pressure. We will discuss this in more detail in the last section.

### 4.3.3 Mixing

Velocity and galactocentric distance aren't the only properties we can track over time. Now that we have identified the two distinct distributions of gas (stripped ISM gas and entrained gas), we can compare some of their properties - namely metallicity and temperature. For some gas particle with mass  $M$  containing hydrogen mass  $m_{\text{H}}$  and helium mass  $m_{\text{He}}$ , we define metallicity as the metals fraction  $Z$  where

$$Z = 1 - \left( \frac{m_{\text{H}}}{M} + \frac{m_{\text{He}}}{M} \right) \quad (4.2)$$

In other words,  $Z$  is the mass fraction of all elements heavier than Helium.

In Figure 4.19 we see convergence in temperature distributions for both the entrained and stripped gas. The stripped gas appears to be a single distribution up until the current time, where we see a small plateau of hot gas appear. We also see

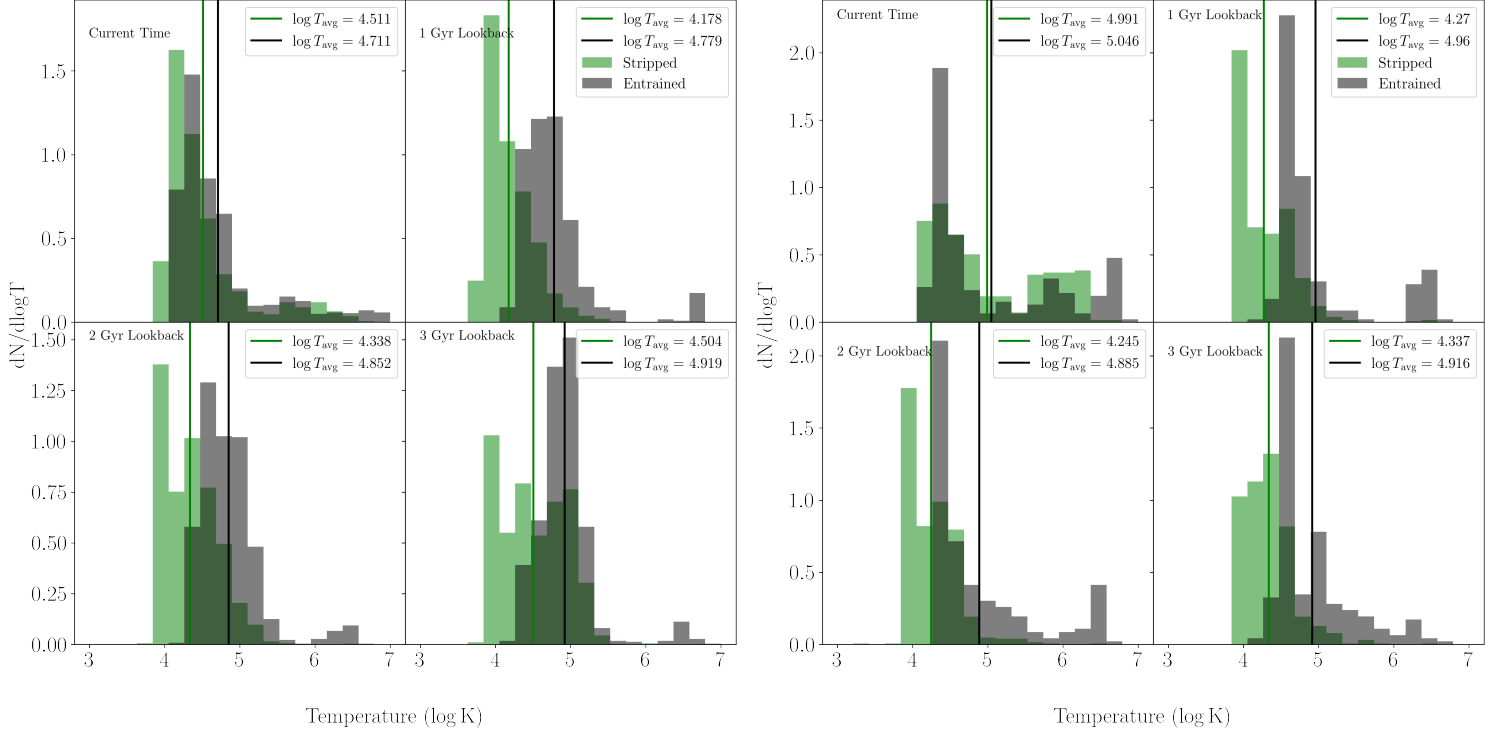


FIGURE 4.19: Histograms of tail particle temperatures for galaxy 10641 (left) and galaxy 4347 (right) taken at four distinct times: Current time, -1 Gyr lookback, -2 Gyr lookback and -3 Gyr lookback. Green and black represent stripped and entrained gas (consistent with previous figures). Solid green and black lines show averages of the log temperatures.

a significant upwards shift in mean temperature in the stripped gas at the current time. Examining the entrained gas distribution we can see it follows a similar shape to that of the stripped gas, but has a small peak of hot gas. Tracking the evolution of this distribution and we observe what appears to be two phased behaviour - the bulk of the entrained gas appears to cool and converge onto the stripped gas, while a small amount of entrained gas heats up and forms a high temperature plateau in the distribution. Interestingly this two phased behaviour when combined results in minimal shifts in the mean temperature of the entrained gas when compared to the shifts in the stripped gas mean temperature. These observations from the

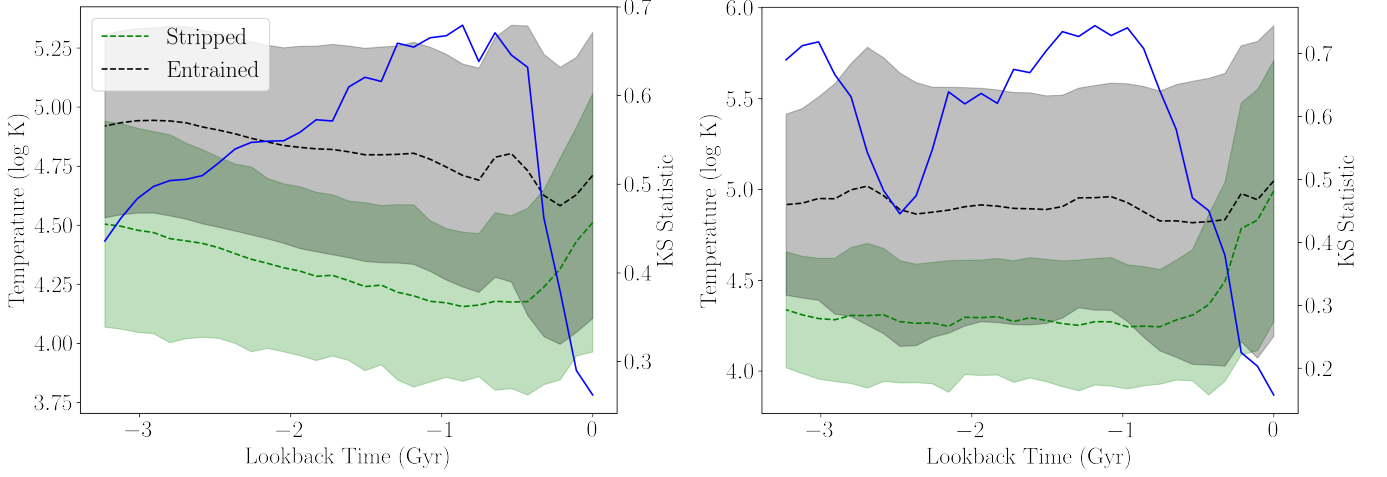


FIGURE 4.20: Average temperature trajectories of the entrained (black) and stripped particles (green) for galaxy 10641 (left) and galaxy 4347 (right), with shaded regions showing one sigma. A two sample KS test is performed at each snapshot between the entrained and stripped gas distributions, with the resulting statistic plotted in blue.

histograms evidence mixing between the stripped and entrained gas, in addition to mixing between both populations of gas and the IGM.

In Figure 4.20 we look at the average trajectories (alongside  $1\sigma$  spread) of the stripped and entrained gas temperatures. We see the entrained and stripped distributions for both galaxies remaining relatively separate until the last few hundred Myrs, where we see a sharp uptick in stripped gas temperature, while the mean entrained distribution remains relatively constant in temperature. Specifically, for galaxy 648-1286 we see a steady decrease in the stripped gas temperatures. This likely represents the cooling of CGM gas (the green particles in the CGM from Figure 4.15) as it falls into and mixes with the ISM. Our earlier observation of convergence between the two distributions are quantified here using a two sample KS test, which over time shows a sharp downwards turn in its statistic as the

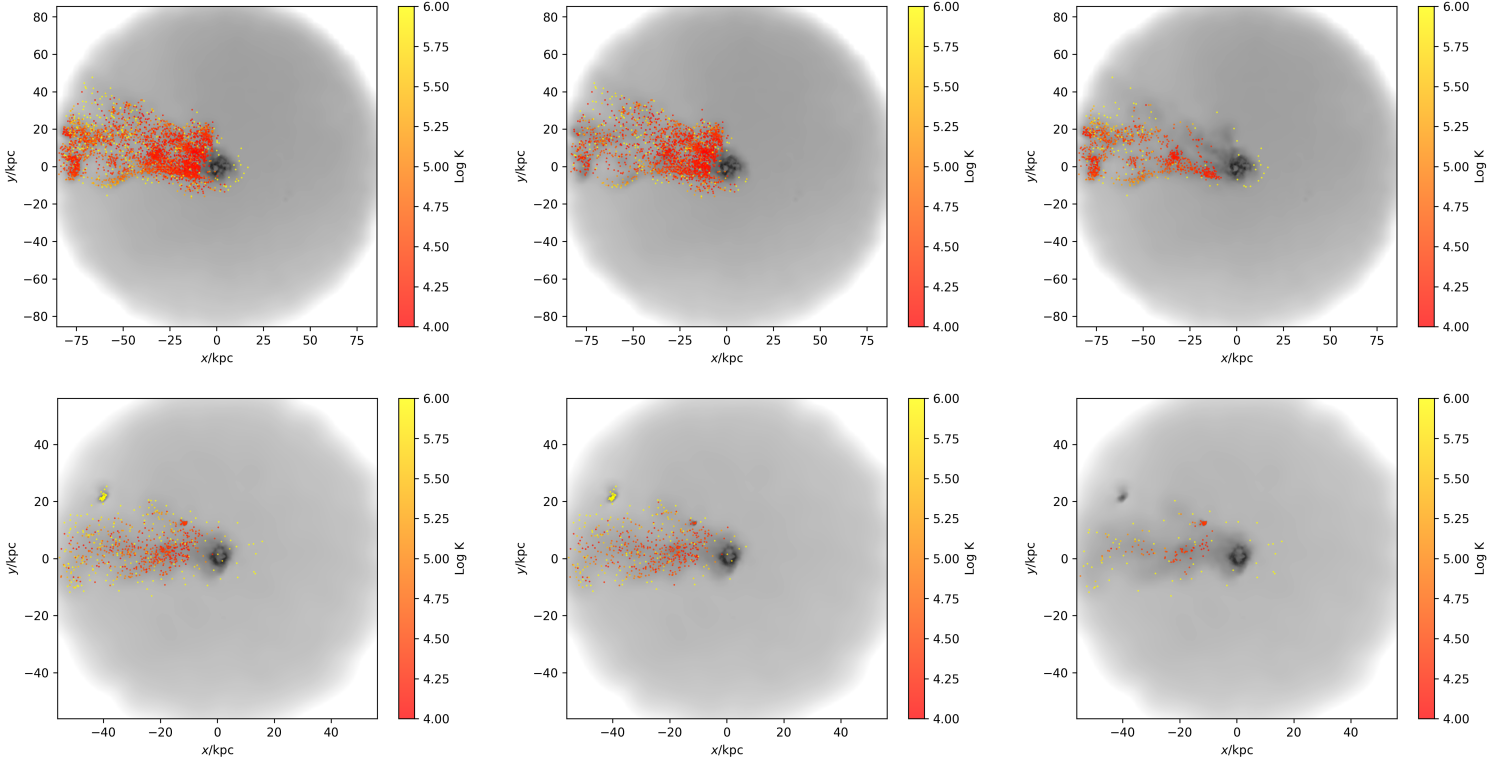


FIGURE 4.21: Greyscale gas density maps of galaxy 648-1286 (top) and 584-5100 (bottom) with tail particles plotted on top. The colouring of the tail particles represents their temperatures on the colour bar shown on the right of each map. The first column shows all the gas, while the middle and right columns separate out the stripped and entrained gas respectively

stripped gas heats up, representing increasing confidence in the null hypothesis that both distributions are the same. This rapid stripped gas heating and convergence between the two gas populations also correlate strongly with the spikes in ram pressure and position/velocity perturbations as seen in Figure 4.18, indicating that this heating is likely the direct result of stripping. The two phased behaviour of the entrained gas mentioned earlier can be seen in the increasing spread of temperatures moving forwards in time, where part of the entrained gas cools as it mixes with the stripped ISM, while another part heats as it mixes with the IGM.

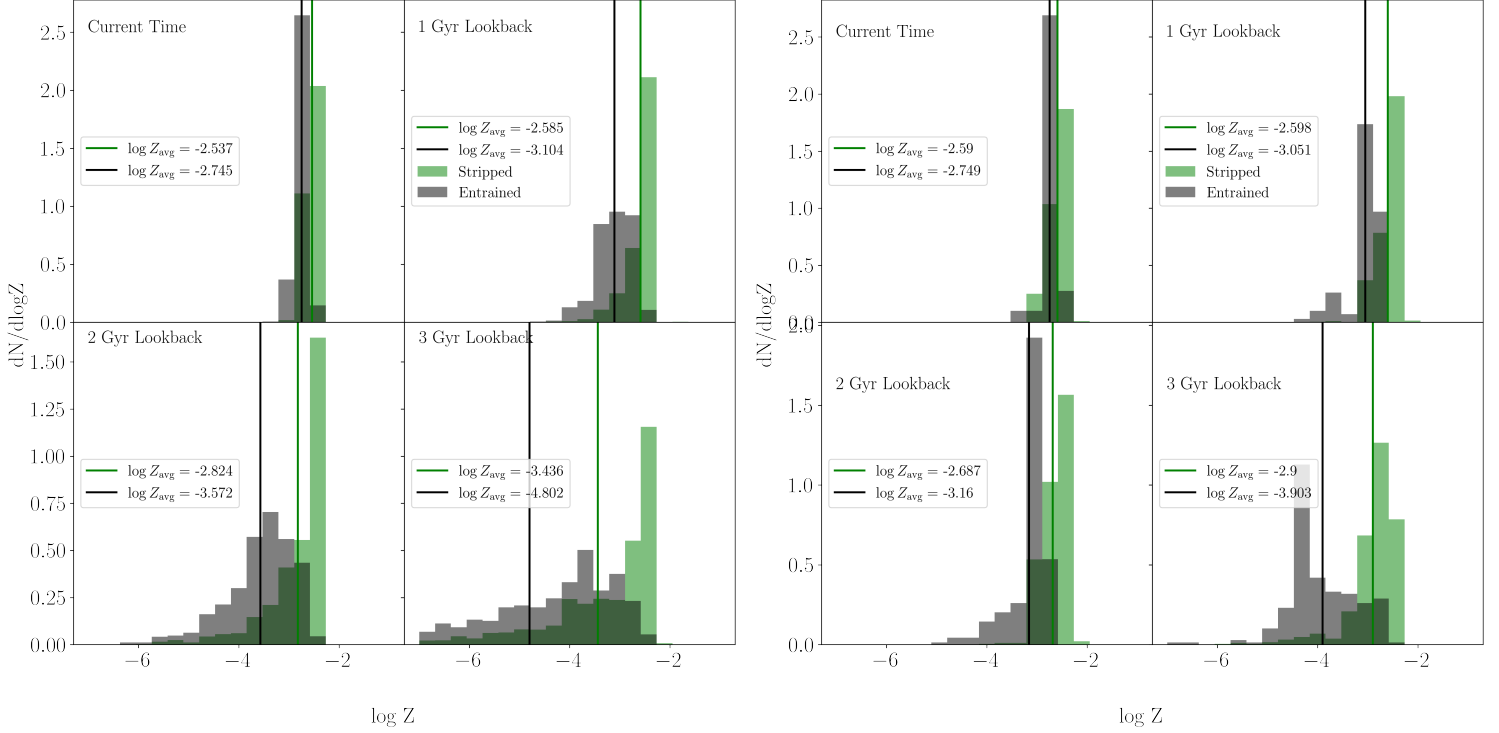


FIGURE 4.22: Histograms of tail particle metallicities for galaxy 10641 (left) and galaxy 4347 (right) taken at four distinct times: Current time, -1 Gyr lookback, -2 Gyr lookback and -3 Gyr lookback. Green and black represent stripped and entrained gas (consistent with previous figures), with alphas applied to show overlaps in the distributions. Solid green and black lines show averages of the log metallicities.

Figure 4.21, which shows the temperature of each tail particle, paints a clearer picture. Focusing on galaxy 648-1286 (since it exhibits a more well defined tail), we see mostly cool gas within the tail with warmer gas on the boundary of the tail, consistent with Figure 3.3. We see that for the stripped ISM, most of the hotter particles appear on the boundary of the tail. Combining this with our observations in Figure 4.20, we can conclude the observed heating of the stripped gas is the product of mixing between the boundary layer of the tail and the hot group medium, consistent with the findings of Müller et al. 2021. We also observe

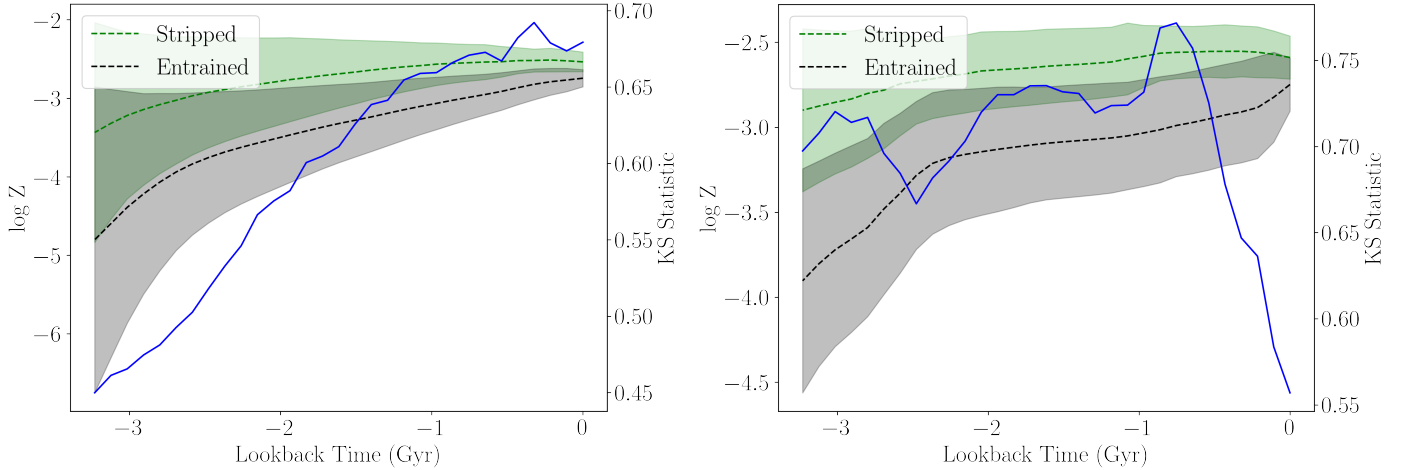


FIGURE 4.23: Average metallicity trajectories of the entrained (black) and stripped particles (green) for galaxy 10641 (left) and galaxy 4347 (right), with shaded regions showing one sigma. A two sample KS test is performed at each snapshot between the entrained and stripped gas distributions, with the resulting statistic plotted in blue.

cool pockets of entrained gas well below  $10^5$  K and a spread of hotter entrained gas particles, consistent with Figures 4.19 and 4.20 in showing the result of mixing with both the stripped ISM and the IGM.

The metallicity, however, tells a different story. Looking at Figure 4.22, both distributions of gas appear to have increasing metallicity over time, with the entrained distribution converging onto the stripped distribution. This is further evident in Figure 4.23, where again we see a steady increase in both distributions of gas. While the metal enrichment of the stripped gas can be attributed to accretion onto the ISM, the same does not apply for the entrained gas since by definition it never entered the disk. A possible source of the entrained gas’ metal enrichment could be through mixing with the stripped gas. Unlike the temperature however,

this metal mixing does not appear to correlate with the position/velocity perturbations or ram pressure. The convergence appears smooth throughout the entire 3.2 Gyr time window and does not exhibit any significant perturbation or discontinuity in the last 400 Myrs. This suggests that metal mixing and enrichment is a continuous process and relatively unaffected by violent dynamical effects.

#### **4.3.4 The Stripped CGM Hypothesis**

From the previous sections we saw some surprising results - in the tail we see clumps of cool, entrained gas accounting for over 30% of the total tail mass (Figure 4.13). These gas particles saw violent accelerations correlating with increases in ram pressure (Figure 4.18), and two phased temperature mixing with both the stripped ISM and the IGM (Figures 4.20, 4.19 and 4.21).

Figures 4.16 and 4.15 show that the bulk of the entrained tail gas is CGM gas in the past, and Figure 4.18 shows the ram pressure impacting both the entrained and stripped gas. Since much of the tail gas originated from the CGM, we next examine the properties of the CGM and track it over time. We define a set of CGM particles as particles between  $3r_e$  and  $R_{\text{vir}}$  3.2 Gyrs ago, and track those particles forwards in time. Looking at Figure 4.24, we can see the CGM sticking around while slowly accreting onto the ISM, but at around -1 Gyrs (third row third column) we see the CGM start to get pushed, as if it is getting stripped. In the following panels the CGM appears to get swept up behind the galaxy, forming a tail.

Further evidence of this CGM sweeping can be seen in Figure 4.25. The velocity trajectories of the CGM particles look relatively stable and keplerian, up until

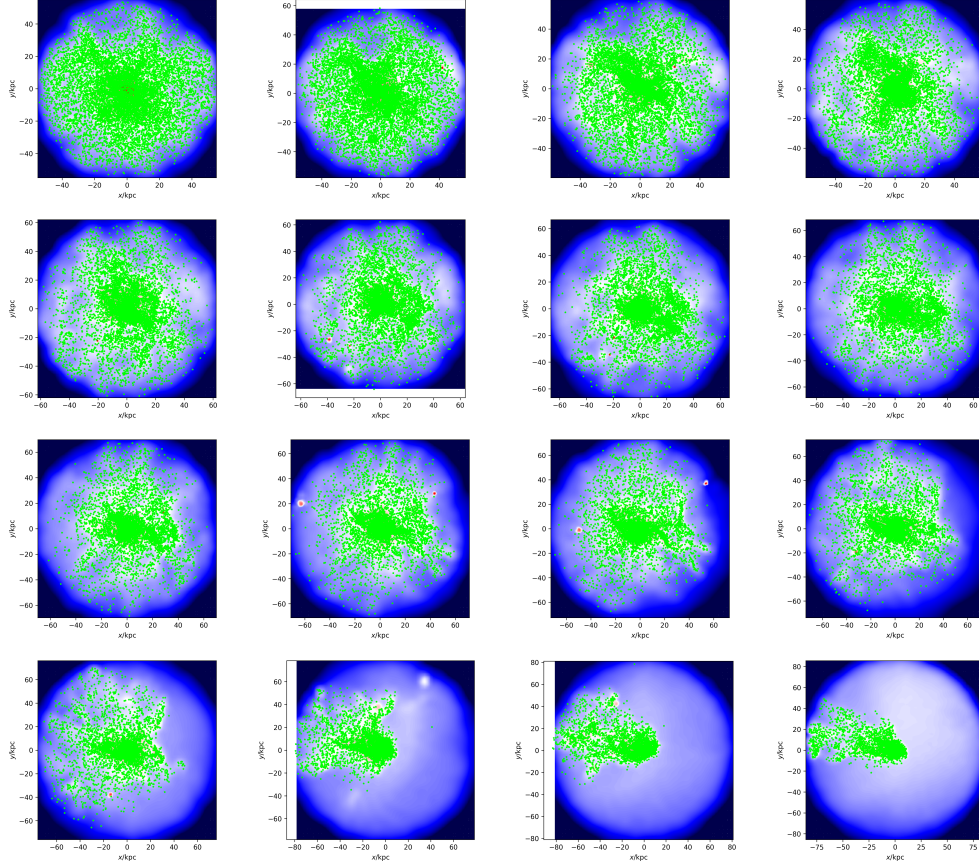


FIGURE 4.24: The time evolution of the CGM for galaxy 10641. Time moves forward from left to right, top row to bottom row, starting at -3.2 Gyr in lookback time and ending at the current time. The lime particles are all CGM particles at -3.2 Gyr traced to the time in their current frame. A full video can be seen at this link: [https://youtu.be/TQIbBA\\_06-M](https://youtu.be/TQIbBA_06-M)

the ram pressure spikes, where we see sharp accelerations of a significant portion of the CGM. Interestingly this is unlike what we saw with the entrained gas in Figure 4.17, where for galaxy 648-1286, its entrained gas did not see significant acceleration. Flagging the trajectories undergoing this acceleration and looking at the galactocentric trajectories in Figure 4.26 confirms that these particles reside on the outer regions of the CGM, and swiftly move away from the galaxy as velocity

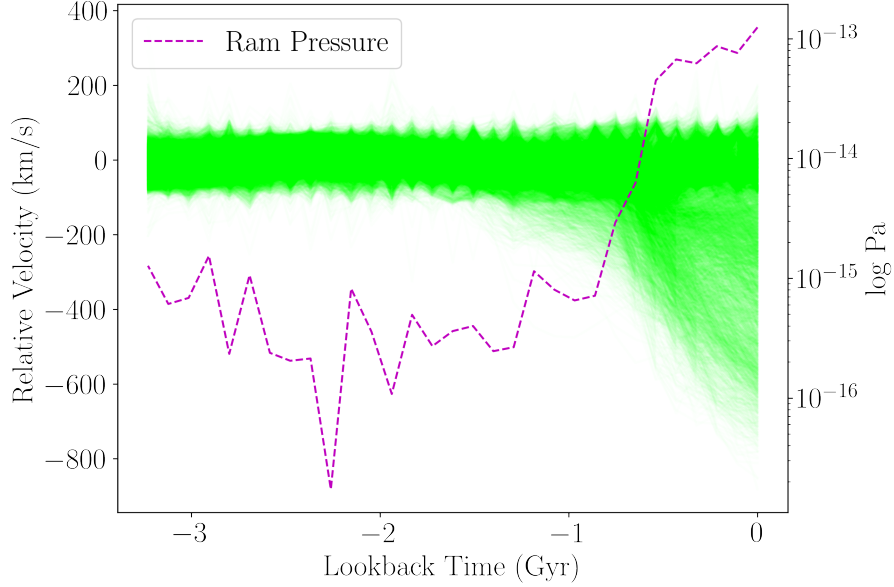


FIGURE 4.25: Projected relative velocity trajectories of the CGM gas from -3.2 Gyr (see Figure 4.17 for the concise definition of projected relative velocity), with ram pressure plotted in magenta.

and ram pressure spike.

Figure 4.27 paints a clearer picture of what’s going on with the velocities. We can see the velocity distribution looking normal at both -3.2 Gyrs and -1 Gyrs in lookback time. However at the current time the distribution flattens, with a significant plateau of gas at significant velocities relative to the disk.

We have only tracked the CGM from a particular point in time and seen that it is stripped at a later point in time - it is difficult for us to make conclusions on the CGM as a whole from this. To account for this we can also examine the immediate environment of the galaxy over time dynamically. At each snapshot, instead of tracking the properties of the CGM particles from -3.2 Gyr, we study the properties of all the particles between  $3r_e$  and  $R_{\text{vir}}$  at the current snapshot. This measure of the galaxy’s evolving environment is equivalent to a measure of

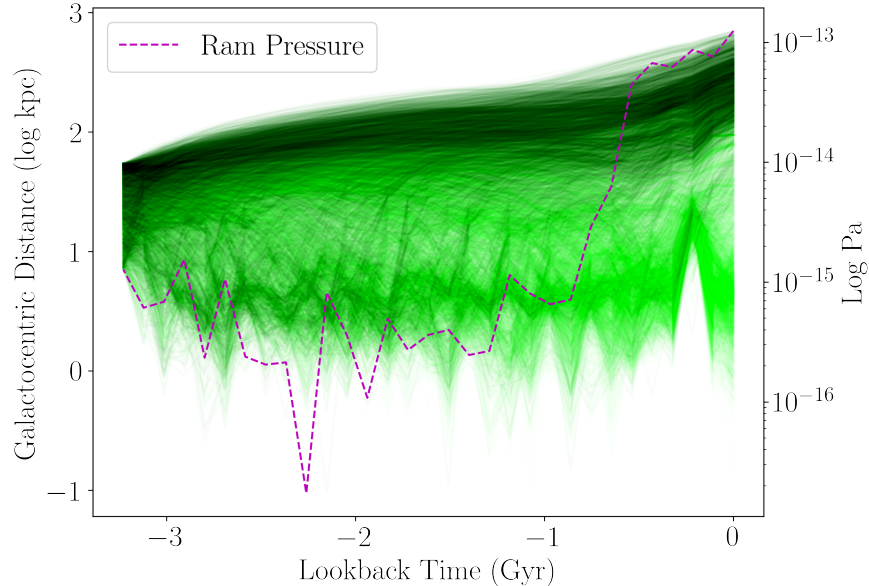


FIGURE 4.26: Projected radial trajectories of the CGM gas from -3.2 Gyr, with ram pressure plotted in magenta. Particle trajectories with a final velocity exceeding 200 km/s are shown in black.

the galaxy’s CGM at the initial snapshot at -3.2 Gyr, but less so over time as the outer, unbound particles of the initial CGM leave and other particles fall into the halo. Any sudden, transient behaviours of the immediate environment would also represent similar behaviours in the CGM as a whole.

In Figure 4.28 we track the temperature of the immediate environment of galaxy 10641 over time. There is evidently significant heating in the last 1 Gyr, along with a strong correlation in ram pressure. The preceding steady-state behaviour emphasizes a high likelihood of a direct causal relation between ram pressure and environment temperature. In isolation, the observed heating could be caused by a myriad of factors, such as shock heating. However, combined with all our earlier observations in, the most likely scenario is that the CGM is getting stripped. At later times when we examine the particles between  $3r_e$  and  $R_{\text{vir}}$ , we are mostly

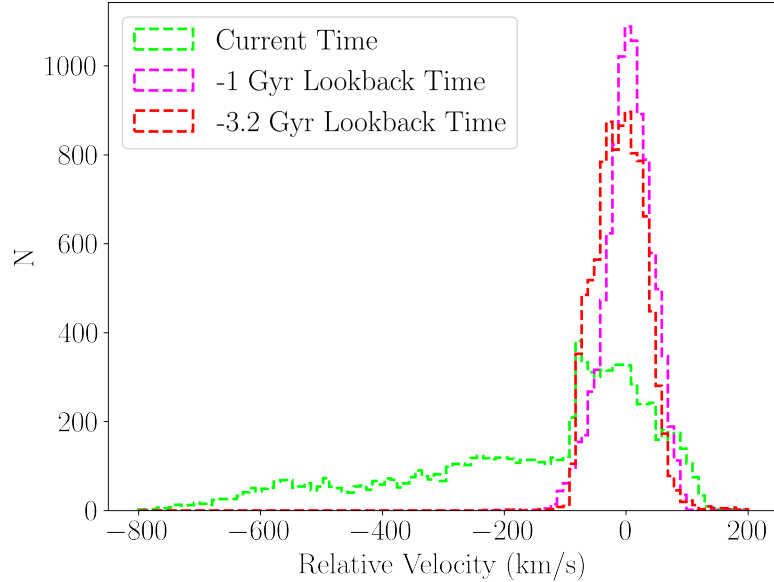


FIGURE 4.27: Projected relative velocity distributions of the CGM gas at three distinct times - current time (green), -1 Gyr lookback (magenta) and -3.2 Gyr lookback (red). -1 Gyr lookback was chosen to visualize the distribution before the ram pressure spike.

grabbing hot group medium particles. This is also evident from Figures 3.10 and 3.4, where we see a large population of fast, unbound gas in the histograms, and a halo dominated by laminar streamlines in the velocity map.

What we’ve presented in this section is evidence towards a novel entrainment mechanism, which in turn represents a novel tail formation mechanism. We find that ram pressure is not only stripping the ISM, but also the CGM. The tail is multiphased, consisting of ISM gas directly stripped from the disk, and CGM gas swept into the stripped ISM gas. We did note earlier that the trajectories with large accelerations in Figure 4.25 did not match up with the entrained gas trajectories in Figure 4.17, but we saw in Figure 4.26 that these accelerated gas particles are indeed leaving the galaxy. This distinction is the result of our tailfinding algorithm only choosing particles within specific velocity bounds. We can directly compare

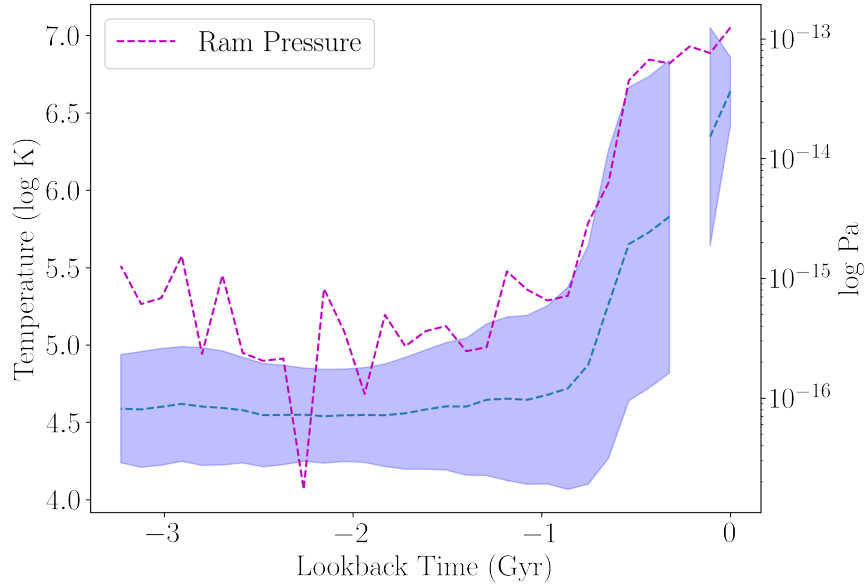


FIGURE 4.28: Temperature trajectory of the non-tail particles within  $R_{\text{vir}}$  of galaxy 10641 over time, with the mean shown as a blue dashed line, one sigma shown as a shaded region, and ram pressure in magenta. Non tail particles refer to all particles between  $3r_e$  and  $R_{\text{vir}}$  that are not particles identified as the tail at the current time. The break in the line represents a bad data point where there was interference from a flyby object.

the entrained gas velocities with the CGM velocities in Figure 4.29, where we see the mean velocities of both distributions trend downwards together at around -1 Gyr, but the entrained gas velocity suddenly restores itself back towards the galaxy velocity. Physically, this is a strong indication of some momentum mixing process, possibly driven by turbulent flows observed in Figure 3.4.

Tail formation via this CGM sweeping mechanism would explain the spikes in tail mass that preceded the spikes in ram pressure in Figures 4.11, 4.9 and 4.10 - the relatively smooth and continuous acceleration of the CGM as seen in Figure 4.25 means our tailfinding algorithm would identify these sweeping CGM particles as a part of the tail for a few snapshots. This is evident in Figure 4.30, with the

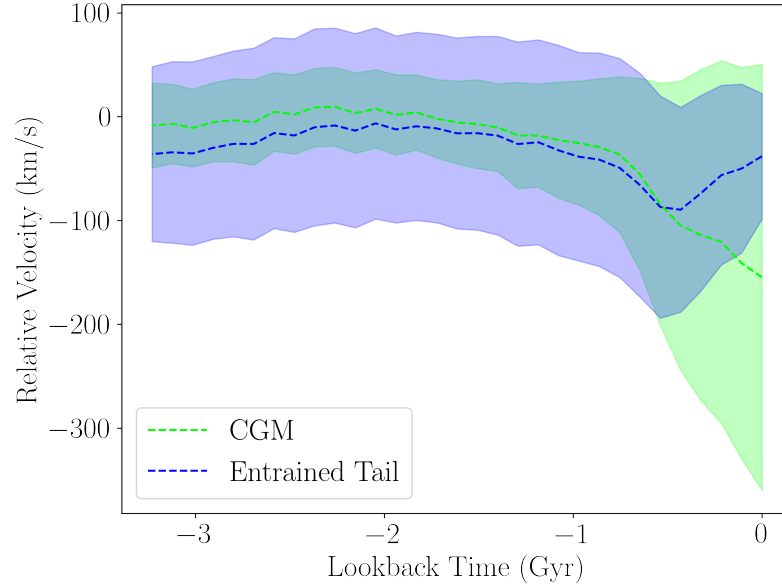


FIGURE 4.29: Projected relative velocity trajectories of the CGM gas from -3.2 Gyr in lime and the entrained gas in blue. Like with previous figures, the dashed lines represent average trajectories, with the shaded regions representing one sigma.

evident tail mass spike from the left three maps on the top row corresponding to evident CGM sweeping from the left three maps on the bottom row. Physically, this spike represents a tail formed by ram pressure stripping of the CGM, which requires less ram pressure to strip given it is much less gravitationally bound to the stellar disk than the ISM. The drop in tail mass as ram pressure peaks represents a depletion of the CGM, with the remaining tail consisting of stripping ISM and entrained CGM.

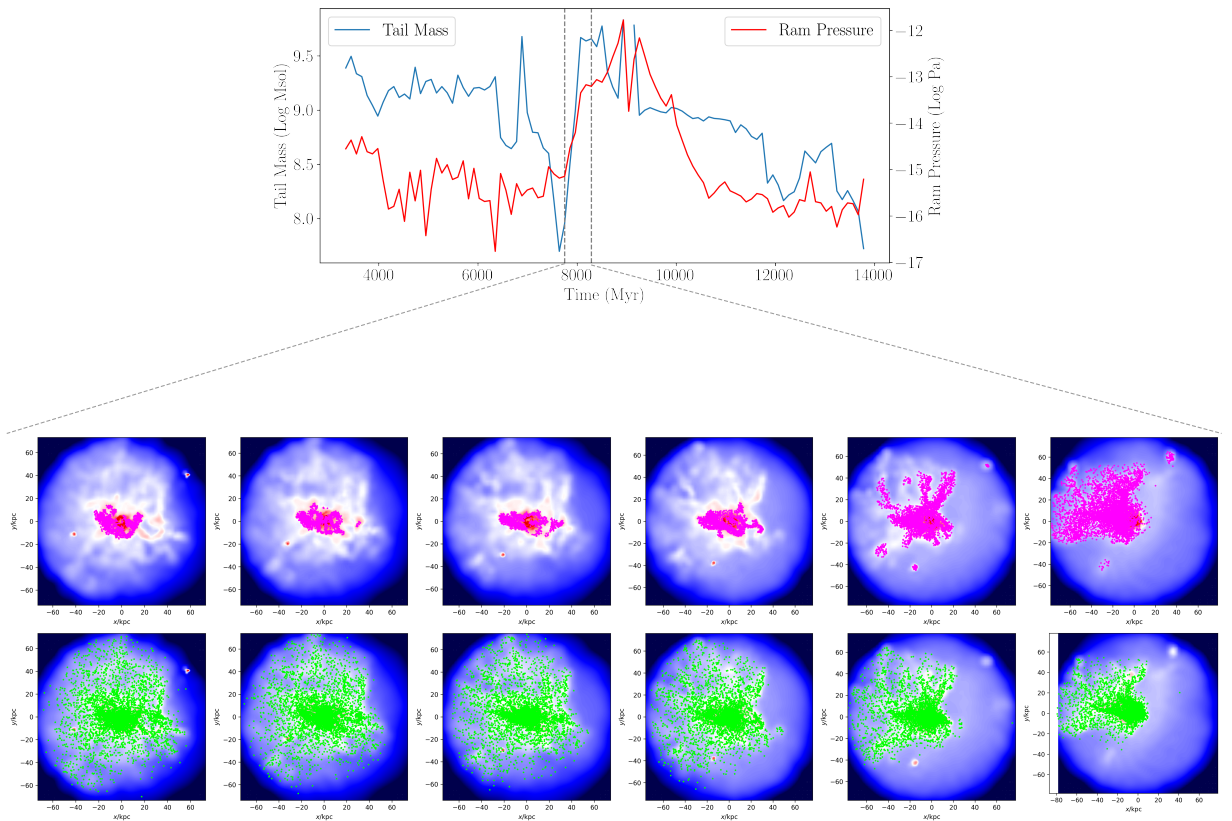


FIGURE 4.30: A closer look at the tail mass spike in 4.10. The maps from left to right show six snapshots within that 535 Myr window. The top row shows the particles captured by our tailfinding algorithm, and the bottom rows shows the CGM particles from 3.2 Gyrs ago (same panels to 4.24 but more time "resolution")

# Chapter 5

## Conclusion

### 5.1 Summary Discussion

Using a series of physically motivated temperature constraints, velocity and density cuts, we identify the tail particles of galaxies. To perform statistics across a relatively small sample of galaxies in group, we look across multiple snapshots to boost our sample size, and then apply a weighting to each galaxy based on their occurrences in the data. We observed the orientations of these tails to behave as expected, with infalling tails pointing away from, and backsplashing tails pointing towards, the central BGG, along with all tails overwhelmingly pointing away from the velocity of the galaxy. However, there was no overall trend in the orientations of all tails. Further statistical analyses on tail mass correlations showed no significant correlation between ram pressure and tail mass. This was a surprising result, but we could not draw definitive conclusions from this since we did not directly cull galaxies that did not have tails (See Section 3.5 and Figure 3.18). However, tracking a couple of visually identified jellyfish galaxies over time showed two very

interesting observations - spikes in tail mass would sometimes precede spikes in ram pressure, and a complete lack of correlation between tail mass and ISM mass. While time offsets are expected between peaks in ram pressure and tail mass, the former should precede the latter assuming ram pressure stripping is the primary mechanism forming tails. Combined with the results of our statistical analysis, this is suggestive of tail forming mechanisms beyond ram pressure stripping of the disk. For two infalling galaxies, we found that at least 30% of the tail mass was not stripped ISM, but was instead CGM material that ended up entrained in the tail. We confirm this by examining where the entrained tail particles were 3.2 Gyrs ago, and found them to be spread out in the CGM. We observed significant amounts of temperature mixing between the stripped ISM, entrained tail gas, and the IGM. Observations of radial and velocity trajectories of the entrained gas show that most of the entrained gas remained in the CGM over the next 3.2 Gyrs, and that the entrained gas saw a sharp acceleration corresponding to a sharp increase in ram pressure. A sharp deceleration proceeded, indicating momentum mixing processes between the the entrained gas and stripped gas. Observations of the CGM revealed very similar behaviours between itself and the entrained gas, with both reacting strongly to ram pressure. Tracking the CGM particles from 3.2 Gyrs to the current time showed the CGM getting stripped. It appears that in addition to stripping the ISM, ram pressure also strips the CGM. This process sweeps CGM material into the stripped ISM, with both constituting the tail. We propose that ram pressure stripping of the CGM is an important tail formation mechanism, on top of known existing tail formation mechanisms in ram pressure stripping of the ISM, and stripped ISM-IGM mixing.

## **5.2 Future Work**

This study unfortunately saw two critical limitations - a limited sample size, and a lack of a proper method to cull non-tailed galaxies. We encourage a replication of this work with larger sample sizes, such as with the IllustrisTNG or Romulus galaxies (Nelson et al. 2019, Tremmel et al. 2017), as well as a method of separating out tailed galaxies from non-tailed galaxies. While one may return to traditional visual identification methods, we also encourage algorithmic approaches such as studying the morphologies and asymmetries, or using machine learning with the training data consisting of existing catalogues of visually identified jellyfish galaxies.

In terms of results, the entrainment of non-ISM gas onto a galaxy tail through ram pressure stripping of the CGM due to ram pressure appears to be a novel phenomenon. We believe this warrants further investigation with higher resolution, larger scale wind tunnel simulations that include both the ISM and CGM.

# Appendix A

## Finetuning the Tailfinding Algorithm

We finetune and constrain the boundaries of our cuts for our tailfinding algorithm such that we seek to maximize two values:

- The total stripped ISM mass
- The ratio between the stripped ISM mass and total tail mass

We set these criteria to capture as much stripped ISM as possible and as little non-tail background gas as possible. To apply this, we examine the tail mass that ever entered the disk (similar to Figure 4.13) for a sample of galaxies with well defined tails. We show the total stripped ISM mass over time and stripped ISM-tail mass fraction over time for five of these galaxies in Figure A1.1. We define the total mass as the total mass of the tail as identified using various schemes described in the figure caption. The mass ever in disk represents the total stripped ISM mass. The red "Everything" curve represents an upper bound in total stripped

ISM mass, since it shows the result of tracking every single particle currently in the CGM back in time. However, since it just grabs every particle, including all background particles, it also represents a lower bound in the mass fraction plot since a sensible tail algorithm that culls background particles would increase that mass fraction.

Our goal is to maximize both the amount of mass we capture in the bottom row, and the mass fraction in the top row. Looking at the top row, across two of the galaxies we see negligible differences in mass fraction between three possible tail finding methods, and across three of the galaxies we see a minimal improvement of around 2-10% in having a velocity cut compared having no velocity cut. On the bottom row, the differences are again minimal, but in a rather obvious manner, the tail algorithm with a  $2\sigma$  density cut captures more mass than a  $3\sigma$  density cut. Based on all the above observations (in addition to a wider range of explored cuts across a larger sample of galaxies), we proceeded with a  $2\sigma$  density cut alongside the velocity cut.

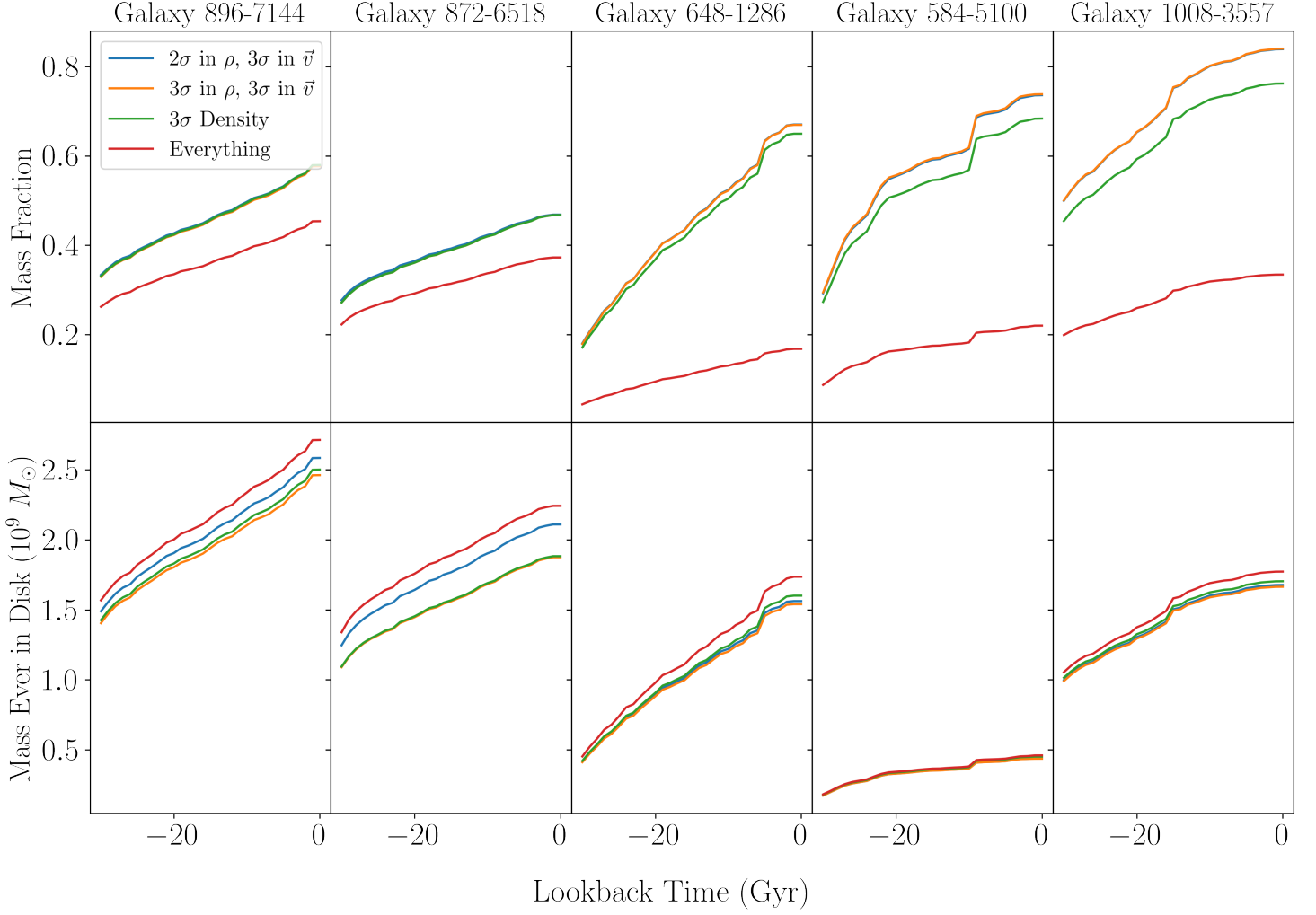


FIGURE A1.1: Mass fraction over time and mass ever in disk over time for five jellyfish galaxies. The mass ever in disk over time on the bottom row represents the total mass of the particles that ever entered the disk, and the mass fraction over time on the top row represents the a ratio between the mass ever in disk and the total tail mass. In various colours we show four ways of defining the tail: the algorithm used in the thesis (Blue), the algorithm with a  $3\sigma$  density cut (yellow), only a  $3\sigma$  density cut (green), and everything in the CGM at the current time (red). Like with Figure 4.13, we track the tail particles identified using each of these schemes back in time, and look at which of these particles ever entered the disk.

# Bibliography

- Allen, S. W., Evrard, A. E., & Mantz, A. B. (2011). *ARA&A*, **49**, 409–470.
- Babcock, H. W. (1939). *Lick Observatory Bulletin*, **498**, 41–51.
- Baes, M. (2020). In: *Panchromatic Modelling with Next Generation Facilities*. Ed. by M. Boquien et al. Vol. 341, 26–34.
- Barnes, J. & Hut, P. (1986). *Nature*, **324**, 446–449.
- Bautz, L. P. & Morgan, W. W. (1970). *ApJ*, **162**, L149.
- Behroozi, P. S., Wechsler, R. H., & Wu, H.-Y. (2013). *ApJ*, **762**, 109.
- Bellhouse, C. et al. (2017). *ApJ*, **844**, 49.
- Belokurov, V. et al. (2009). *MNRAS*, **397**, 1748–1755.
- Bialy, S. et al. (2021). *ApJ*, **919**, L5.
- Binney, J. & Tremaine, S. (1987). Chapter 7: Collisions and Encounters of Stellar Systems. In: *Galactic Dynamics*. Princeton, 421–422.
- Bischko, J. C., Steinhauser, D., & Schindler, S. (2015). *A&A*, **576**, A76.
- Boselli, A. et al. (2018). *A&A*, **614**, A56.
- Brown, T. et al. (2017). *MNRAS*, **466**, 1275–1289.
- Brownson, S. et al. (2022). *MNRAS*, **511**, 1913–1941.
- Bryan, G. L. & Norman, M. L. (1998). *ApJ*, **495**, 80–99.
- Cavaliere, A., Fusco-Femiano, R., & Lapi, A. (2016). *ApJ*, **824**, 145.
- Chang, P. & Etienne, Z. B. (2020). *MNRAS*, **496**, 206–214.

## Bibliography

---

- Choi, W., Kim, C.-G., & Chung, A. (2022). *arXiv e-prints*, arXiv:2207.05263.
- Deb, T. et al. (2020). *MNRAS*, **494**, 5029–5043.
- Del Popolo, A., Yeşilyurt, S., & Ercan, E. N. (2003). *MNRAS*, **339**, 556–568.
- Dijkstra, M. & Westra, E. (2010). *MNRAS*, **401**, 2343–2348.
- Dullo, B. T., Graham, A. W., & Knapen, J. H. (2017). *MNRAS*, **471**, 2321–2333.
- Elbaz, D. et al. (2007). *A&A*, **468**, 33–48.
- Franchetto, A. et al. (2021). *ApJ*, **922**, L6.
- Gullieuszik, M. et al. (2020). *Star-forming clumps in jellyfish galaxy tails*. HST Proposal. Cycle 28, ID. #16223.
- Gunn, J. E. & Gott J. Richard, I. (1972). *ApJ*, **176**, 1.
- Hahn, O. & Abel, T. (2013). *MUSIC: Multi-Scale Initial Conditions*. Astrophysics Source Code Library, record ascl:1311.011.
- Haines, C. P. et al. (2013). *ApJ*, **775**, 126.
- Harrison, C. M. et al. (2018). *Nature Astronomy*, **2**, 198–205.
- Haynes, M. P., Giovanelli, R., & Chincarini, G. L. (1984). *ARA&A*, **22**, 445–470.
- Hickson, P. (1997). *ARA&A*, **35**, 357–388.
- Hinshaw, G. et al. (2009). *ApJS*, **180**, 225–245.
- Hota, A. et al. (2021). *Journal of Astrophysics and Astronomy*, **42**, 86.
- Hubble, E. (1937). *MNRAS*, **97**, 506.
- Huchra, J. P. (2003). Galactic Structure and Evolution. In: *Encyclopedia of Physical Science and Technology (Third Edition)*. Ed. by R. A. Meyers. Third Edition. New York: Academic Press, 369–387. ISBN: 978-0-12-227410-7.
- Hudson, M. J. et al. (2015). *MNRAS*, **447**, 298–314.
- Jaffé, Y. L. et al. (2013). *MNRAS*, **431**, 2111–2125.
- Joshi, G. D. et al. (2019). *MNRAS*, **483**, 235–248.

## Bibliography

---

- Kabsch, W. (1976). *Acta Crystallographica Section A*, **32**, 922–923.
- Kawinwanichakij, L. et al. (2017). *ApJ*, **847**, 134.
- Keller, B. W., Wadsley, J., & Couchman, H. M. P. (2016a). *MNRAS*, **463**, 1431–1445.
- Keller, B. W., Wadsley, J., & Couchman, H. M. P. (2016b). *MNRAS*, **463**, 1431–1445.
- Keller, B. W. et al. (2014). *MNRAS*, **442**, 3013–3025.
- Kenney, J. D. P. et al. (2014). *ApJ*, **780**, 119.
- Knollmann, S. R. & Knebe, A. (2009). *The Astrophysical Journal Supplement Series*, **182**, 608–624.
- Laigle, C. et al. (2016). *ApJS*, **224**, 24.
- Lee, J. et al. (2022). *ApJ*, **928**, 144.
- Leroy, A. K. et al. (2012). *AJ*, **144**, 3.
- López, C. et al. (2011). *A&A*, **534**, A131.
- Luber, N. et al. (2022). *ApJ*, **927**, 39.
- Lucas, W. E., Bonnell, I. A., & Dale, J. E. (2020). *MNRAS*, **493**, 4700–4710.
- Martin, D. C. et al. (2007). *ApJS*, **173**, 342–356.
- Martin-Navarro, I. et al. (2018). *Nature*, **553**, 307–309.
- Menon, H. et al. (2015). *Computational Astrophysics and Cosmology*, **2**, 1.
- Müller, A. et al. (2021). *Galaxies*, **9**, 116.
- Naidu, R. P. et al. (2022). *Two Remarkably Luminous Galaxy Candidates at  $z \approx 11 - 13$  Revealed by JWST*.
- Nantais, J. et al. (2020). *MNRAS*, **499**, 3061–3070.
- Natarajan, P. et al. (2017). *MNRAS*, **468**, 1962–1980.
- Nelson, D. et al. (2019). *Computational Astrophysics and Cosmology*, **6**, 2.

## Bibliography

---

- Nichols, M. & Bland-Hawthorn, J. (2011). *ApJ*, **732**, 17.
- Oppenheimer, B. D. et al. (2021). *Universe*, **7**, 209.
- Paal, G., Horvath, I., & Lukacs, B. (1992). *Ap&SS*, **191**, 107–124.
- Peng, Y., Maiolino, R., & Cochrane, R. (2015). *Nature*, **521**, 192–195.
- Pidopryhora, Y., Lockman, F. J., & Shields, J. C. (2007). *ApJ*, **656**, 928–942.
- Planck Collaboration et al. (2014). *A&A*, **571**, A16.
- Poggianti, B. M. et al. (2019). *ApJ*, **887**, 155.
- Pontzen, A. et al. (2013). *pynbody: N-Body/SPH analysis for python*. Astrophysics Source Code Library, record ascl:1305.002.
- Pringle, J. E. (1981). *ARA&A*, **19**, 137–162.
- Ramatsoku, M. et al. (2020). *A&A*, **640**, A22.
- Ramos-Martinez, M., Gómez, G. C., & Pérez-Villegas, Á. (2018). *MNRAS*, **476**, 3781–3792.
- Roberts, I. D. et al. (2021a). *A&A*, **650**, A111.
- Roberts, I. D. et al. (2021b). *A&A*, **652**, A153.
- Roberts, I. D. & Parker, L. C. (2020). *MNRAS*, **495**, 554–569.
- Rubin, V. C. & Ford W. Kent, J. (1970). *ApJ*, **159**, 379.
- Sánchez, S. F. et al. (2019). *MNRAS*, **482**, 1557–1586.
- Saxena, A. et al. (2018). *MNRAS*, **480**, 2733–2742.
- Schawinski, K. et al. (2014). *MNRAS*, **440**, 889–907.
- Schellenberger, G. & Reiprich, T. H. (2015). *A&A*, **583**, L2.
- Scheuer, P. A. G. (1974). *MNRAS*, **166**, 513–528.
- Slipher, V. M. (1913). *Lowell Observatory Bulletin*, **2**, 56–57.
- Smith, M. C., Sijacki, D., & Shen, S. (2018). *MNRAS*, **478**, 302–331.
- Springel, V. (2005). *MNRAS*, **364**, 1105–1134.

## Bibliography

---

- Springel, V. & Hernquist, L. (2003). *MNRAS*, **339**, 289–311.
- Steinhauser, D. et al. (2012). *A&A*, **544**, A54.
- Steinhauser, D., Schindler, S., & Springel, V. (2016). *A&A*, **591**, A51.
- Stone, J. M. et al. (2008). *ApJS*, **178**, 137–177.
- Strateva, I. et al. (2001). *AJ*, **122**, 1861–1874.
- Suess, K. A. et al. (2022). *arXiv e-prints*, arXiv:2207.02883.
- Sun, M. et al. (2009). *ApJ*, **693**, 1142–1172.
- Teyssier, R. (2002). *A&A*, **385**, 337–364.
- Tortora, C. et al. (2010). *MNRAS*, **407**, 144–162.
- Tremmel, M. et al. (2017). *MNRAS*, **470**, 1121–1139.
- Vulcani, B. et al. (2013). *A&A*, **550**, A58.
- Vulcani, B. et al. (2018). *ApJ*, **866**, L25.
- Wadsley, J. W., Keller, B. W., & Quinn, T. R. (2017). *MNRAS*, **471**, 2357–2369.
- Weinberger, R., Springel, V., & Pakmor, R. (2020). *ApJS*, **248**, 32.
- Wu, B. et al. (2015). *ApJ*, **811**, 56.
- Wu, J. et al. (2017). *MNRAS*, **468**, 109–121.
- Youdin, A. N. & Goodman, J. (2005). *ApJ*, **620**, 459–469.
- Yun, K. et al. (2019). *MNRAS*, **483**, 1042–1066.